SINGLE EVENT UPSET MECHANISMS IN EMERGING MEMORY TECHNOLOGIES

By

William Geoffrey Bennett

Dissertation

Submitted to the Faculty of the

Graduate School of Vanderbilt University

in partial fulfillment of the requirements

for the degree of

DOCTOR OF PHILOSOPHY

in

Electrical Engineering

August, 2014

Nashville, Tennessee

Approved:

Professor Ronald Schrimpf

Professor Robert Reed

Professor Arthur Witulski

Professor Robert Weller

Professor Norman Tolk

ACKNOWLEDGMENTS

No person accomplishes a doctorate degree alone, and debts are owed to those who assist in the process. Great assistance was given to me from the Radiation Effects and Reliability group at Vanderbilt University. These people include, but are not limited to: my advisor Dr. Schrimpf for assisting in project direction and attempting to polish my writing abilities, the multitude of professors in my group that gave countless feedback improving my work, as well as Nick Hooten, Nelson Godspard, Stephanie Weeden-Wright, Mike King, Elizabeth Auden, Enxia Zhang, and other students who collaborated on efforts to further our research. Special gratitude to my committee, Dr. Schrimpf, Dr. Reed, Dr. Weller, Dr. Witulski, and Dr. Tolk, for going through the mentoring and defense process to maximize my work's potential. This work could not be completed without funding from the Defense Threat Reduction Agency and the U.S. Air Force, as well as facilities from Vanderbilt University. Supply of devices was also crucial for much of this research from both Jazz Semiconductor, for their 180 nm process and imec, for their resistive memory structures.

Personal support can equal the importance of professional support when accomplishing a long-term goal such as this. My parents have supported my educational goals throughout my life, pushing me to excel in activities for which I had interest. My friends played a crucial by regularly meeting after hours for libations and debriefing. Finally, my greatest supporter of all, my wife, who put up with me during graduate school, and who will likely remind me of it when is is extremely inconvenient. She is a once in a lifetime discovery for which all my other findings will seem insignificant by comparison.

I wrote this document based on the current state of the art test methods with available resources, keeping in mind a concept that resonated with me throughout my graduate career:

"If you're a scientist and you have to have an answer, even in the absence of data, you're not going to be a good scientist."

-Neil Degrasse Tyson

TABLE OF CONTENTS

List of Tables

LIST OF FIGURES

CHAPTER 1

INTRODUCTION

Designers working in radiation environments often look at emerging technologies to provide radiation tolerance as semiconductor dimensions continue to scale down. Decreased transistor size can lead to an increase in susceptibility that can impede implementation of modern processes in radiation tolerant designs [1]. The radiation tolerance of electronic circuits has long been a reliability concern for space applications, but with sub-32-nm transistor technologies, even terrestrial designers are having to seriously consider the stability of future technology nodes [2–4]. At the same time, planar CMOS circuits are reaching the physical limits of scaling and density (non-radiation hardened technologies), which has led to increased interest in emerging technologies for terrestrial applications [5]. Alternate material (non-flash based) Non-Volatile Memories (NVMs) are seen as a possible next-generation storage technology. Resistive memory technologies, where bits are stored as resistance instead of electric charge, have shown promise as non-volatile memories for radiation environments (robust total dose response), as well as possible scalability advantages over their planar CMOS counterparts [6].

Inter-device spacing will also decrease as scaling trends downward, and understanding the interaction between tightly spaced junctions is paramount to quantifying the response of modern memories and circuits to heavy ion strikes [7–9]. Multi-Node Charge Collection (MNCC) is when more than one node in a system collects charge from a single event. Data on MNCC can be found throughout the literature for circuits and higher level systems [10, 11], but lacks detailed analysis of the generated current pulses and response of a set of junctions. The response of these tightly spaced junctions can aid in the development of radiation-tolerant ICs for highly-scaled technologies and provide insight into the mechanisms driving MNCC [12–14]. Lower-level mechanisms are often inferred using measured

upset rates [15, 16] and/or estimated leveraging device simulations [4, 17], but this runs the risk of overlooking mechanisms that can be less obvious in complicated data.

For the near future, NVM technologies will share the requirement that they be CMOS compatible. This is a fabrication requirement needed for adoption because of the enormous cost of developing, retooling, or rebuilding fabrication plants for non-CMOS processes. CMOS compatibility means that most dense NVMs will be built with tightly spaced silicon transistors. These access transistors will most likely be susceptible to some form of MNCC, requiring an understanding of these mechanisms for quantification of their reliability. Figure 1.1 shows the standard SRAM cell size reported by Intel as a function of technology nodes. The cell areas show how drastically the cell spacing will decrease as gate sizes continue to shrink. The coincidence in response of adjacent memory cells, for instance in two separate 1 Transistor 1 Resistor, Resistive Random-Access Memory (1T1R RRAM) structures, will increase as cell spacing decreases. This work concentrates on understanding the underlying MNCC mechanisms coupled with the single-event susceptibility of the 1T1R RRAM structure.

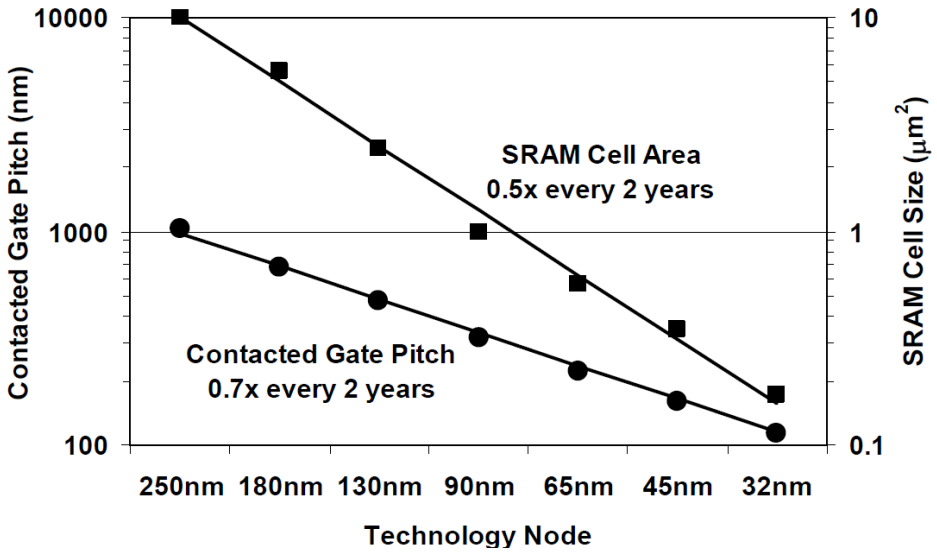

Figure 1.1: Intel's reported standard SRAM cell size as a function of technology nodes [18].

1.0.1 Overview of Presented Work

The cornerstone of this work is the first experimental evidence for single-event upsets in Hf/HfO_2 RRAMs. A new type of upset was also seen, whereby effects from subsequent strikes on a cell can accumulate until the cell transitions to its complementary state. It is termed a Multiple Event Upset (MEU), an extension of the commonly used acronym SEU for Single-Event Upsets. MEUs are made possible because the RRAM lacks a restoration force seen in other memory types (e.g., SRAMs). Data are also presented that show an exponential dependence between the sensitivity of the cell to ionizing radiation and the applied voltage to the BL of the device. The RRAM becomes more sensitive with larger applied bias voltage on the bit line (BL) of the device, which is inverse to similar mechanisms seen in SRAM cells where higher operating voltages decrease a cell's sensitivity.

Further understanding of how RRAM cells will respond in dense memory arrays expected from commercial designs was gathered using a custom diode test structure of tightly spaced silicon junctions in both expirements and simulation. Four independent junctions were alternated between on and off states to quantify the response in each condition. The data showed nearby junctions significantly alter the amount of charge collected on the main junction of interest. If adjacent junctions are biased in the on state, they compete for the same generated charge as the main junction, resulting in decreased charge collection values on the main junction. The difference in the magnitude of MNCC was also compared between heavy-ion experiments, simulation, and Two-Photon Absorption laser experiments. The likelihood that MNCC events occur is higher using laser testing compared to similar heavy-ion data. This result confirms that the larger spot size of the TPA generation region (compared to heavy-ions) does affect the underlying MNCC mechanisms. Understanding these results can change the way circuit designers interpret comparisons of laser data and heavy-ion results, giving them a numerical comparison metric to replace assumptions.

The presented MNCC work can be applied to a variety of emerging technologies (FinFETs, FeRAM, MRAM, PCRAM, etc.); likewise, the RRAM research can be used in situ-

ations where MNCC may not be a factor. Together the presented data and simulations provide insight into how future NVM will respond in radiation environments. Combined with the presented dynamic compact model for the resistive element in the RRAM, simulations were performed on a highly-scaled FinFET device, and showed a relatively low susceptibility to incident radiation. Using this work, well-founded prediction of future generations of emerging memory technologies is possible, allowing designers to choose the best available technologies for fabrication. The ability to predict a technology's single-event response reduces the cost of reliably implementing advanced technologies for mission-critical components in radiation environments.

1.0.2 Outline

The goal of this document is to detail the state of the art for radiation-induced MNCC mechanisms and RRAM single-event susceptibilities. This work provides insight to the radiation effects community and helps enable the next generation of radiation-tolerant memories. This is accomplished by reviewing the available literature on MNCC (Section 2.2), as well as 1T1R RRAM fabrication and operation (Section 2.3). There is also a review of single-event testing sources for reference during experimental descriptions (Section 2.1.4). Chapter 3 presents the experimental and simulation data for MNCC, showing the mechanisms described above, as well as a metric to compare heavy-ion experiments to TPA laser data. Chapter 4 provides data supporting the first report of SEUs and MEUs in resistive memories, along with a compact model used for 3D TCAD simulations. Chapter 5 combines information from Chapters 3 and 4 to simulate the radiation response of highly-scaled FinFET RRAMs using calculated on-orbit environments. A discussion of this work, and future applications of this research are presented in Chapter 6.

CHAPTER 2

Background

2.1 General Radiation Effects

This Background Chapter has been divided into four sections covering various information that is useful throughout the document. Section 2.1 reviews basic energy deposition by energetic particles as well as an overview of different memory storage elements presently used in commercial applications. Section 2.2 covers literature related to the importance of MNCC in radiation environments, and Section 2.3 looks at the current state of resistive memory research.

2.1.1 Processes of Ionizing Energy Deposition

The initial process contributing to a Single Event Upset (SEU) is ionization. There are two main categories of ionization, indirect ionization, a process by which the incident particle creates secondary particles that then generate electron hole pairs in the struck material, and direct ionization which describes electron hole pair generation resulting from energy loss by the incident particle.

The three forms of indirect ionization are: Rutherford scattering, elastic nuclear reactions, and inelastic nuclear reactions. Rutherford scattering, sometimes called Coulomb scattering, occurs when an incident particle passes within a small distance of an atomic nucleus. This close proximity allows the like-charge of the two particles to repel each other and deposit energy into the system. Coulomb forces cause the repulsion, and are the source of the name Coulomb Scattering. A nuclear reaction, in general, is an interaction that directly involves the nucleus of an atom. In an inelastic nuclear reaction, the resultant products are physically different from the particles that initiated the reaction. For instance, when an iron ion strikes a silicon nucleus, the result could be a variety of ions other than silicon and iron. An elastic nuclear reaction is related to Rutherford scattering, but the in-

cident particle comes into direct contact with the nucleus. The products from this reaction are identical to those that existed before the reaction occurred.

Opposed to indirect ionization, direct ionization deposits almost all of its energy along the vector of trajectory of the charge-generating particle. During direct ionization, the incident particle generates electron hole pairs by transferring enough energy to a bound electron to free it. This process is illustrated in Figure 2.1. The freed electrons are often too energetic to interact directly with the energy bands of the device, but will continue to scatter with other bound electrons until they lose enough energy to stabilize at the conduction band of the incident material. This mechanism usually has a fairly constant Linear Energy Transfer (LET) over short distances (10 nm $<$ distance $<$ 1 μm) [19], but can sometimes be accurately estimated over greater distances. Direct ionization dominates SEE in most environments, and will be the focus of this work.

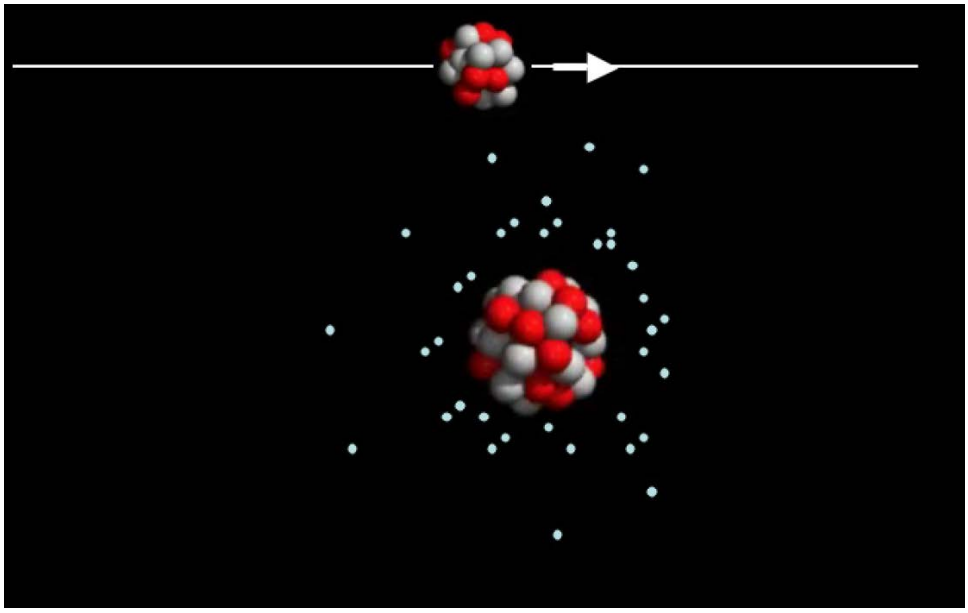

Figure 2.1: Process of direct ionization of an incident particle with the electron cloud of a target material [20].

2.1.2 Ion-Generated Carrier Collection Mechanisms

Output current generated from a strike can be translated to a voltage drop for propagation through a circuit to determine whether or not a cell has upset. The magnitude and duration of a current pulse depends on the fundamental mechanisms of charge transport and the topology of the struck device. There are two dominant mechanisms that contribute to charge transport at the lattice level: drift and diffusion.

Diffusion is a relatively slow process compared to drift. There are two types of diffusion that have a relevant impact on SEUs, and those are standard and ambipolar diffusion. Standard diffusion is regularly used in the solution to carrier transport of operating semiconductor devices. This mechanism works from the concept that an excess of carriers in one area results in a net transport of those carriers into regions with a lower density. The equation for this transport method can be seen in (2.1), where μ is the carrier mobility, D is the diffusion coefficient, and $\frac{dn}{dx}$ is the change in carrier concentration versus distance.

$$J_{Diff} = \mu D_n \frac{dn}{dx} \tag{2.1}$$

Ambipolar diffusion is a special case of standard diffusion by which oppositely charged carriers in a plasma diffuse at the same rate because of the electrostatic attraction between the particles. In silicon, this causes electrons to diffuse slower, while increasing the diffusion of holes. This is a special case of diffusion that is only relevant here due to the ability of high energy particles to create plasma columns when they strike a device. The plasma can affect the transport of charge in the device, either impeding it from moving towards a sensitive node, or keeping the charge from moving away from the sensitive node.

Drift is typically a faster process than diffusion. Drift is enabled by an electric field being present in a material. Carrier transport caused by drift acts on electrons and holes in an opposing manner. Electrons move towards regions of higher potential, while holes are attracted to regions that have lower potential. This causes electron hole pairs deposited

inside an electric field to be separated in opposite directions. The equation for drift current can be seen in (2.2). A concept related to drift current is that of carrier drift velocity, the speed at which a carrier moves due to the presence of an electric field. In silicon, the drift velocity saturates at approximately $1 \cdot 10^7$ cm/s. Equation 2.3 shows drift velocity, accounting for saturation, with the total current equation given in Eq. 2.4 as the sum of drift and diffusion. Eq. 2.5 gives the final equation needed to see how drift and diffusion play a role in the calculation of the carrier velocity, or transport.

$$J_{Drift} = qn\mu E \tag{2.2}$$

$$v_D(E) = \frac{\mu E}{1 + \frac{\mu E}{v_{Dsat}}} \tag{2.3}$$

$$J_{total} = qn\mu E + \mu D_n \frac{dn}{dx} \tag{2.4}$$

$$v_{electron} = \frac{J_{total}}{qn} = \mu E + \frac{\mu D_n}{qn} \cdot \frac{dn}{dx} \tag{2.5}$$

Drift and diffusion are fundamental to all semiconductor devices, but in radiation environments there are several mechanisms that can play a unique role. Conduction through a plasma can occur when the incident particle generates enough carriers along a path extending away from the drain of a transistor to allow that path to become highly conductive. Carriers travel along the column at a higher rate than they do radially away from the column center. When this column extends through a region of high electric field, like a reverse biased junction depletion region, an enhancement of charge collection can occur [21].

Likewise, tracks with high carrier densities can create regions outside of the track that inhibit carrier motion. This is most prominent when the ion track travels through the depletion region and extends well into the substrate. A barrier is established, caused by carrier gradients and thus an electric field, below the track (in the substrate) that inhibits majority carriers from entering into the substrate. The barrier can allow for a higher percentage of charge to be collected at the junction, due to a lack of recombination [22].

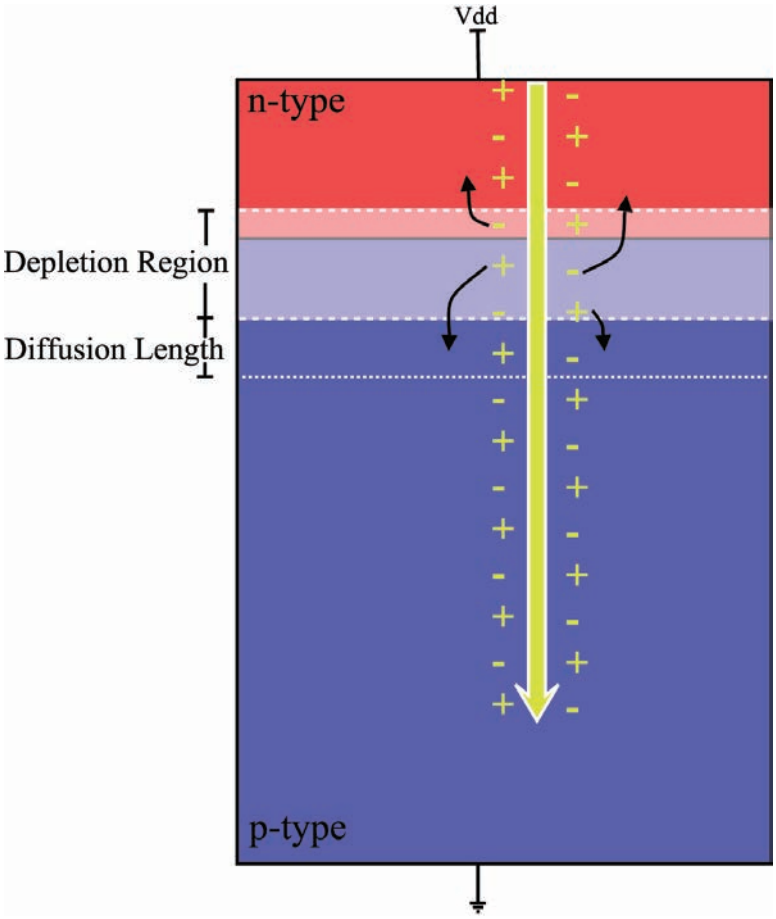

Figure 2.2: Collection from an ion strike is illustrated for a basic p-n junction.

2.1.3 Basic Single-Event Example

A simple overview of current generation from a single-event strike aids in the understanding of this work. A p-n junction diode with an incident ion is shown in Figure 2.2. The strike is normal to the junction, and all electron hole pairs are generated by direct ionization. For lightly ionizing strikes, the field in the depletion region remains stable and immediately begins transporting electrons to the n-type material and holes to the p-type material. As discussed before, this process is fast, and leads to the generation of a current pulse that is often known as the prompt current pulse. The prompt component of a generated current pulse is shown in Figure 2.3. Following the prompt collection, a transition to diffusion-dominated collection occurs. There is not a hard geometrical boundary for this location, rather a range over which drift becomes less dominant. The region, sometimes called the diffusion tail, is labeled in 2.3. The distance a carrier can diffuse before recombining is referred to as the diffusion length.

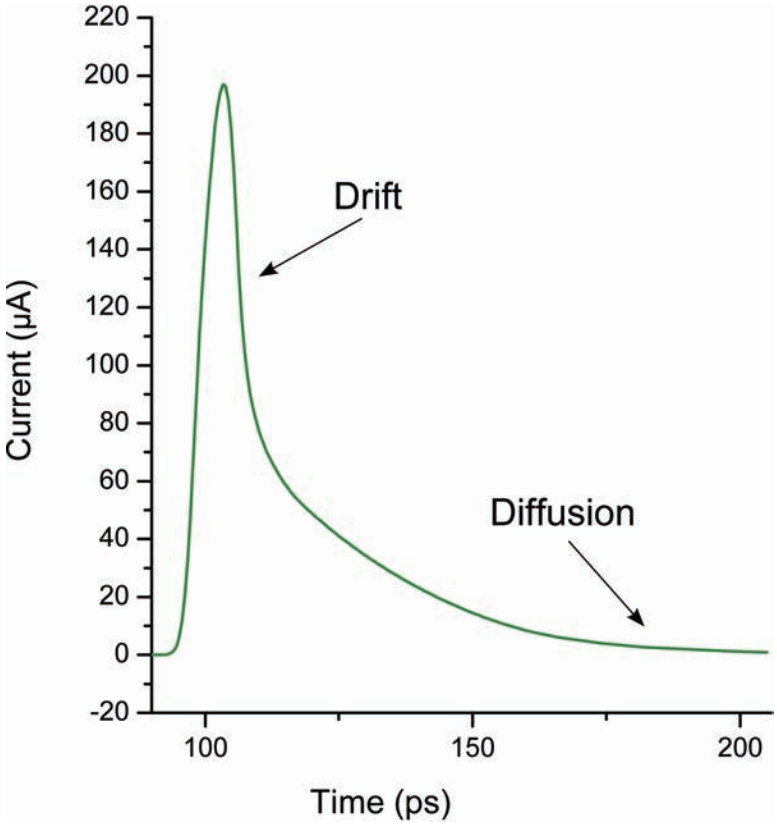

Figure 2.3: The resultant current pulse is shown for the strike in Figure 2.2.

This example uses an unloaded and ideal voltage source to power the device. In circuits, there will be a load of some kind, like a resistive element in the case of the RRAM. This load will change the way the current is collected, always causing slower collection. Slower collection will maintain a voltage drop for longer than the pulse width of the unloaded device. The voltage pulse is what causes error propagation in digital CMOS, and also causes state changes in resistive elements.

2.1.4 Single-Event Excitation Sources

Testing devices and systems in actual space environments is resource intensive [23]; subsequently, alternative ground testing methods have been implemented to help quantify radiation effects on microelectronics while using significantly less resources [24, 25]. The three types of high-flux terrestrial sources are particle accelerators, lasers, and x-ray generators. This section does not cover low-flux sources like button sources, because they are typically only applicable for specialized SEE testing purposes

Particle Accelerators

The original source for ground testing, and arguably the closest comparison to actual space environments, particle accelerators produce energetic ions which can then be used to excite carriers in electronics. Most facilities are broadbeam, where by particles arrive at random intervals, across a relatively large region (2 cm^2). A variety of facilities with different ion masses and energies allow for robust characterization of a wide variety of different environments and effects.

There have also been substantial improvements in the ability to shrink the region of exposure. Microbeam has shrunk the window of opportunity to 3.7 μm^2, and has the ability to raster over a region of interest [26]. The major drawback is the limited ion mass and energy range that can be used in this setup. This setup shares the major issue with ion testing, which is cost. The facilities are very expensive to maintain, and are often less reliable than other testing alternatives.

Focused Laser

Focused laser testing is the lowest cost of the testing sources available. Systems can fit in a normal laboratory space, and be maintained by several experienced engineers. There are two main types of laser excitations for single event testing, single [27] and two photon absorption [28]. Both sources have similar charge generation regions (1μm), which are about an order of magnitude larger than a comparable ion energy deposition region. Single photon laser excitation uses photons above the energy bandgap of the incident material to generate carriers in the DUT. This means that while the generation depth into the material is tunable, it is limited to tens of micrometers, thus requiring the laser to be incident on the top of the active device. This can be problematic for metal overlayers, as the photons cannot penetrate the metal overlayers.

Two photon absorption helps alleviate this issue by using subbandgap photons that can be focused through the entirety of the device material. This allows for backside laser exposure, limiting the effects of metal overlayers. Both laser sources share the same limitation which is their difficulty in generating charge in the system similar to that of an ion. For this reason it is often difficult to quantitatively compare ion and laser data.

Focused X-Ray

Focused X-Ray testing is a relatively recent development for single event testing, and was first shown by [29]. X-Ray irradiation has two main advantages over Laser testing: the carrier generation region can be made to closely match that of a variety of ions and energies, and has the ability to transmit through metal overlayers. The major issue is that X-Ray irradiation will generate trapped charge in device oxides, which can affect device performance due to total ionizing dose [30]. The most promising application of focuses x-ray irradiation is in highly scaled technologies where a 100 nm generation region (approximate ion value) is paramount to getting a realistic response. Multi-node charge collection is an example of a measurement that depends strongly on the nature of the generation region of the excitation source.

Table 2.1: Excitation sources available for single event testing on microelectronics.

Excitation Source	LET ($MeV - cm^2/mg$)	Depth (μm)	Track Radius (nm)	Strike Window (μm^2)	Advantages	Disadvantages
Ion (Broadbeam)	0.8 to 100	300 to 50	50	10^8	• Closest match to environments • Diverse generation characteristics	• Higher cost • Large window of opportunity
Ion (Microbeam)	1 to 35	8 to 100	50	3.7	• Close match to environments • Smaller window than broadbeam • Location specific ion response	• Higher cost • Low LET • Short range
Laser (SPA)	<1 to >100 (Laser Eqv.)	1 to 20	10^4	0.04	• Affordable test setup • High reliability • kHz event rate • Location specific response	• Large generation region • Short transmission distance • No transmission through metal overlayers • Difficult ion comparison
Laser (TPA)	<1 to >100 (Laser Eqv.)	15 (Movable)	10^4	0.04	• Affordable test setup • High reliability • kHz event rate • Location specific ion response	• Large generation region • Large window of opportunity • Reflections from metal overlayers • Difficult ion comparison
Focused X-Ray	<1 to >100	100 to 500	50 to 10^4	0.04	• Small generation region • Public use facility • Transits through metal overlayers	• Under development • Generates charge in oxides • Requires proposal acceptance

2.2 Multi-Node Charge Collection

When technology feature sizes were relatively large ($> 0.25\ \mu$m), the inter-cell spacing made it difficult for generated charge from a normally incident ion to result in significant current generation on two or more sensitive nodes. As node spacing became smaller, MNCC became a topic of interest for the radiation effects community. It has been studied as it pertains to systems [10, 11]. These papers are often able to calculate the number of adjacent cells which are upset as a function of incident flux. Using some assumptions, they make conjectures about the mechanisms at the device-level.

Amusan et al. [7] showed in simulation that inter-device spacing (scales with technology feature sizes), would be a major factor in the amount of charge collected between adjacent nodes. This can be thought of as the magnitude of MNCC. The plot is shown in Figure 2.4. Although simulation based, it suggests that there will be a strong increase in the magnitude and/or quantity of MNCC events as device spacing continues to decrease. It also shows a strong correlation between the Linear Energy Transfer (LET) of the incident ion, and the amount of charge spread between nodes. Both of these factors are important when choosing a technology for space applications, and these issues will be present in both standard CMOS and CMOS compatible non-volatile memories alike.

Artola et al. [11] looked at MNCC as a function of Multi-Bit Upsets (MBU), but had to rely heavily on simulation to garner any information about MNCC. Even this intensive look at MNCC simulations resulted in predicted cross sections being off by 2-3x. Kauppila et al. had better results with compact modeling [12], but very little of this work concentrated on MNCC, and relied solely on simulation to calibrate the compact model. Concentration on a calibrated model was ultimately the same issue with [13], which used simulation work that relied on MNCC simulation to determine the output of higher order systems.

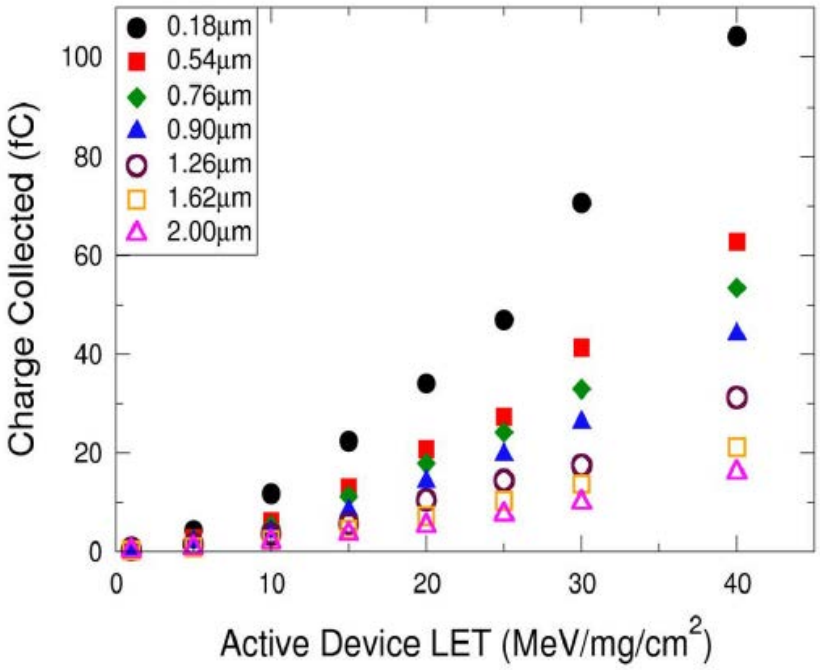

Figure 2.4: .
Plot from Amusan et al. showing the increase in adjacent node charge collection as a function of inter-device spacing [7].

2.2.1 Radiation Hardened By Design

Radiation-tolerant circuit-designers are now taking advantage of MNCC to reinforce their designs. Many of these methods come with minimal area penalties and increased stability with decreased node spacing. One such technique is reinforcement by Pulse Quenching. Pulse quenching is a common mode rejection technique whereby a current pulse on an adjacent node reduces the magnitude of the primary generated current pulse. This reduction in magnitude is called pulse quenching, and is shown as a quenched current pulse in Figure 2.5. Pulse quenching occurs when a strike occurs on S1 (Figure 2.6), because nodes X and Y can both collect charge simultaneously. Collection on one node reduces the magnitude of the generated pulse on the other, reducing the cell's vulnerability.

Another example of radiation hardening by design (RHBD) is Sensitive Node Active Charge Cancellation (SNACC) [32]. This is more concentrated on analog circuitry, but is a similar common mode rejection technique, whereby collection on two adjacent nodes

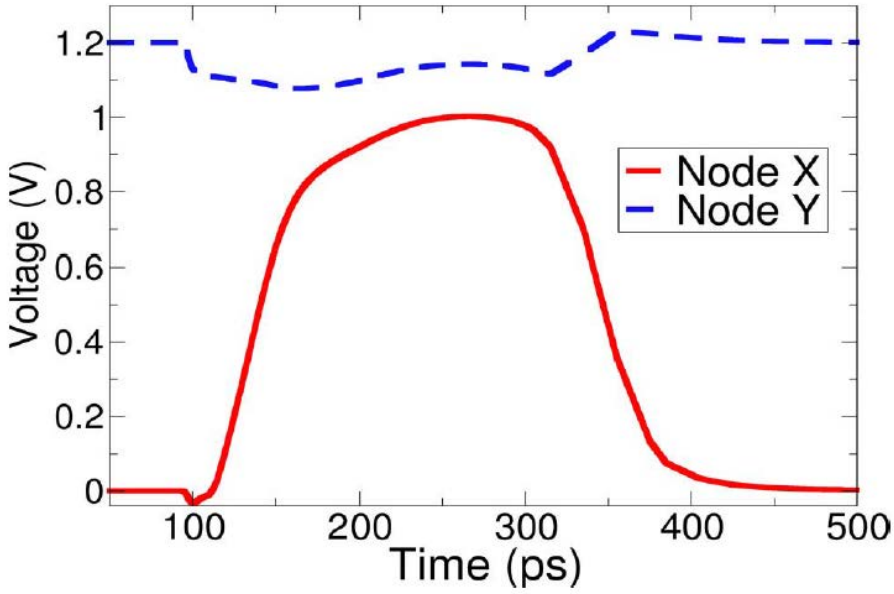

Figure 2.5: MNCC induced current pulse quenching during simulation from [31].

improves signal integrity over a single junction collecting generated charge. The utilization of MNCC for common mode rejection has and will continue to be a popular RHBD technique. Examples include Differential Charge Cancellation (DCC) [32], Reinforcing Charge Collection (RCC) [33], etc. The one thing all these techniques share is the heavy reliance on simulation data to understand how the mechanisms of MNCC affect the charge collection on adjacent junctions, and confirmation is often left solely to TPA laser data.

These are just a few examples of RBHD concepts, much like [14, 34]. In modern CMOS processes, simulation results of RHBD techniques are also often verified using Two Photon Absorption (TPA) laser excitation. This adds a significant layer of complexity of the response of the circuit. The generation region under laser excitation can be orders of magnitude large than that which occurs for ion irradiation. While ions may generate charge near two or three junctions in a modern technology, an equivalent laser pulse could generate charge near 10-20 active devices. Increasing the number of charge-collecting junctions can cause a significant over-prediction in the effectiveness of a hardening techniques based on MNCC. Likewise, alternative testing techniques can result in a much worse response

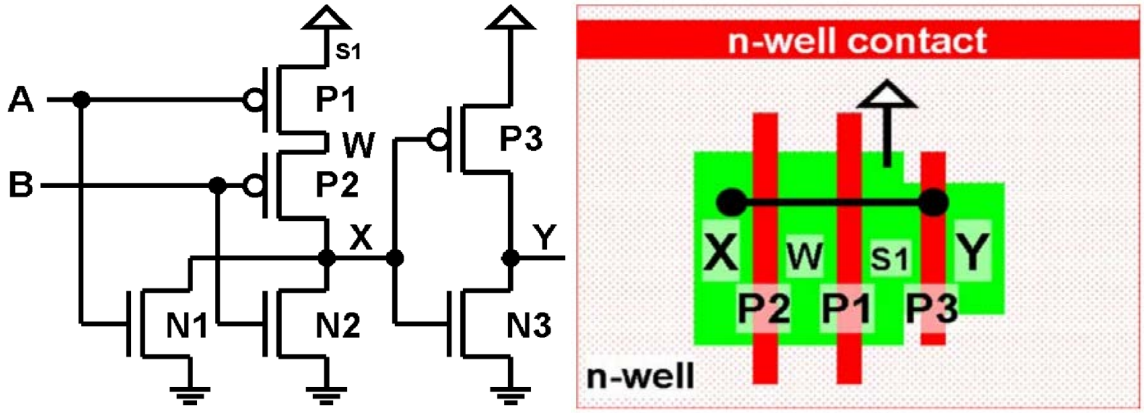

(a) Pulse quenching OR gate circuit. (b) Pulse quenching OR gate layout.

Figure 2.6: Circuit and layout for the pulse quenching technique presented in [31].

for unhardened circuits that have significant MNCC susceptibilities. Quantifying these mechanisms from a basic level will lead to more robust standard CMOS and non-volatile memories, and is one of the goals of this work.

2.3 Resistive Random Access Memories

The prediction of the "Death of Silicon CMOS!" has a long and storied history. Every few years a crucial manufacturing hurdle is faced, and people begin predicting that CMOS circuits will be replaced with a new exotic material or process. Time and time again, the hurdle has been cleared to result in the next generation of CMOS devices. Recently the book had to be rewritten with the introduction of the FinFET, a 3D device topology. This diverged from planar CMOS to create smaller devices that could be more tightly packed to create even higher transistor densities.

Planar silicon memory is facing similar hurdles, and will face even more going forward, so the race is on to find its replacement. Resistive Random Access Memory (RRAM) is one such candidate [35, 36]. It has a crucial advantage that many alternatives do not posses; it can be built on silicon wafers (CMOS compatible), with similar processing steps, drastically lowering the barrier for adoption by large chip manufacturers [37]. This compatibility also closely intertwines the response of RRAM memory cell and standard CMOS because

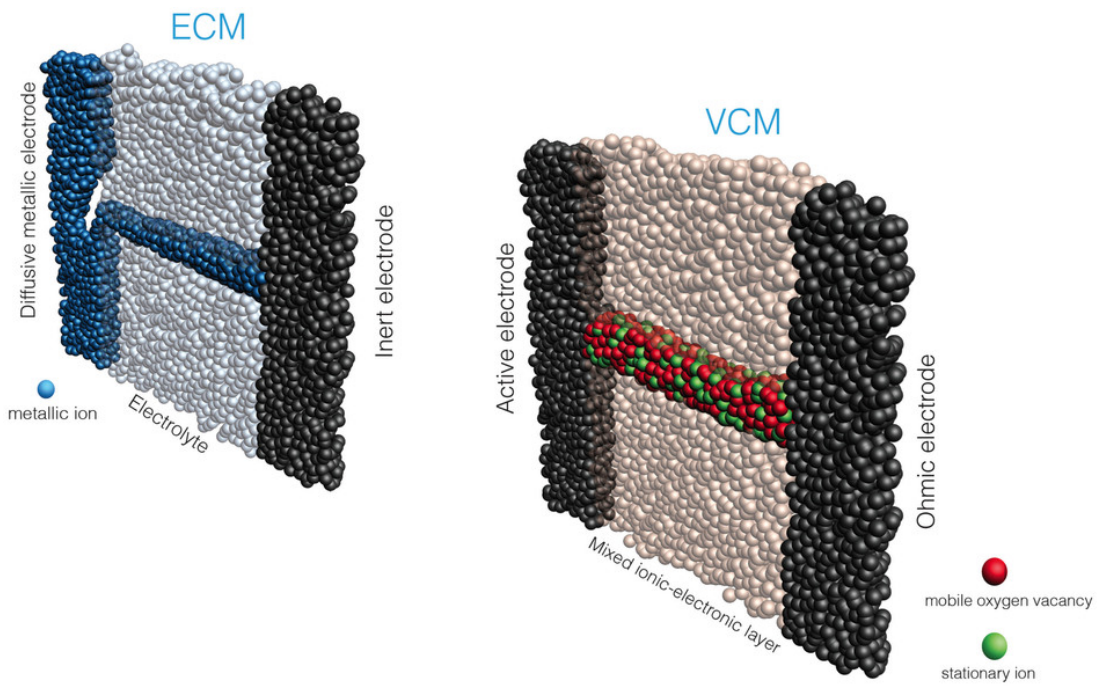

Figure 2.7: The difference between the conduction mechanisms of ECM and VCM resistive memories. ECM forms a metallic ion path through an electrolyte, while VCM forms oxygen vacancies through a mixed ionic-electronic material [38].

they share similar transistor attributes. The RRAM operates by storing a resistance instead of electronic charge, giving it theoretical power and stability advantages over current memory storage technologies. RRAM is still a developmental process, and will, at this stage, have the issues that come along with unproven manufacturing.

2.3.1 Types of Resistive Memories

The two main types of resistive memories used in RRAM are shown in Figure 2.7. They are valence change memory (VCM) and electrochemical memory (ECM). Both types of RRAM are presently manufactured using a one transistor one resistor (1T1R) structure. The transistor is called the access transistor and is used to activate the resistive element for read/write operations. The resistive memory element is built in the overlayers on top of the drain of the access transistor, but other configurations are possible.

VCM typically uses a stack of materials consisting of a stable metal electrode, a reactive

ohmic metal, a switching oxide, and a stable metal oxide [39]. VCM operates by applying a voltage across the electrodes, forming charged vacancies in the switching oxide that lower effective resistance (Figure 2.7). Operating in this manner leads to two possible states (depending on the applied write voltage). In one state, referred to as the low resistance state (LRS), the formed vacancies create a conductive path, leading to a lower resistance. In the other state, vacancies are removed from the oxide, limiting the conductivity of the oxide, and thereby increasing the overall resistance. This is referred to as the high resistance state (HRS).

There are numerous material options for constructing VCM-based RRAMs. For instance, TaO_x, HfO_x, TiO_2, among others have all been studied as suitable switching oxide materials, while Ta, Ti, and Hf have been shown to be suitable reactive metals [35]. Each material choice impacts the overall device performance in complex ways [35] and must be optimized for successful implementation of RRAM into a device. Careful consideration of oxide thickness is also required, as it has a direct influence on the overall switching speed of the RRAM cell. Determining the best combination of materials for the oxide and electrodes results in a large parameter space, whereby each parameter has some effect on the read/write cycle lifetime.

ECM operates much the same way as VCM but with a different underlying structure and switching mechanism [40]. The ECM element stack is composed of an electrochemically active electrode, a solid-state electrolyte, and an opposing electrochemically inert electrode. ECM switches by applying a voltage across the electrodes to transport atoms from the electrochemically active electrode into the electrolyte, forming a path of low resistance metal atoms. Like VCM, it has an LRS, where the metal atoms have created a conductive path, and an HRS, where metal atoms have been removed from the electrolyte to produce a high resistance path. Suitable materials for ECM switching oxides have been shown to be ZiOx, SiOx, and GeOx, amongst others [35]. The active electrode is often Cu or Ag, with common inactive electrodes being Pt or Ni [35]. Just as with VCM, the optimization

of material choices and oxide thickness plays a critical role in determining overall device performance. The device tested in this work is a HfO_2 based VCM memory, and is detailed in Section 2.3.3.

2.3.2 Currently Manufactured Semiconductor Memory Elements

One of the principal limitations in aerospace electronics is the size and speed of reliable memory. Most unhardened memories, such as Flash or SRAM, are unusable for radiation environments because of their sensitivity. The only way to successfully field these technologies is through extensive hardening techniques and error correcting codes that can cause speed, power, and area penalties of 250 % or more [41]. Four types of memories are primarily used for space applications: Static Random-Access Memory (SRAM), Dynamic Random Access Memory (DRAM), Electrically Erasable Programmable Read-Only Memory (EEPROM)/Flash, and Magnetoresistive Random-Access Memory (MRAM). Each is discussed below.

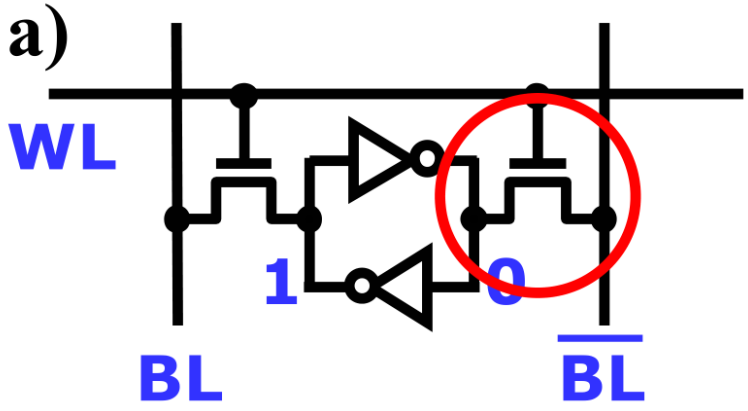

Figure 2.8: Circuit schematic of the common used 6T SRAM cell [41].

SRAM operates by using a bistable latch to store each bit of information. Each latch is composed of multiple transistors (e.g., the common 6-transistor SRAM cell, shown in Figure 2.8 [42]). An SRAM cell is capable of retaining stored information without a regular refresh, assuming the SRAM remains powered. If power to the SRAM is lost, so are the contents of the memory, making it a volatile memory. Non-volatile versions of traditional

SRAM do exist (e.g., nvSRAM [43]), and are sometimes used in situations where retaining stored information is critical. However, non-volatile SRAMs are typically comprised of a traditional SRAM paired with a different, non-volatile memory type (such as EEPROM) [44]. SRAM is used throughout the radiation effects community to measure a process technology node's radiation tolerance. SRAMs are a useful test device because they are easy to layout/operate, and can be found in almost all microprocessors flown on satellites and spacecraft. When unhardened, SRAMs are also highly sensitive to ionizing radiation due to the collection of radiation-induced charge at sensitive semiconductor junctions in the transistors of the SRAM cell [3]. As excess charge is collected, it can lead to a voltage spike on the struck node. If the voltage spike is of sufficient magnitude and duration, it can cause the bit state to flip from its true value, resulting in the storing of erroneous information. As a result, every cell of an SRAM is potentially vulnerable to radiation-induced upsets, requiring that each individual cell be hardened to ensure radiation tolerance.

Dynamic Random-Access Memories (DRAMs) operate by storing bits as electronic charge on a capacitor using a single access transistor. Like SRAM, DRAM cannot be classified as a non-volatile memory (NVM), as the capacitor does not maintain its charge state for long durations during periods of device inactivity. Capacitive storage also suffers from a high sensitivity to radiation. If the access transistor is struck by an ionizing particle, it can discharge the stored charge on the capacitive node at any time during operation, resulting in loss or corruption of stored data [26].

Flash, also known as floating gate MOSFET-based memory, stores data as electric charge in a floating gate fabricated inside its access transistor. Flash can be used in some space applications, because of its reasonable resistance to total ionizing dose (TID) effects, but it still suffers from SEU sensitivity, especially for higher-energy events [45]. This can be mitigated through the use of error correcting codes, but application of Flash memory is still limited to low-flux particle environments (due to its SEU sensitivity), making it difficult to field in many space environments.

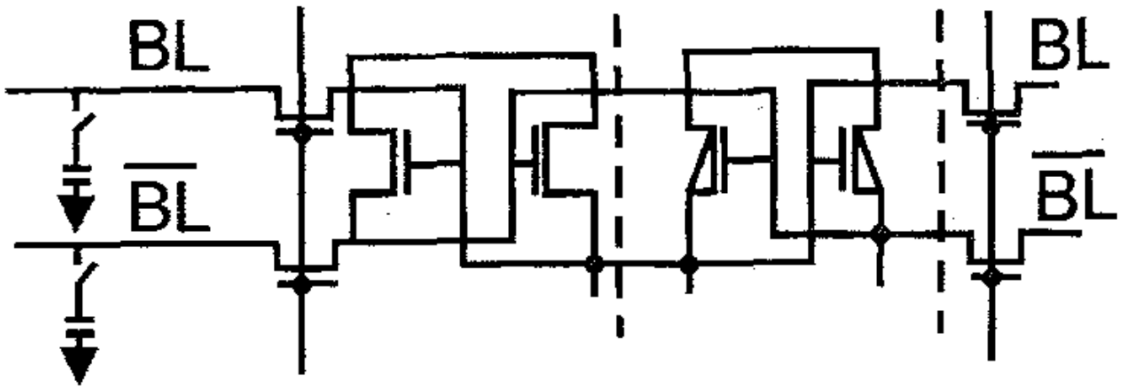

Figure 2.9: DRAM circuit schematic as tested in [3].

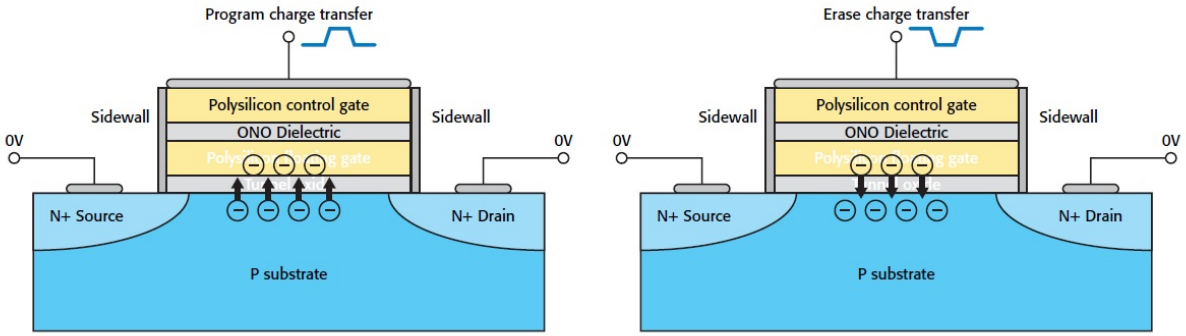

Figure 2.10: Read and write operation of a floating gate Flash memory cell [46].

Magnetoresistive Random-Access Memory (MRAM) is a recently available radiation-tolerant memory for non-volatile applications [47]. It stores data as a magnetic polarization, and is currently available in chips up to 16 Mbits. It suffers from relatively slow access times (approximately 35 ns) and, in its current form, is limited to relatively small bit densities [48]. Of all the previously discussed memory designs, MRAM is the most similar to the resistive random access memory discussed in this work because MRAM is a true NVM and shows good radiation tolerance. However, it lacks the scalability and fast access times seen in current RRAM research, making MRAM a less likely commercial memory for general applications [35].

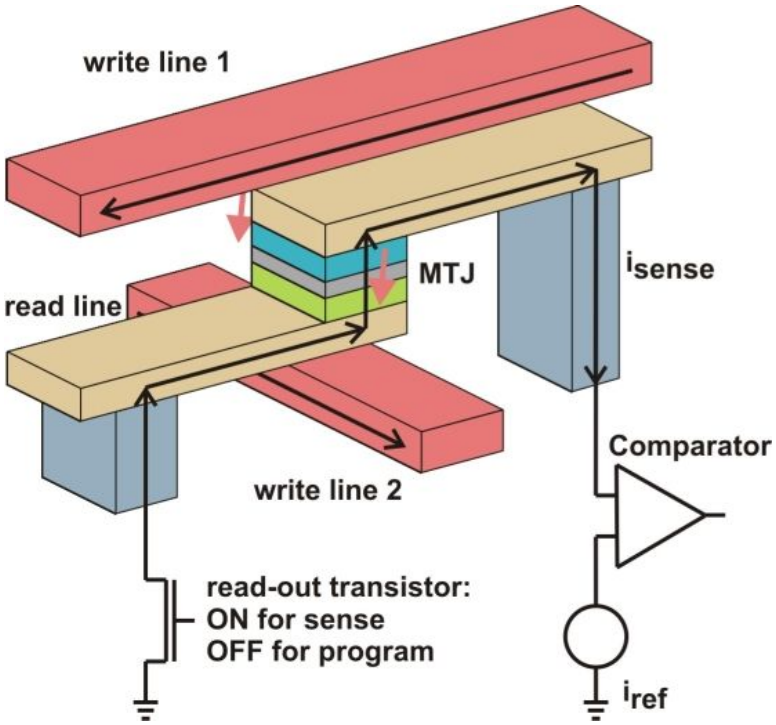

Figure 2.11: Cell drawing of a magnetic tunnel junction (MTJ) based MRAM [49].

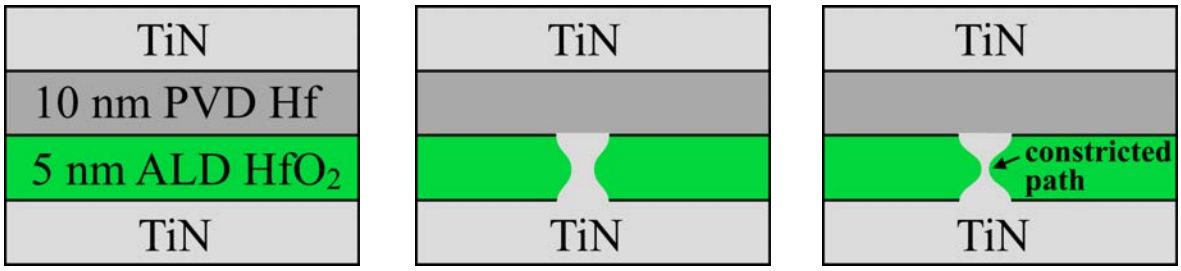

(a) Unformed RRAM structure.

(b) Conduction path after forming (LRS).

(c) Constricted conduction path (HRS).

Figure 2.12: Conduction mechanism in the RRAM resistive element.

2.3.3 Characteristics of Hf/HfO_2 Resistive Random Access Memory

The resistive element of the RRAM consists of two TiN electrodes on the top and bottom of the resistive layers. The top layer is 10 nm of physical vapor deposition (PVD) Hf, while the bottom layer is 5 nm of atomic layer deposition (ALD) HfO_2, Figure 2.12a. These are similar to devices discussed in [50]. This is considered a digital resistive element because it has two states, a High Resistance State (HRS) and a Low Resistance State (LRS), which are analogous to a 1 or 0 being stored as a charged state in a standard CMOS SRAM (Static Random Access Memory) [6].

The physics behind the resistive switching mechanism is still under investigation, but is widely believed to be caused by the constriction or relaxation of the conductive path through the Hf oxide [50–52]. The conduction path is formed by ions that are transported through the oxide by the high electric fields created by the applied voltage across the TiN electrodes. This applied voltage is called “forming” and only takes place once for a resistive element to create the conductive path. When the conductive path is in its unrestricted state, the RRAM to is set to the LRS, Figure 2.12b; likewise when the path is restricted in the oxide, the RRAM is in the HRS, Figure 2.12c. Simulation of this mechanism is discussed in [51].

The resistive element is built on top of the drain of a single access transistor. In this case the transistor is built in a 65 nm process with a gate width of 1 μm and a gate length

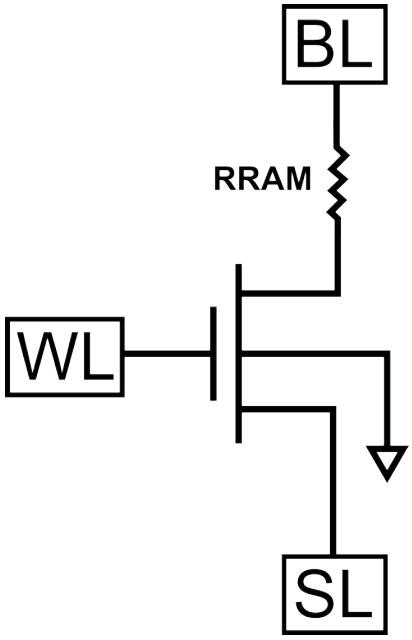

Figure 2.13: Circuit schematic of the RRAM 1T1R structure.

of 100 nm. The TiN electrodes are built on top of the via between the active drain diffusion and the connecting metal layer. Figure 2.14 shows a diagram of the 1T1R structure. This highlights one of the major advantages of the technology, it can be implemented with standard CMOS transistors, and is a vertical process that maximizes density. The same SRAM cell with the same size transistors would require at least twice the area of a single 1T1R cell, cutting the bit density by a factor of two.

2.3.4 Hf/HfO_2 Resistive Random Access Memory Operation

Once the conductive path has been formed during normal operation, the RRAM can be in two states, high or low. The states are not truly discrete, but are decided using bounds of operation. For instance it is common to use values like $<$10 kΩ for the low state, and $>$100 kΩ for the high state [53–55]. This does mean that the exact value of resistance is variable, and highly dependent on the voltage applied to the device. To set the device into a high state, the source is biased high, the BL is grounded, and a voltage pulse is sent to the gate to turn it on for a very short period of time. The field generated inside the RRAM

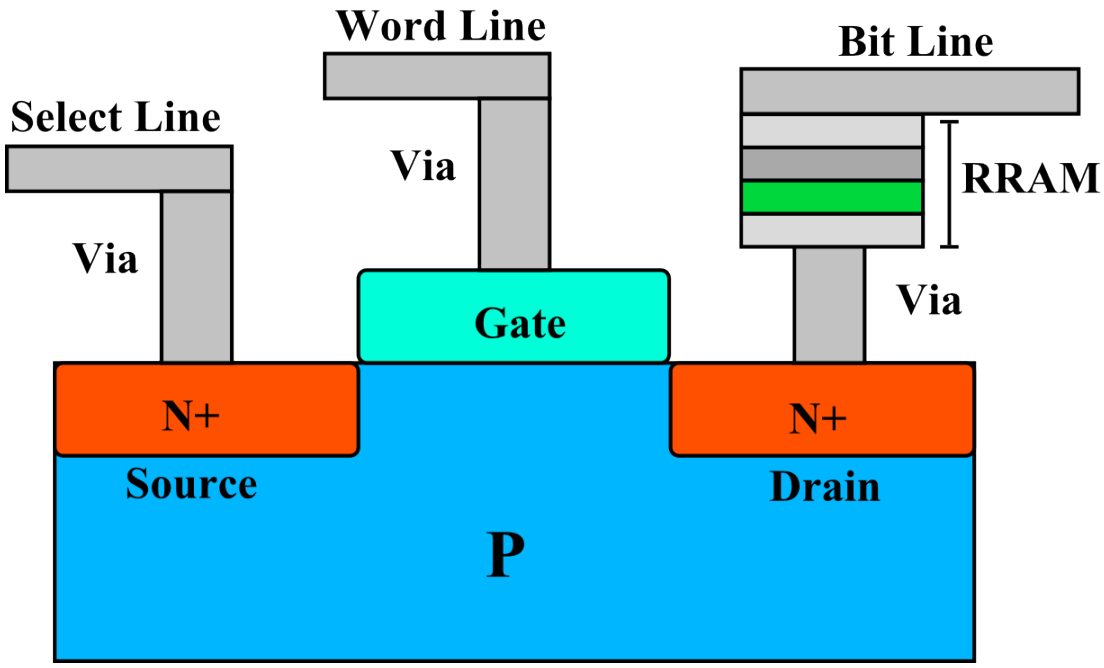

Figure 2.14: Diagram of the 1T1R device structure.

oxide causes a constriction of the conductive path (RESET), creating a higher resistance. The present state of the RRAM is measured by applying a very small voltage across the RRAM and measuring the resulting current. Inversely the RRAM is SET into the low resistance state by biasing the BL high, grounding the source and pulsing the gate. This relaxes or expands the conductive path creating a lower resistance region for current to flow [56, 57].

While there used to be some debate over whether the resistance switching mechanism was voltage or current controlled, several recent papers have provided strong evidence of electric field (i.e., voltage) driven switching [39, 52, 55]. Figure 2.15 shows the dependence of the resistance state as a function of the applied voltage. Regardless of the load resistor, and subsequently the applied current, the same resistance change is seen. Another note from Figure 2.15 is that the amount of time the voltage is applied can strongly impact the resistance.

This begins to show the possibility of a complex single event response as a function of

incident ion and strike location. Since the 1T1R structure is essentially a CMOS transistor with a large resistance applied to the drain terminal, the generated current transients will be something very familiar to the radiation effects community. Similarly, understanding the RRAM response to short voltage spikes being applied across the resistive element, may give great insight into the relative susceptibility to different ions and energies.

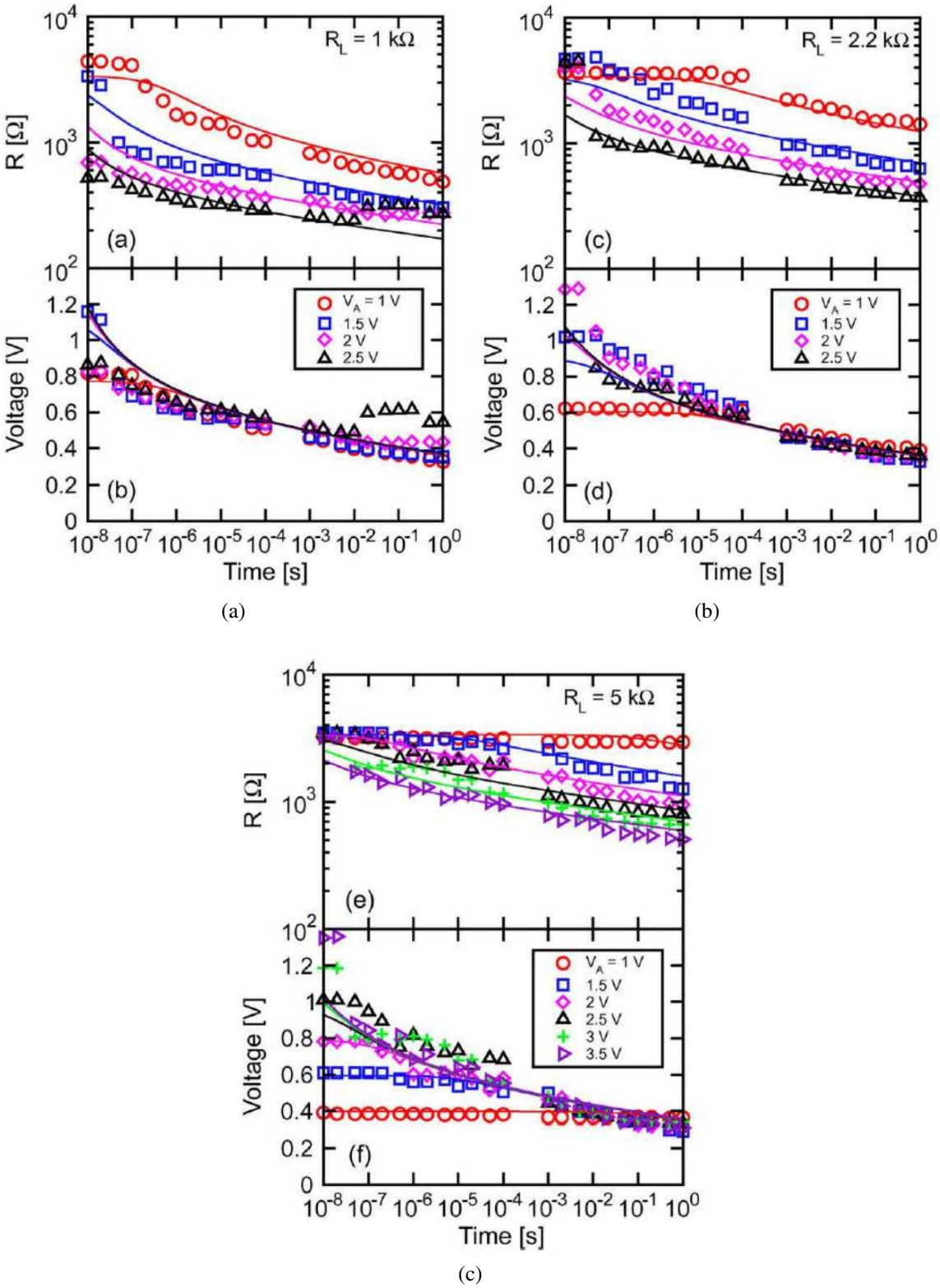

(a)

(b)

(c)

Figure 2.15: Voltage dependence of the RRAM SET/RESET procedure from [55].

CHAPTER 3

Multi-Node Charge Collection

As the size and inter-device spacing of semiconductor devices decreases, the interaction between junctions increases, affecting the response to ion-generated charge [7–9]. In this chapter, heavy-ion and backside two-photon absorption (TPA) laser measurements on closely spaced bulk-silicon diodes are used to investigate MNCC effects on current transients at the individual device level. MNCC occurs when more than one node in a system collects charge from a single event. Section 3.1 explains the experimental setup, while Section 3.2 presents the experimental and simulation data for laser and heavy-ion results. This chapter concludes with discussion of the results in Section 3.3.

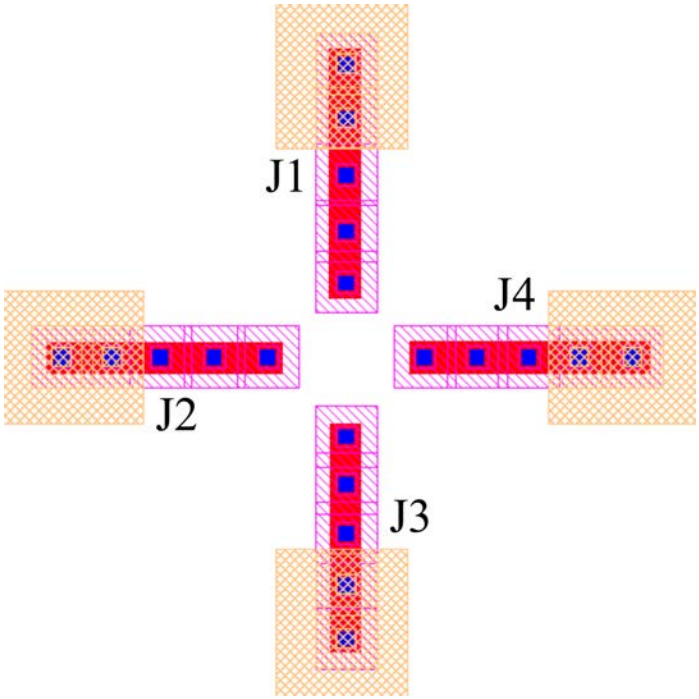

Figure 3.1: Layout of the test structure: N+ regions (red), contacts (blue), metal 1 (purple), and metal 6 (gold).

While data related to MNCC can be found throughout the literature for circuits and higher level systems [10, 11], investigating device-level MNCC effects through high-speed

current transient capture can provide insight into the factors affecting MNCC [12–14]. This information is often inferred using measured upset cross sections [15, 16]. These complex systems convolute the device response with the underlying charge-collection mechanisms, which can lead to conflicting results [8, 10]. The fundamental response of a set of junctions is typically determined using device simulation [4, 17], with experimental verification only in higher level systems. The following sections describe experimental investigations of how neighboring junctions compete for ion-generated charge and the probability that MNCC events occur using different excitation sources.

Broadbeam heavy-ion and backside TPA measurement results are presented for a 180 nm bulk CMOS test structure that was fabricated to investigate MNCC phenomena at the individual device level. Current transient capture measurements using two-photon absorption [28] are used to map out regions in the test structure to reveal areas of single-node and multi-node charge collection. Heavy-ion test results on the same structure are also presented for several ions and energies. These data show the likelihood of MNCC by ion species and generated charge density, which can be correlated to position using TPA measurements.

3.1 Laser and Heavy-Ion Experimental Details

The Device Under Test (DUT) is a set of four identical n+/p-well diodes fabricated in a 180 nm bulk CMOS process, shown to-scale as a GDSII image in Figure 3.1. Each diode is 1x6 μm and is 1.3 μm from its nearest neighbor (corner to corner). Spreading resistance measurements were performed to determine the device doping. The N+ regions are highly doped and extend a relatively short depth ($\lesssim$100 nm) compared to the p-well and shallow trench isolation (STI). This is a blanket p-well technology, meaning the entire substrate (10^{15} cm^{-3}) is doped with a p-well (10^{17} cm^{-3}), and its depth was measured to be 600 nm.

The N+ diffusions are connected using on chip transmission lines, which connect to I/O pads with no electrostatic discharge protection (ESD) or other circuitry. The substrate

contact (p-well) is out of view in Figure 3.1, but is located 20 μm from center traveling southwest. This 180 nm CMOS process has a standard SRAM cell size on the order of 5 μm^2 (reported by scaling trends in [18]), which is approximately the size of the region between all four junctions in Figure 3.1 (4.85 μm^2). The adjacent active diffusions are also spaced with the minimum distance allowed by the fabrication process. These facts reinforce that the junctions used for the presented results represent approximate spacing for active junctions in standard SRAM cells for this technology.

The on-chip GSG (Ground Signal Ground) pads are wire-bonded to 50 Ω matched microstrips. The DUT and microstrip are mounted using conductive epoxy in a custom brass high speed package that uses high speed precision K connectors for connection with the oscilloscope (Tektronix TDS 6124C). High-speed cables, rated and tested to exceed the oscilloscope sampling rate, are connected to 40 GHz bias tees (50 Ω), with bias voltages supplied by a Keithley 2410 SourceMeter. Collecting junctions are labeled J1 through J4, and are identical except for their location and orientation. Data are recorded using the RATACA code base that is detailed in Appendix A.

Heavy-ion testing was performed with the 10 MeV/u and 4.5 MeV/u cocktails at Lawrence Berkeley National Laboratories (LBNL) 88" Cyclotron in vacuum. Junction J3 was chosen as the oscilloscope trigger channel for all heavy-ion results. Transients are captured if and only if J3 generates a transient exceeding the trigger level.

TPA laser testing was carried out at Vanderbilt University. The laser system used in this work employs optical parametric generation (OPG) in a BBO crystal to convert 800 nm, 120 fs pulses at a repetition rate of 1 kHz from a Titanium/Sapphire chirped-pulse amplifier (Titan, Quantronix, Inc) into signal and idler wavelengths. The OPG (TOPAZ, Light Conversions Inc) is tuned to a signal wavelength of 1260 nm; available pulse energies at this wavelength can exceed 150 μJ. A series of dielectric mirrors are used to isolate the signal wavelength, and a spatial filter reduces the pulse energy and produces a near-Gaussian beam profile. A waveplate/polarizer combination is used to fine-adjust the pulse energy

incident on the sample, and a beamsplitter sends a small percentage of the incident light to a large-area InGaAs photo-diode that has been calibrated with a sensitive pyroelectric detector (J10MB-LE, Coherent Inc.) over the range of pulse energies used.

The signal from the photo-diode is captured for each transient measurement, allowing direct correlation of specific laser pulses and subsequent transients. The TPA data presented here include only those transients from pulse energies that are within one standard deviation of the mean laser energy during the scan. This optimization removes much of the inherent variance in laser pulse energies and allows for a more accurate mapping of the transient response within a relatively small range of laser pulse energies ($\pm$10 pJ). The laser generation spot is optically focused on the active silicon surface of the device, and charge generation spot size measurements [58] show 80% of the generated charge is contained within a 1.2 μm diameter circular region (Gaussian distribution) when using a 100x (NA 0.5) focusing objective. Specific data on spot size measurements can be found in [59]. Scans were run at $\pm 3\ \mu m$ of the surface focus, with no change in the results. The DUT is mounted on a high precision 2-axis linear stage that has a minimum step size of 0.1 μm.

3.2 Results

3.2.1 Two-Photon Absorption Experiments

TPA transient measurements were performed on the diode test structure shown in Figure 3.1. Various laser energies were used to cover a large range of charge generation. The data presented are based on analysis of individual transients captured simultaneously on three separate channels of the oscilloscope. Figure 3.2 shows current transient characteristics on junction J3, exclusively, as a function of laser pulse location, while the adjacent junctions, J2 and J4, are either biased (top) or unbiased (bottom). In order to minimize the pulse-to-pulse variance of the laser energy during area scans, the laser energy is recorded on the fourth channel of the oscilloscope, and data are optimized using RATACA. The response of J1 cannot be simultaneously recorded, and is disconnected for all laser area

scans.

Total collected charge is calculated by numerically integrating the captured current transients. Due to variations in the experimental noise floor, the regions of the captured waveform that fall outside of the transient response will, in many cases, not integrate to zero. In some cases, the integral of this region can even be on the order of the integral of the transient response itself. Therefore, it is necessary to choose integration bounds that appropriately bound the transient response, but do not include a significant amount of the captured waveform outside of the transient response. During a typical measurement, many transients may be captured. This makes choosing these integration bounds by visual inspection prohibitively time consuming. Because of this, it is necessary to develop a method to algorithmically determine the integration bounds during the automated post-processing of the captured waveforms.

This is done by first applying a ten-point median filter to each waveform to eliminate high frequency noise components. The filtered waveform is only used to choose the integration bounds. In this case, the first point of the filtered waveform above 10 μA is chosen as the first bound and the last point above 10 μA is chosen as the second bound. The noise floor cutoff is determined by analyzing noise captures at the test location. These points in time are then used as integration bounds for the unfiltered waveform. This helps eliminate error in measurements on non-trigger channels (possibly only noise) and low frequency drift that can cause small shifts in baselines, which can be especially problematic in heavy-ion data. Eliminating the unnecessary integration of noise by the judicious selection of integration bounds helps to remove sources of error from the measurement that could lead to mis-calculations of the total collected charge. The other reported quantities (peak current and FWHM) are more straightforward. The peak current is determined by the largest value that occurs above the noise floor, and the FWHM is the time over which the transient response is greater than half of the maximum peak current for a particular waveform.

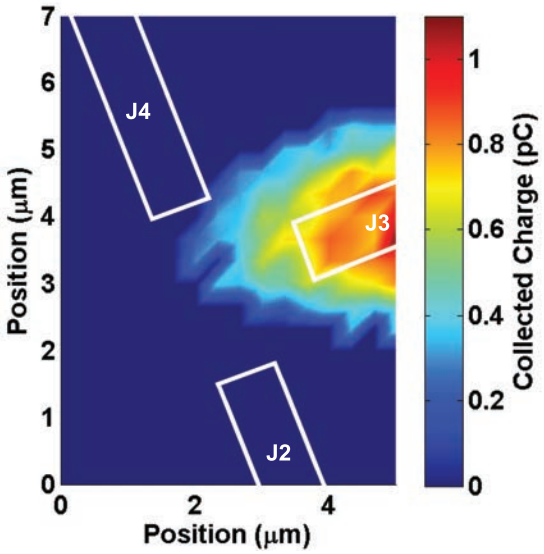

(a)

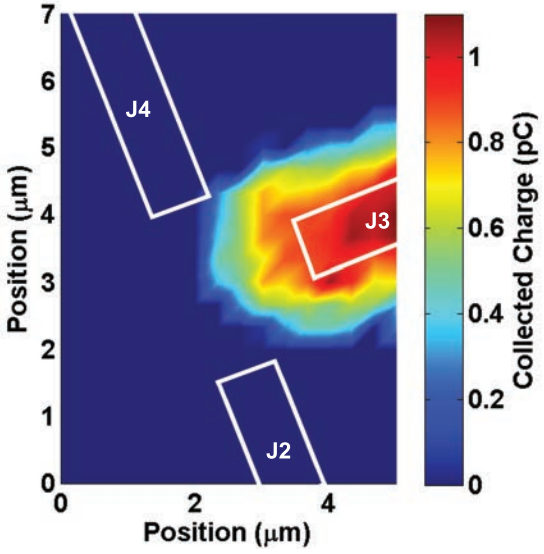

(b)

Figure 3.2: Average values for collected charge from TPA laser data. For (a), J2, J3, and J4 are connected and biased at 3.3 V; for (b), J2 and J4 are disconnected, while J3 is biased at 3.3 V.

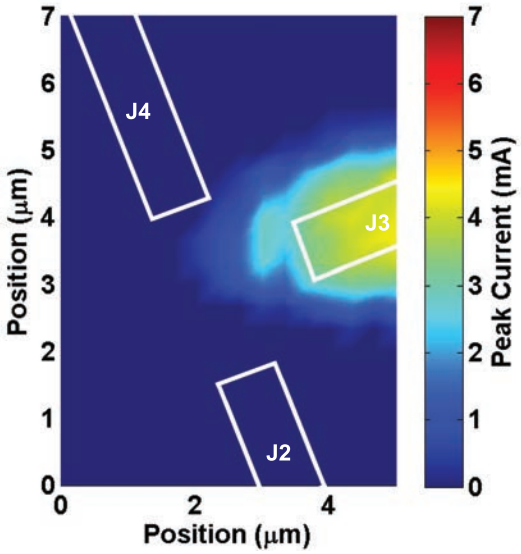

(a)

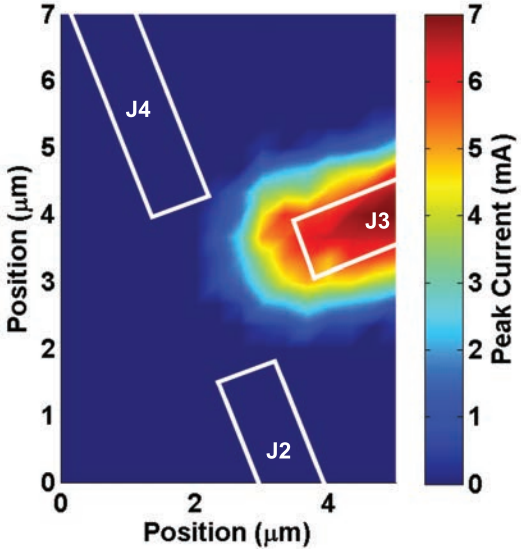

(b)

Figure 3.3: Average values for peak current from TPA laser data. For (a), J2, J3, and J4 are connected and biased at 3.3 V; for (b), J2 and J4 are disconnected, while J3 is biased at 3.3 V.

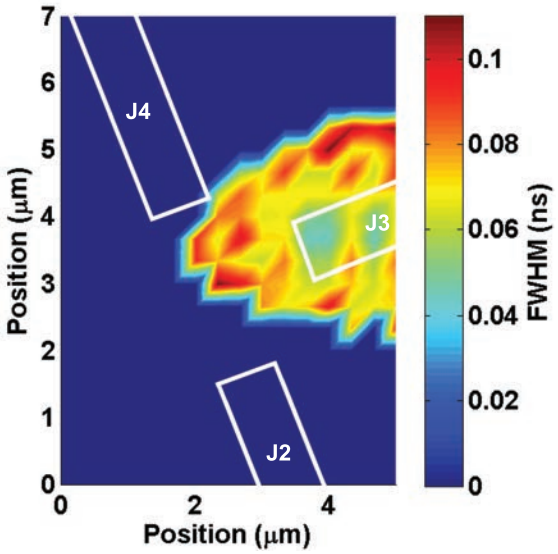

(a)

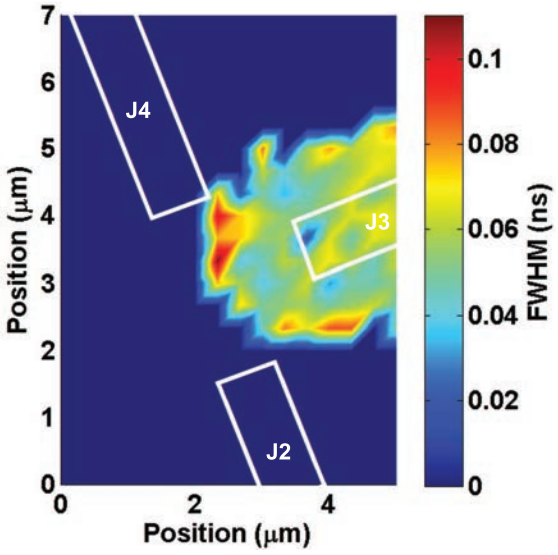

(b)

Figure 3.4: Average values for FWHM from TPA laser data. For (a), J2, J3, and J4 are connected and biased at 3.3 V; for (b), J2 and J4 are disconnected, while J3 is biased at 3.3 V.

The surfaces in Figures 3.2, 3.3, and 3.4 are linearly interpolated between recorded locations. No smoothing or functional fit has been applied to the data. Each record location is the average value for transients generated from laser pulses that are within one standard deviation of the mean laser pulse energy during the scan.

Significant increase in the collected charge can be seen in the region approaching the adjacent junctions, when the adjacent junctions are unbiased, showing the effect these junctions have on J3 (Figure 3.2). Direct strikes on J3 typically result in maximum charge collection, but the collected charge decreases when the adjacent junctions are biased, even though this location is greater than 1.3 μm from an adjacent junction. There is an even stronger difference in the peak current (Figure 3.3), which nearly doubles when the adjacent junctions are disconnected.

The opposite trend holds true for the FWHM (Figure 3.4); the FWHM decreases slightly when the adjacent junctions are not connected, especially for events that occur on the outer edge of J3. The FWHM depends on the peak amplitude, so what appears as a slight pulse broadening here is accounted for by the large difference in peak current. This is shown in Figure 3.5 where the pulses have approximately the same duration, but because the peak current amplitudes differ by about 50%, the magnitude for the half maximum differs by 50%, causing the black curve (adjacent junctions off) to result in a higher FWHM.

The sharing of charge between adjacent junctions can be seen most clearly as a change in the peak and collected charge values near the adjacent junctions (J2, J4). Scans were repeated for a wide range of laser energies (100 pJ to 1.5 nJ) to investigate how the charge is distributed between the junctions as a function of charge density. Charge is collected by multiple junctions for all energies, demonstrating that MNCC exists across the full laser energy range.

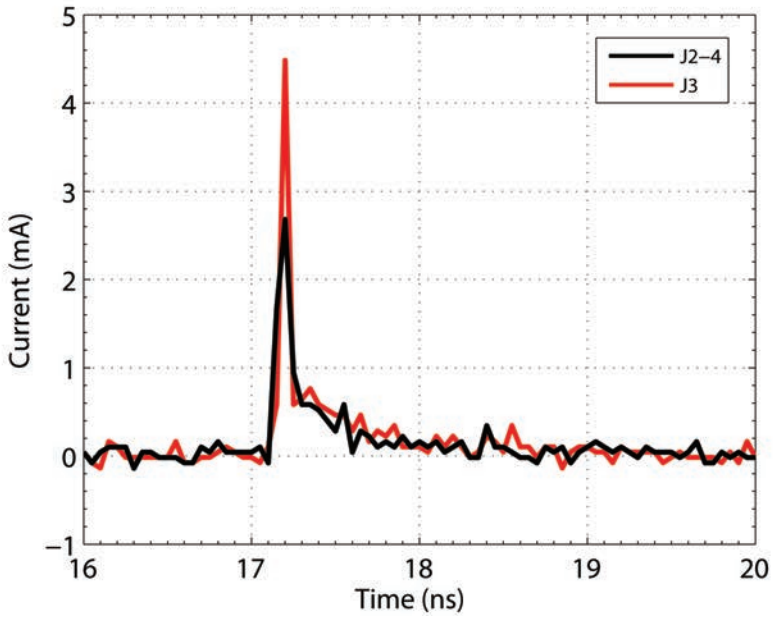

Figure 3.5: Transients from direct strikes to J3 (TPA) with all junctions connected (black) and only the struck junction connected (red). The difference in the peak magnitudes causes a difference in the FWHM that may not correlate to a difference in pulse duration.

3.2.2 3D TCAD Simulations

The distribution of the charge between junctions was analyzed using 3D Synopsys TCAD simulations [60] by looking at the radiation-generated current. Figure 3.6 is a top-side view, 2D slice of a 3D TCAD simulation. The bias value is 3.3 V, and the LET of the particle is 60 MeV-cm^2/mg. The strike occurs at X=0.75, Y=0.75 μm, and the plot is captured 1 ns after the strike occurs. The generation track is normal to the device surface, extends 45 μm in length, and has track radius of 50 nm. The block of silicon was 20 μm on a side forming a cube.

Figure 3.6 displays the difference between the current density in the Z-direction with only J3 connected, and with all junctions connected. Figure 3.6 is made by subtracting the current density in the Z-direction for two separate simulations (all junctions biased at 3.3 V, and only J3 biased at 3.3 V). A value of zero means that whether the adjacent junctions are biased or unbiased, there is no difference in the generated current. If the

value is positive, the current density increases, and likewise a negative value means the current density decreases. The Z-direction is plotted to represent current flowing into, or out of, the junctions. While there is also current flowing in the x and y directions, it is not recorded by the measurement until it flows through the plane in the Z-direction. The most affected junctions are the closest to the strike center. The current density of J3, which is connected in both cases, decreases while that of J4 increases after being connected. The changes in current density flowing into a collecting junction exhibit the same trend as the current recorded at that node by the oscilloscope for the backside laser measurements.

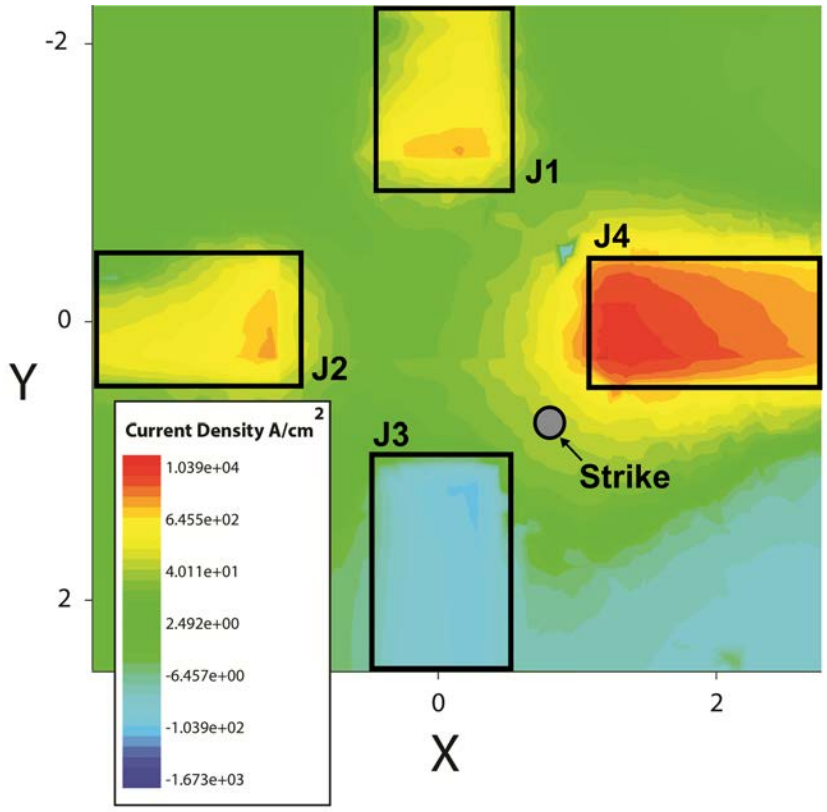

Figure 3.6: Difference simulation plot showing increased charge collection when adjacent junctions are disconnected.

If the strike location is further from the center (e.g. $X = Y = 1.5\ \mu$m), MNCC decreases, due to the increased distance between the deposited charge and the collecting junction. This agrees with the observation that as technology decreases in size, MNCC (competition for charge) increases [7]. For example, at the 32 nm technology node, an entire SRAM cell can

fit inside the region between the corners of J3 and J4 [18], leading to even more competition for the generated charge.

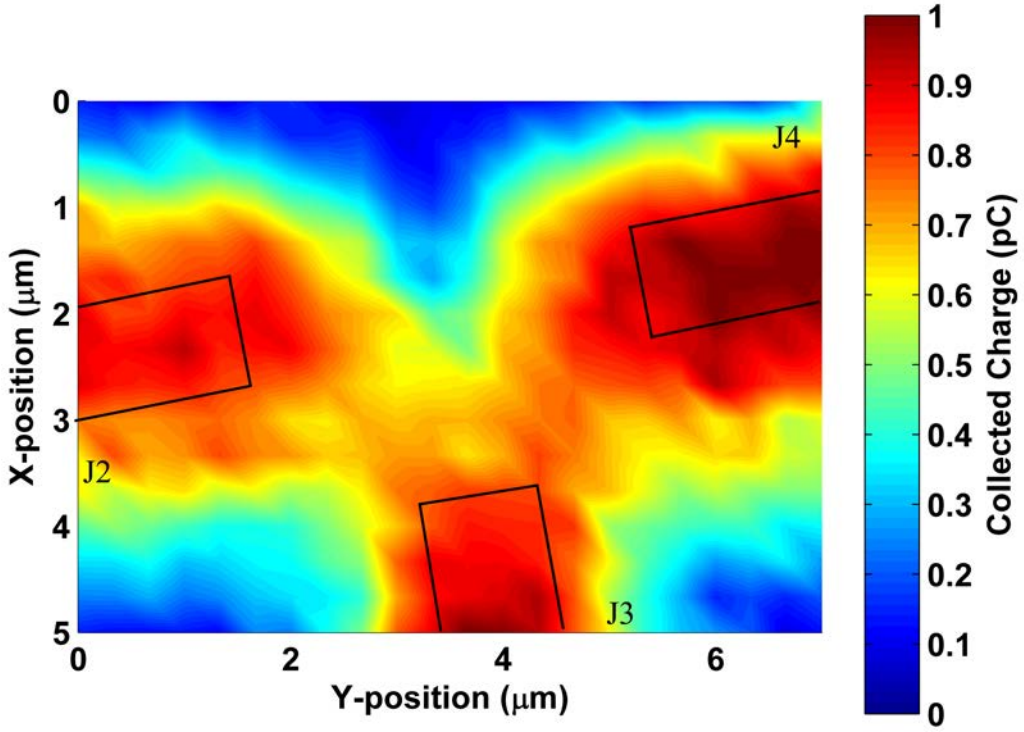

Figure 3.7: Sum of charge collection on all three junctions (J2, J3, J4) as a function of laser position at a reverse bias of 3.3 V, showing regions in between two junctions that collect the same amount of charge as direct hits on a single junction.

The effect of MNCC on the ensemble of junctions can been shown by summing the output from the three active junctions in the device (J2, J3, J4). The sum represents the total charge collected on all three junctions, as a function of laser position, which is shown in Figure 3.7. When the laser generates charge between two junctions, the total collected charge is approximately the same as when a single junction is struck. The region between the nearest neighboring corners of two junctions demonstrates this effect in Figure 3.7 as the narrow red regions that connect the individual junctions. When strikes occur near only a single junction (i.e., not between two closely spaced junctions), only about half as much charge is collected as when the laser strikes between J2 and J3 or between J3 and J4. This demonstrates the sharing of charge between adjacent junctions and the mechanism's strong dependence on the bias conditions of adjacent junctions.

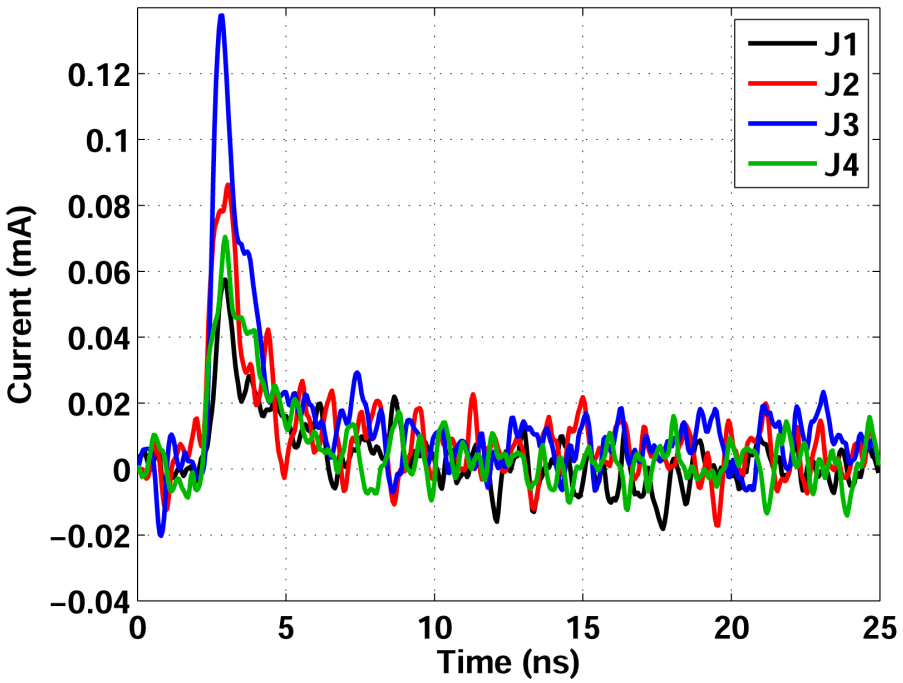

Figure 3.8: Transient capture for a 10 MeV/u Ag strike that occurs approximately in between all four junctions, showing the peak and duration of a strike occurring between all four junctions.

3.2.3 Heavy-ion Experiments

Heavy-ion transient measurements were performed at LBNL on the diode test structure previously discussed. A variety of ions were used from both the 4.5 and 10 MeV/u cocktails in order to cover a range of deposition characteristics, summarized in Table 1. The results presented here are based on an analysis of individual transients captured simultaneously on all four junctions on separate channels of the oscilloscope. This is different from the TPA measurements where only events on three junctions were captured.

Table 3.1: Ion generation properties in Si for the LBNL 88-inch cyclotron.

Ion	LET (MeV-cm^2/mg)	Q_{SV} (pC)	Q_{Total} (pC)
10 MeV/u Ar	9.7	0.12	17.8
10 MeV/u Ag	48.2	0.57	46.2
4.5 MeV/u Y	45.6	0.51	18.2
4.5 MeV/u Xe	68.8	0.74	26.8

Spatial resolution is inherently difficult in broadbeam heavy-ion testing due to the random isotropic flux and beam size (4 inch radius) produced by the 88-inch cyclotron. Even though the exact location of the generated charge cannot be determined, insight can be gained through individual transient captures as well as statistical analysis of the data.

Figure 3.8 is a single capture of a 10 MeV/u Ag ion striking between all four junctions. The total charge collected by all four junctions for that strike is 0.85 pC, which is 91% of the highest recorded strike on a single junction (J3, 0.94 pC). The peak currents however varied significantly from 2.4 mA on the trigger junction (maximum response), to 0.14 mA for a single event that produced a signal on all four junctions. This significant decrease in peak magnitude occurs because the ion does not pass through the depletion region of a junction. The fraction of the deposited charge collected by all junction is similar to that of a direct strike on a single junction, even though there is not a substantial modulation of the depletion region, which is commonly associated with funneling and higher efficiencies [61].

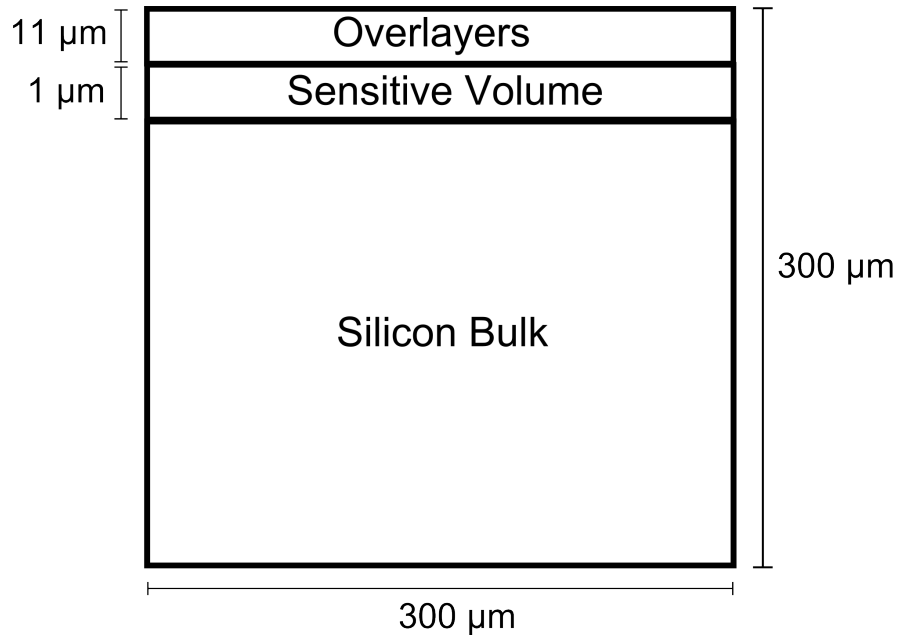

Figure 3.9: Simulation structure and sensitive volume used in MRED to determine the amount of charge generated in the first micrometer of active silicon.

Figure 3.10 shows the probability of MNCC as a function the charge generated by the

ion in the first micrometer of active silicon. The metric used here, ξ, is the fraction of ion strikes that meet a specific set of MNCC criteria (ξ = Valid Events / All Events). To be considered a valid MNCC event, transient captures must a) be above the noise floor, and b) have at least a 15/85% split in collected charge between adjacent junctions. Specifically, if two adjacent junctions collect charge, one will have at most 85% of the total collected charge by the two junctions, and the other junction will have at least 15%. The specific ratio for ξ is somewhat arbitrary, but this value is sufficient to eliminate noise without suppressing actual events. In this test setup, only events that trigger on J3 are measured.

Values are shown as a function of Q_{SV}, which is defined here as the amount of charge generated by the incident ion in the first micrometer of active silicon. This depth approximately corresponds to the collection depth for all the ions tested, based on the incident ion LET and assuming 100% collection efficiency. Q_{SV} can differ significantly from an ion's total generated charge along the entire ion track. For example, 10 MeV/u Ar and 4.5 MeV/u Y have approximately the same total generated charge, but Y generates five times as much charge in Q_{SV}. If these ions were plotted as a function of total generated charge in Figure 3.10, they would have nearly the same x-location, but their MNCC probabilities would vary by over an order of magnitude.

Charge generated in Q_{SV} was estimated for each ion using the Monte-Carlo Radiative Energy Deposition code (MRED) [62]. A 300 μm on a side cubic silicon volume was simulated, including approximately 11 μm of overlayers that are above the sensitive volume, shown in Figure 3.9. Overlayer information was obtained from the device manufacturer. The sensitive volume used to calculate the amount of generated charge is 300 μm wide, 300 μm long, and 1 μm deep was placed at the active silicon surface (below the overlayers), and 10,000 ions were simulated to calculate the average values shown in table 3.1. These ions all have similar radial charge generation profiles in the first few micrometers (excluding magnitude) with the 1/e point of a Gaussian fit at approximately 50 nm.

ξ, and thus MNCC, increases with increased charge generation density in the sensitive

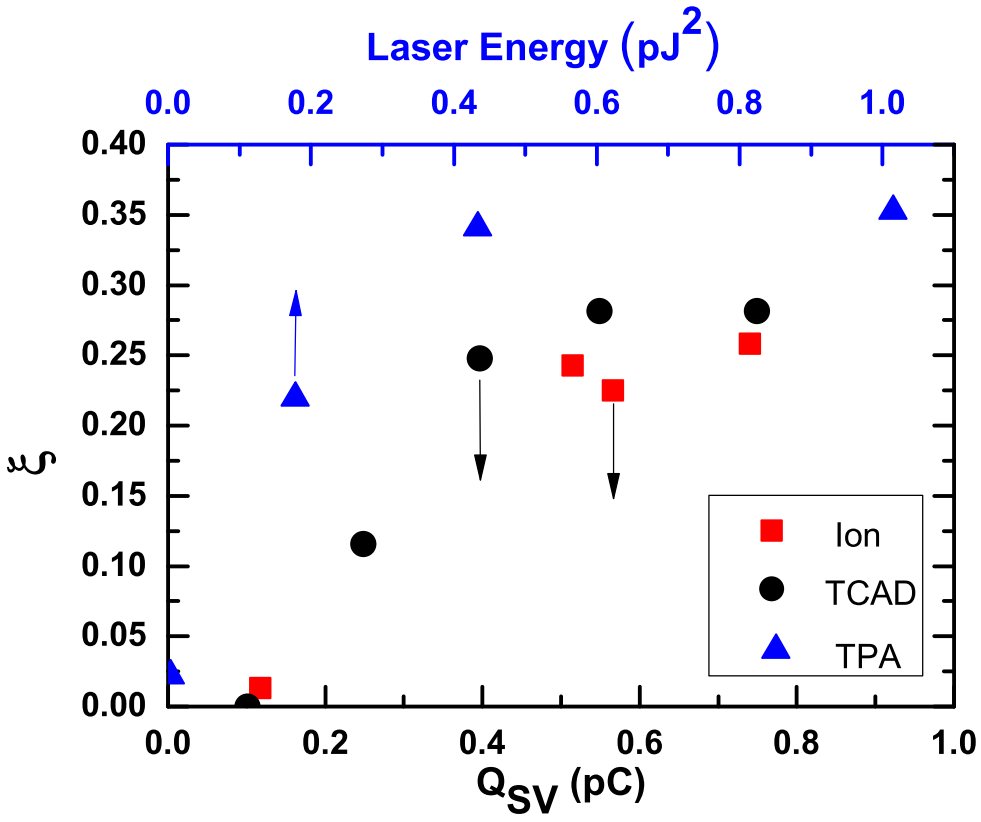

Figure 3.10: MNCC metric ξ for heavy-ion data and 3D TCAD simulation shown as function of the generated charge in a 1 μm deep sensitive volume, as well as TPA laser measurements shown as a function of laser pulse energy squared. Data show a significant increase in MNCC during TPA data collection when compared to heavy-ion data and TCAD simulations.

volume. While this has been documented before [10], a saturation of the MNCC probability occurs at high charge generation densities (Q_{SV} = 0.45 pC), which is consistent with circuit-level data obtained using flip-flops [10]. This validation is important however, because some circuits do not show this high LET saturation of MNCC [8], resulting in ambiguity about the mechanism's existence. The saturation in the probability of MNCC at high LETs demonstrates that the utility of multi-node hardening schemes may depend strongly on the particle environment for which a particular IC is intended.

The same MNCC saturation is shown in simulation data using 3D Synopsys TCAD. The location of the generated charge was scanned over the active silicon in 1 μm steps over

an origin-centered, regularly spaced grid (11 x 11), covering the experimental LET range. The output data are processed using the same criteria used for experimental ion data.

3.3 Discussion of Multi-Node Charge Collection Results

Two-photon laser experiments were performed to compare the qualitative MNCC response for laser and ion irradiation. Due to the difficulty in quantitatively comparing ion-generated and laser-generated charge values, the laser data are presented on a separate x-axis, with the laser energy squared (approximately proportional to the laser-induced carrier density). The results are shown in Figure 3.10. While Q_{SV} and laser energy squared are related, there is not a unique relationship between the quantities plotted on the two x-axes. Laser data also saturate at higher energies, consistent with the ion results, but the fraction of MNCC events is greater when compared to simulation or ion irradiation. This increase in the saturation value of ξ for TPA testing occurs because of the significantly larger generation region for laser excitation compared to ion energy deposition. The laser-generated spot size diameter is approximately 1.1 μm while that of the incident ions is approximately 100 nm [59]. Holding the generated charge density in Q_{SV} constant, the increased size of the generation region for TPA excitation decreases the distance generated carriers have to diffuse in order to be collected, and increases the probability that the generated carriers can be collected by one of the adjacent junctions.

The differences in the MNCC probabilities between ion irradiation and laser excitation need to be considered when comparing data between the two sources. The probability of MNCC may differ significantly between the two sources for the same amount of generated charge. Although the relationships between the TPA laser energy and Q_{SV} in Figure 3.10 is arbitrary to some extent, there is no scaling factor that matches the heavy-ion or simulation results exactly. In the saturation region, the probability of MNCC using TPA is 25% higher than it is for heavy-ions. Using TPA experimental data without accounting for these effects could affect estimates of MNCC in circuits that are susceptible to multi-node events, or

could lead to overestimates of improvements in circuits that use MNCC to increase their single-event reliability [14, 32].

ξ depends on the proximity of the collecting junction to the ion-generated charge. A decrease in distance between adjacent junctions, leads to an increase in the probability that more than one junction collects significant charge. This is shown in Figure 3.7; as the laser travels from a point between the corners of two adjacent junctions (heading away from center), the sum of all collected charge decreases rapidly. If the laser travels west towards J3, the sum of the collected charge increases, but all of that charge is collected on J3. This occurs because the adjacent junction, J4, is too far away to collect a significant amount of charge. This shows that with decreased scaling of CMOS circuits, these events will become more probable, and since at the 32 nm technology node, four SRAM cells can fit in between all four junctions in this layout [18], MNCC is an important issue for present and future technology nodes.

Heavy-ion measurements show a positive correlation with the incident ion and the probability that MNCC occurs, but a saturation in this trend occurs with charge generation in excess of 0.45 pC in Q_{SV}. This saturation also occurs during TPA measurements, although a 25% increase in probability exists; this value may change depending on device characteristics and circuit topology. TPA data also show the position dependence of MNCC, as well as evidence that neighboring junctions compete for the same generated charge. Ion data also show that strikes between four adjacent junctions can lead to approximately the same amount of total charge collection at all four junctions that was measured by an ion directly striking an individual junction. Experimental validation and quantification of these MNCC effects can be used for both strengthening simulation environments that are modeling multiple collecting junctions, as well as interpreting data from circuits and systems that leverage MNCC as a scheme for hardening.

CHAPTER 4

Resistive Random Access Memory

Many alternative memories are being explored as a next-generation flash memory. As discussed previously, RRAM is a prime candidate for this role, and to this point has shown a resilience to total ionizing and displacement damage effects. Chapter 4 explores the final radiation susceptibility, single-event upsets. Section 4.1 describes the device under test, followed by experimental setup details in Section 4.2. Experimental results are presented in Section 4.3, and complementary modeling techniques follow in Section 4.4. Hardening methodologies are described in Sections 4.5 and 4.6. The final section (4.7) discusses these radiation testing and simulation results for SEUs in resistive memories.

4.1 Device Specifications

The resistive element under test consists of two TiN electrodes on the top and bottom of the resistive element materials. A cross section diagram of the structure is shown in Figure 2.12a. The top layer of the element is 10 nm of physical vapor deposition (PVD) Hf, while the resistive layer of the element is 5 nm of atomic layer deposition (ALD) HfO_2. The element has a width of 105 nm and a length of 120 nm, and is located on top of the access transistor. These are similar to devices discussed in [37, 50, 56]. This is considered a digital resistive element because it has two states, a High Resistance State (HRS) and a Low Resistance State (LRS), which are analogous to a 1 or 0 in CMOS memories (Flash/DRAM/SRAM) [63].

The physical mechanisms responsible for switching the resistor's state are still under investigation, but they have been described as removal and recreation of a conductive path of Hf ions [37, 50, 56] or by the shrinking and relaxation of a conductive path formed by oxygen vacancies [64]. In this study we work at a higher level of abstraction than the exact physical origin using the phenomenological model proposed in [9-10]. This model is well

suited for the relatively high current range expected from radiation generated transients, and allows a simplification of neglecting the stochastic fluctuation of memory state as described in [65]. Both models have the RRAM in two states during normal operation: relaxed or connected, when the RRAM is in the LRS (Figure 2.12b), and constricted or disconnected when in the HRS, Figure 2.12c.

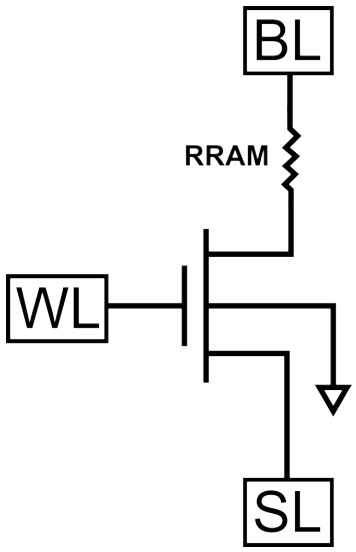

Figure 4.1: Circuit diagram for the 1T1R RRAM structure.

The resistive element is built on top of the drain of a single NMOS access transistor. In this case the transistor is built in a 65 nm process with a gate width of 1 μm and a gate length of 100 nm. The TiN electrodes are located on top of the via between the active drain diffusion and the connecting metal layer. Figure 3.1 shows a diagram of the 1T1R structure. Since the resistance change is most strongly related to the voltage across the resistive oxide [55], it is the change in voltage, not the generated current transient, caused by an incident ion that dominates the response of the RRAM. Current is of interest because of the heating effects in the oxide, but it was shown in [55] to be a less dominant mechanism than the applied voltage across the cell.

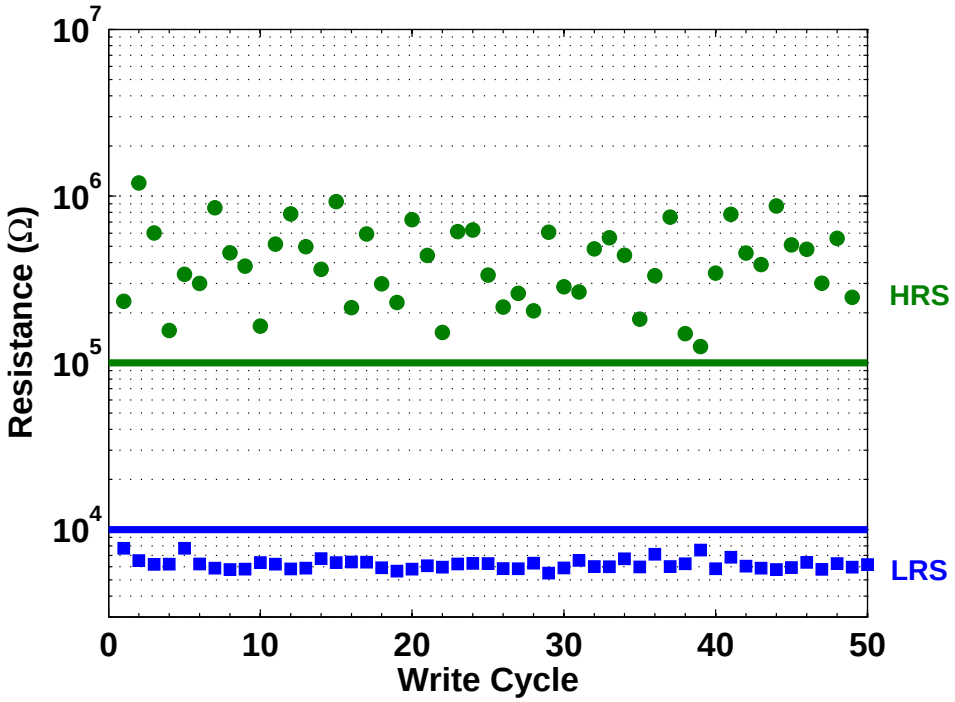

Figure 4.2: Life cycle test of the 1T1R device showing the high state (green) and low state (blue) of the memory cell.

4.2 Heavy-Ion and Laser Experimental Setup

Before single-event testing is performed, the RRAM is formed by holding the gate at 0.8 V and sweeping the voltage across the resistive element from 0 to 3 V. Detailed forming, setting, and resetting measurements are presented in [56]. Stability of the 1T1R structure was verified by repeatedly setting the storage element into the LRS and then resetting back into the HRS. SET (LRS) operation is performed by applying 1.8 V to the bit line (BL) electrode, grounding the source of the transistor, and sending a 1 V, 20 ns pulse to the gate. Conversely, the RESET (HRS) operation is performed by applying 1.8 V to the source, grounding the BL electrode of the resistive element, and sending a 3 V, 20 ns pulse to the gate. The state of the RRAM is measured by applying a 10 mV DC signal to the BL electrode, 1 V DC to the gate (word line), grounding the source (select line), and measuring the resulting current. In Figure 4.2 we show 50 samples of the SET/RESET operation

obtained with this method. The capability of this technology to reach high endurance numbers (10 M) with ns-width pulses has been shown in [56]. The metal lines connecting the RRAM to the transistor, as well as the lines connecting the test equipment to the cell contribute a minimal capacitive or resistive load on the cell when compared to the contribution of the resistive element.

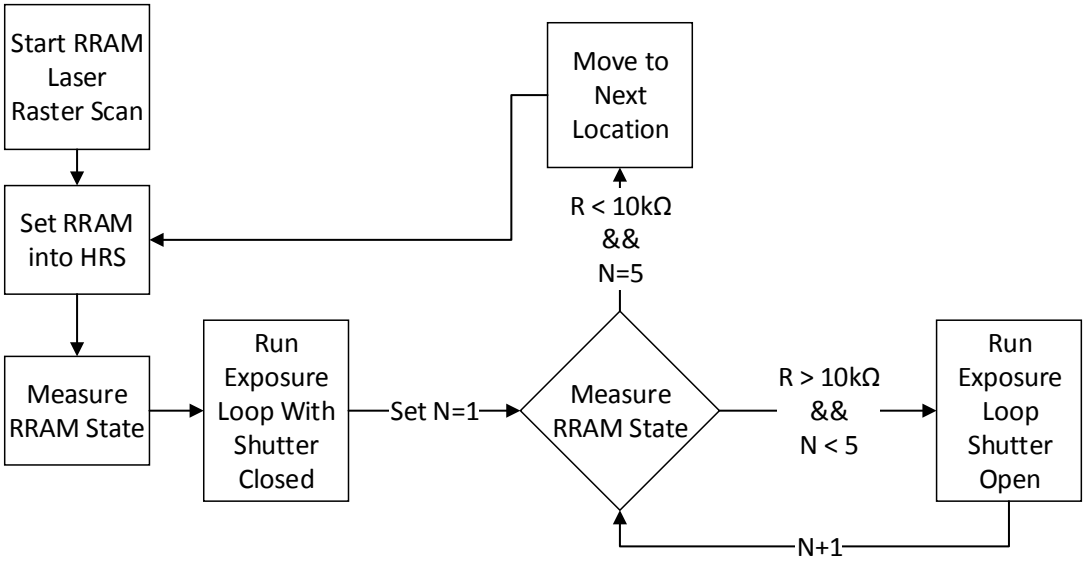

Figure 4.3: Flow chart of how heavy-ion test were performed on the 1T1R RRAM structure.

The following steps are used for single-event testing: write device to a high or low state, put it into the corresponding susceptible bias condition, expose it to a carrier generation source, and measure the state of the storage cell post-exposure. The exposure and measurement steps are repeated if no change in resistance is detected. The state of the RRAM is determined by measuring current and converting it to an effective resistance by dividing by the applied voltage. This measurement can take place without altering the state of the RRAM cell.

During heavy-ion testing, the resistive element is exposed throughout the test because the beam cannot be automatically shuttered during read/write operations. The RRAM was not susceptible when there was no voltage applied to the BL during heavy ion or TPA

testing, even for high-energy events, allowing for the present state of the resistor to be maintained even if struck by an ion. For single-event testing, the state of the RRAM is set, the resistance is measured ($\sim$1 s), V_{BL} is applied for 5 seconds, and then the resistance is measured again. If an upset occurs, the cell is rewritten into the appropriate state ($\sim$3 s). Neither read time or rewrite time are counted toward the single-event fluence. The heavy ion broadbeam flux was approximately $2{\cdot}10^7$ $cm^{-2}s^{-1}$ for all runs, which equates to an ion directly striking the transistor, on average, once per two measurement cycles. The transistor's lateral dimensions are given in Figure 4.19a. Each run consists of 72 read cycles (resistance measurements) with a write only occurring when the cell is upset. The RRAM is tested for full functionality after each run is completed.

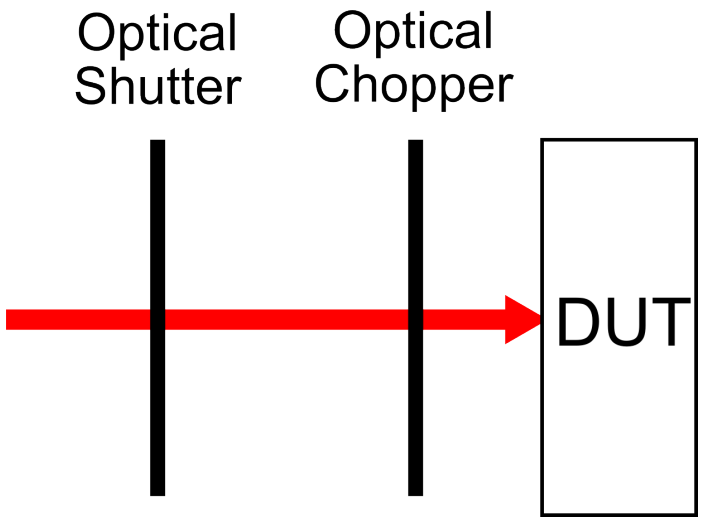

Figure 4.4: Laser source passing through an optical shutter and optical chopper during TPA single-event upset testing.

Backside TPA laser testing was carried out at Vanderbilt University, with the laser only passing through the silicon substrate. The system utilizes an optical parametric generator, which operates at a wavelength of 1260 nm, with a nominal pulse width of approximately 150 fs, and a repetition rate of 1 kHz. Generation spot size measurements [58] show 80% of the generated charge is located within 1.2 μm (circular Gaussian distribution) when using a 100x (NA 0.5) focusing objective. The 1T1R device is mounted on a high precision

linear stage, which has a minimum step size of 0.1 μm. The laser is passed through an optical chopper and automatically shuttered to limit exposure of the DUT to approximately three measurable pulses per exposure, shown schematically in Figure 4.4. The laser pulse energy is captured for each transient measurement using an InGaAs photo-diode, allowing for direct comparison of each exposure and subsequent RRAM state changes.

4.3 Experimental Results

Heavy-ion irradiations, as well as TPA area scans of the RRAM access transistor, were performed while monitoring the RRAM state and current transient response to determine the sensitive area of the device. During ion and laser testing, the RRAM never transitioned from LRS to HRS even when exposed to a large number of high energy events. This is also seen in simulation and is caused by the grounded high-resistance path of the RRAM (drain/BL) not being a favorable path for the collection of ion-generated carries. Without significant charge collection, no significant voltage is dropped across the resistive element, allowing the state to be maintained. The source (SL) collects a significant amount of charge, but will not create the voltage drop across the RRAM needed to cause a state change. For this reason, the following results concentrate on HRS to LRS transitions.

4.3.1 Device Sensitivity to Applied Voltage

Since the RRAM switching mechanism is voltage dominated, the upsets from heavy ions should have a strong dependence on the BL voltage. Figure 4.5 shows this relationship using data collected from the 10 MeV/u cocktail at Lawrence Berkeley National Lab 88-inch cyclotron. The voltage is increased from 0.6 V in 50 mV increments until an upset occurs during the test time frame (72 cycles). This is the threshold voltage for upset, and defines the minimum V_{BL} to cause an upset. The data are presented with an exponential fit, based on work from [66] which derives a simplified RRAM switching model with the following two equations.

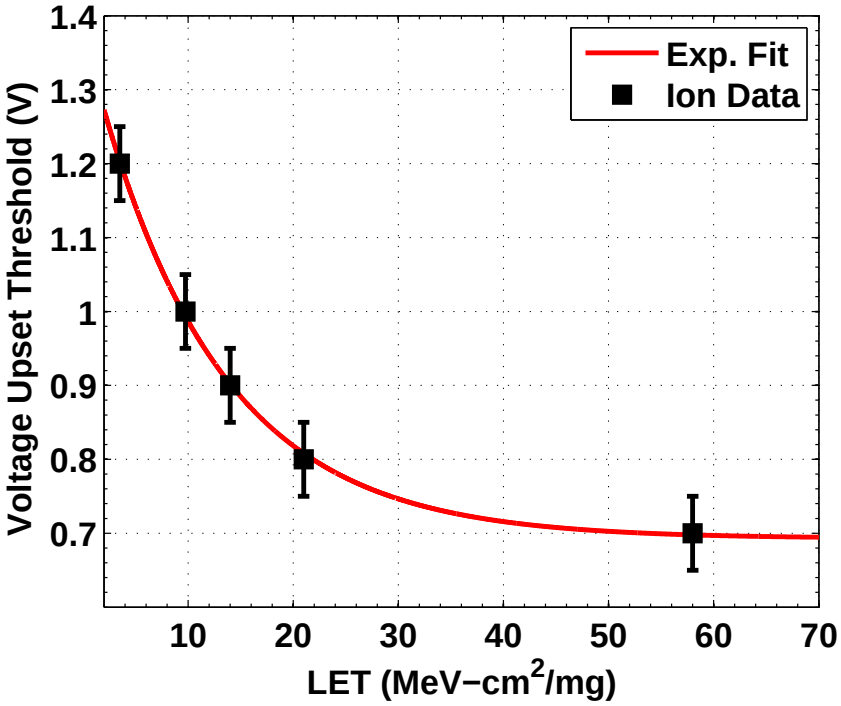

Figure 4.5: Exponential relationship between the BL voltage required to cause upsets in a single RRAM and the LET of the incident ion using three DUTs. Error bars represent experimental resolution, and the fit is $y = 0.69 \cdot e^{-0.085x} + 0.69$.

$$\frac{d\phi}{dt} = Ae^{-\frac{E_A - \alpha qV}{k(T_0 + \frac{R_{th}}{R_0}V^2)}} \tag{4.1}$$

$$|\Delta\phi| = \frac{\phi}{2} \cdot \frac{\Delta R}{R_0} \tag{4.2}$$

Variables and constants for (4.1) and (4.2) are given in Table 4.1. For single-event effects, we substitute (4.2) into (4.1) to relate the change in the resistor state to the voltage dropped across the RRAM.

$$\Delta R = \frac{A \cdot e^{-\frac{E_A - \alpha qV}{k(T_0 + \frac{R_{th}}{R_0}V^2)}} 2 \cdot R_0 \cdot \Delta t}{\phi} \tag{4.3}$$

Eq. (4.3) states that the change in resistance, ΔR, is exponentially related to the voltage

Table 4.1: Variable Declarations

Variable	Description	Value
A	Pre-exponential Constant	± 1 [66]
ϕ	Filament Width	Data [66]
E_a	Activation Energy	0.5
α	Barrier Lowering Coeff.	0.3
V	Applied Voltage	Input
t	Pulse duration	Input
$R(n)$	Present Resistance	$R_0 - \Delta R(n-1)$
R_0	Initial Resistance	Input
R_{th}/R_0	Thermal Resistance Ratio	2500
T_0	Starting Temperature	300

dropped across the RRAM. ΔR is also linearly related to the voltage pulse duration, Δt, and the initial resistance of the RRAM, R_0. The incident ion affects V and Δt, where both are correlated to the ion's LET. With an increase in ion LET, it is possible to drop more voltage for a longer period of time because of increased current pulse magnitude and duration. This results in an increase in the change in resistance, and decreases the applied voltage required to upset the cell. The voltage dropped across the RRAM is limited by the applied voltage and the built in voltage; if the generated pulses reach this voltage limit, they elongate in order to collect the ion-generated carriers. A continuation of this discussion and derivation for time dependent waveforms is given in the modeling section, Section 4.4.

4.3.2 Investigation of Single-Event Upsets

Single-event upsets occur when a single incident particle generates enough charge in a susceptible device to change its state. For the RRAM, this is a particle capable of changing the resistive element beyond its complementary state threshold (from above 100 kΩ to below 10 kΩ, or vice versa). We determine an HRS upset to be when the value of the element falls below 10 kΩ; likewise, a LRS upset would be a transition above 100 kΩ. From (4.3) the upset rate should correlate with applied voltage and ion LET.

Figure 4.6 presents the RRAM SEU cross section as a function of incident ion LET for

two BL voltages, decreasing as expected with lower ion LET and lower applied voltage, resulting in fewer SEUs. The voltage dependence is greatest at low ion LET, and there is no measurable difference between the two voltages considered here at higher LET. The convergence occurs because ΔR approaches saturation at higher LETs for both applied voltages. At saturation, the upset rate is dominated by direct hits, which all have sufficient voltage drop and duration to upset the cell. The maximum cross section in Figure 4.6 is about 30 μm^2, which suggests that there is a significant contribution from diffusive current transients, and matches well with the sensitive area given by TPA laser scans.

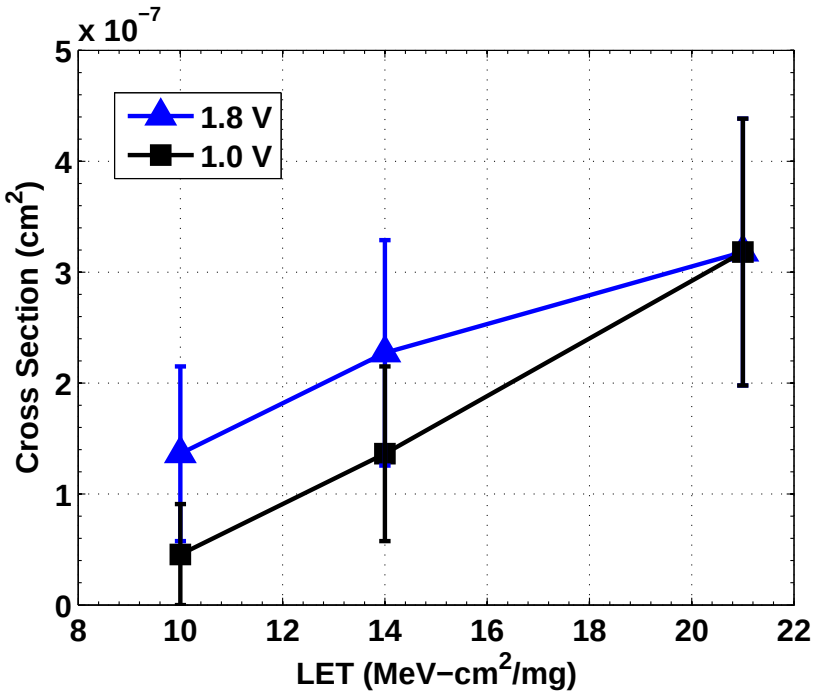

Figure 4.6: Number of single-event upsets as a function of ion LET for BL voltages of 1.0 and 1.8 V using a single sample; error bars represent standard error for Poisson counting statistics.

4.3.3 Evidence for Multiple-Event Upsets

SEUs are considered binary events where the memory cell either upsets or does not upset from a single incident particle. Particle-induced upsets are normally considered binary because the underlying memory technologies are only stable in two states, high and

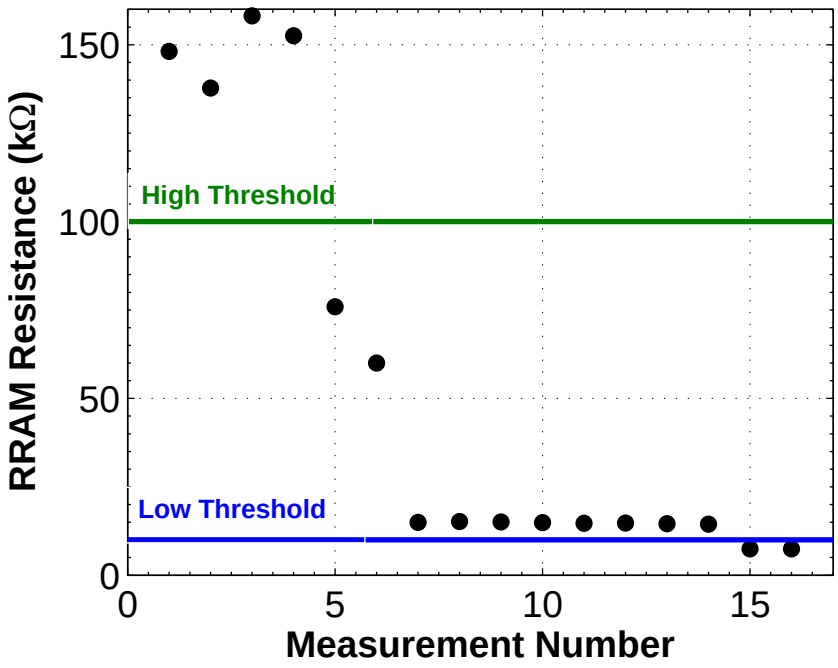

Figure 4.7: Ion-induced Multiple-Event Upset shown as a transition in between the high and low thresholds, followed by a transition below the low threshold.

low. Thus the particle either changes the memory's state, or the state remains the same. The HfO_2/Hf RRAM, like most resistive memory technologies, is stable in a continuum of states [51]. While RRAMs are typically designed to occupy two states during normal operation, abnormal write conditions from a single-event strike can cause the RRAM to occupy a state in between high and low. With no restoration current, the cell will maintain this state until a subsequent write to the cell occurs. If multiple particles strike the cell before the cell is rewritten, the combined change in resistance by each ion can upset the cell, even though each strike cannot upset the cell on its own.

MEUs appear in data plotted in Figure 4.7 where the resistor's value transitions in between the threshold for HRS/LRS. It is stable in between these two states. Two subsequent particle strikes then cause the cell to transition below the LRS threshold. This is how we separate MEUs from SEUs. There may be some error associated with this technique in that some MEUs may happen within a single measurement cycle, but the beam flux makes this

probability small.

Figure 4.8 shows the fraction of MEUs that were recorded out of the total number of upsets (MEUs and SEUs). Figure 4.8 is consistent with Figure 4.6 in that the lower applied voltage results in fewer SEUs and more partial writes to the RRAM cell, increasing the likelihood that it takes more than one particle to upset the cell. The same convergence trend is also shown between SEUs and MEUs at higher LETs, caused by the same mechanism, an increased contribution of SEUs because of an increased quantity of individual ion strikes that have the ability to upset the cell for either voltage.

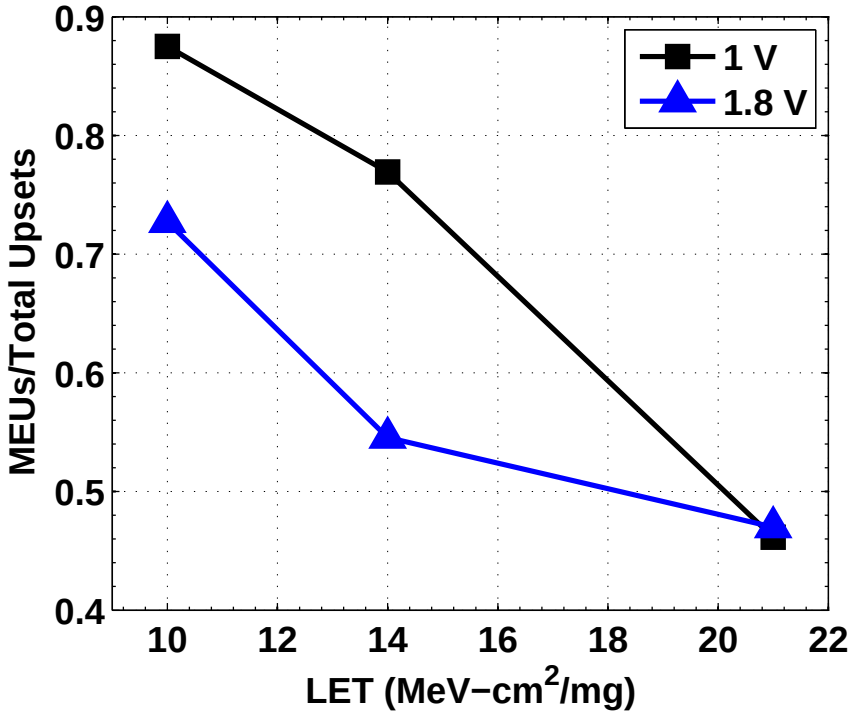

Figure 4.8: Fraction of all upsets that are Multiple Event Upsets for the same ion experiments as Figure 4.6.

The strong dependence of the RRAM's susceptibility on the applied voltage can also be seen with TPA laser analysis. Figure 4.11 plots the laser induced SEU cross section of the cell vs. the applied voltage, at a single laser energy, similar to the LET in Figure 4.8. Each measurement is an area scan of the device (6 x 6 μm in 1 μm steps). Unlike ion measure-

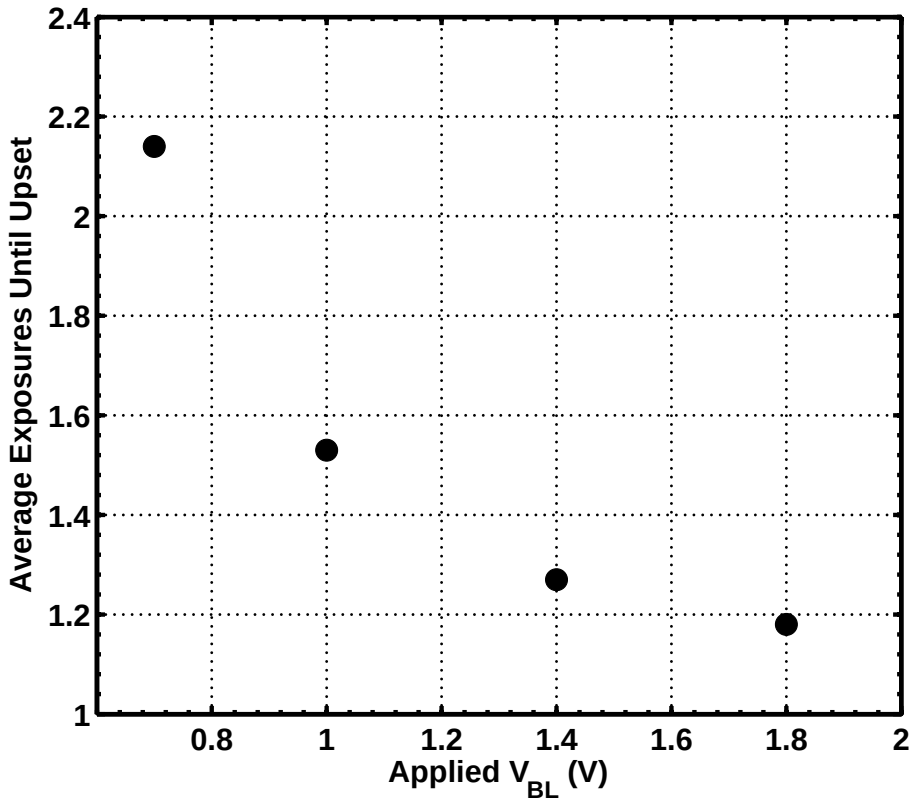

Figure 4.9: Average number of laser exposures required to upset the RRAM for identical area scans with different BL voltages.

ments, the laser is physically shuttered from exposing the device unless it is opened. The sensitive area is reduced by 2.5 times at 0.7 V when compared to the nominal SET/RESET voltage of 1.8 V. It should be noted that the RRAM did not upset for voltages less than or equal to 0.65 V, even for very high laser energies. The exponential increase in cross section with the applied voltage, as well as the minimum applied voltage required for upset correlates well with ion data, and shows that applied voltage is a dominant factor in the RRAM's sensitivity.

4.3.4 Cell Sensitivity Based on Strike Location

Besides the ability to rapidly shutter the source, a major advantage of laser measurements is the ability to control the position of the carrier generation. The strike location can

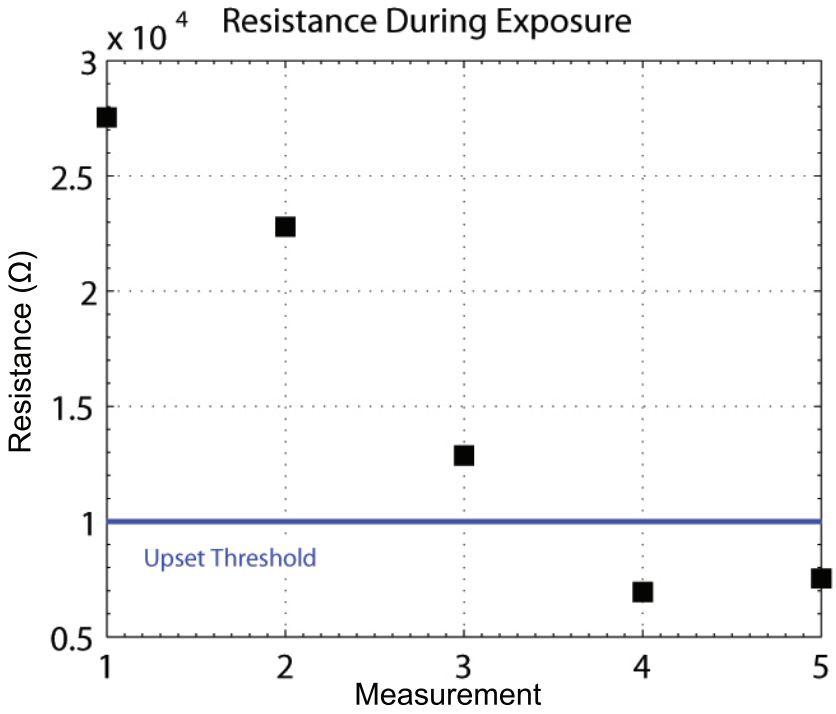

Figure 4.10: Change in resistance after subsequent exposures during TPA testing, with the cell finally upsetting after four exposures.

strongly affect the characteristics of the current transient; strikes inside the depletion region of a biased diffusion (source or drain) respond with a high magnitude short duration transient for low level energy deposition [17], and can also create large magnitude, much longer transients for high levels of generation [59]. Strikes in the channel can cause bipolar-like gain [67], or strikes in unbiased diffusions can cause complicated transients that collect or inject carriers at different points in time. Lastly, strikes outside of any active diffusion can, in bulk CMOS, diffuse over distances of several micrometers to generate transients that are much lower in magnitude, but longer in duration, than direct hits to active diffusions [59].

The variety of possible responses complicates testing in facilities that have random isotropic flux (e.g., broadbeam ion), but comparing to TPA laser data can be useful for understanding the position correlated response of the RRAM. Since the laser source is passed through both a shutter and chopper, it is possible to look at how a limited exposure

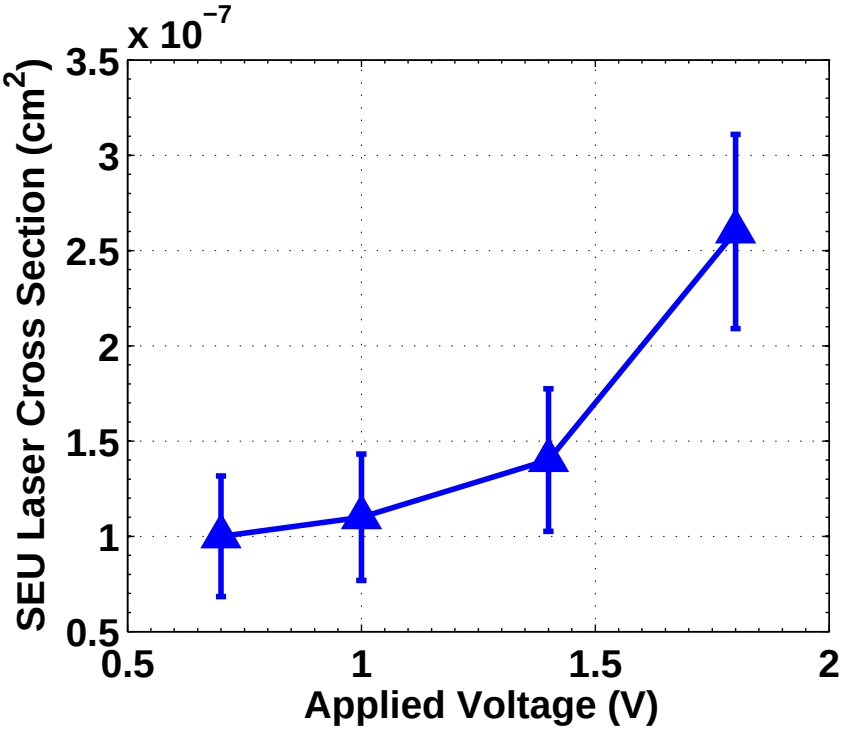

Figure 4.11: Measured TPA laser sensitive area of the RRAM at different applied voltages for a single sample; error bars represent standard error for Poisson counting statistics.

can alter the RRAM state at each position. Figure 4.12 shows the number of exposures it took to upset the RRAM, as a function of laser position. Data capture locations are positioned where dashed lines intersect, and are plotted as 1 μm squares, which was the X and Y step size for the scan. The upset threshold is chosen to be 10 kΩ, the LRS threshold. It is likely that for low magnitude pulses, it may require two or more pulses to upset the RRAM, with the pulses being cumulative in effect, and following the same exponential voltage to resistance change relationship in (4.3). The applied voltage is on the BL, and ΔV across the RRAM is a combination of this voltage and the built in voltage dropped across the RRAM due to a generated current transient.

Figure 4.12a shows the sensitive region with an average laser energy of 212 pJ. Most upsets are from the first exposure, with a few fringe locations that took more than one exposure to upset. For an energy of 406 pJ, Figure 4.12b, both the area of first-exposure

upsets, and that of multiple-exposure upsets increases. There is some spatial translation between these two figures, meaning they do not have the same scan origin. The increase in multiple-exposure upsets shows that the increased energy resulted in more significant diffusive transients (generated outside the active diffusions); these are transients that are lower in magnitude (lower voltage drop across the RRAM), but still have the ability to cause RRAM state changes without meeting the upset criteria.

Pulse to pulse variations from the laser source cannot be eliminated using variance reduction techniques often employed for single-event current transient capture. This can cause unwanted variance where it appears that fringe locations are more sensitive than locations closer to the transistor (e.g. Figure 4.12b X=6 Y=2). This is caused by large pulses being generated above the normal pulse energy, and cause an upset that would not occur with the average generated laser pulse. Several different RRAM die were tested with similar results, with the laser source variance dominating any differences seen during scans. This correlates well with the simulation data, and is presented in more detail in Section 4.4.2.

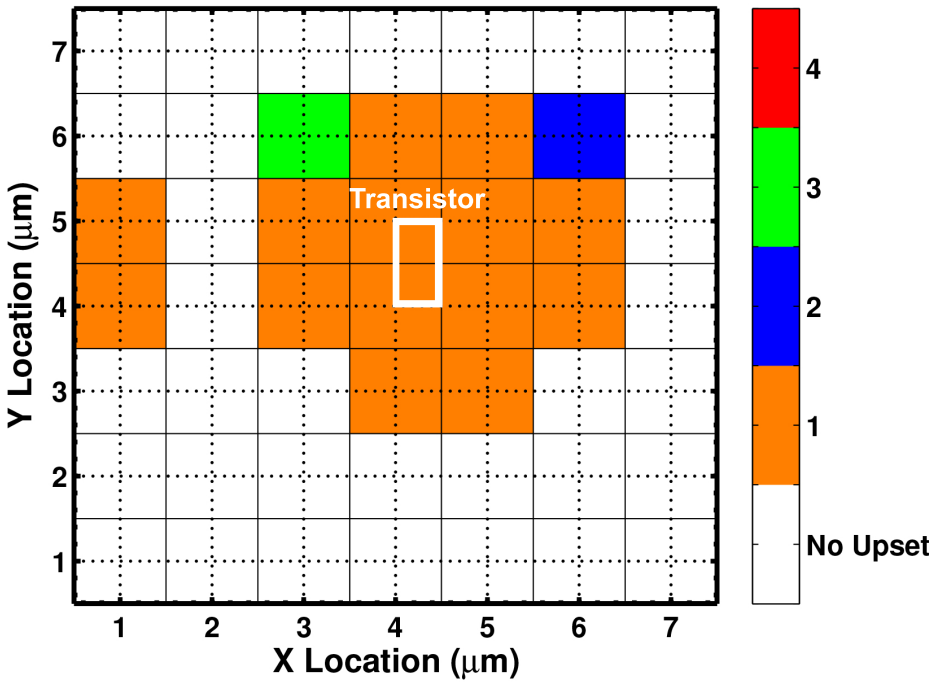

(a) 212 pJ.

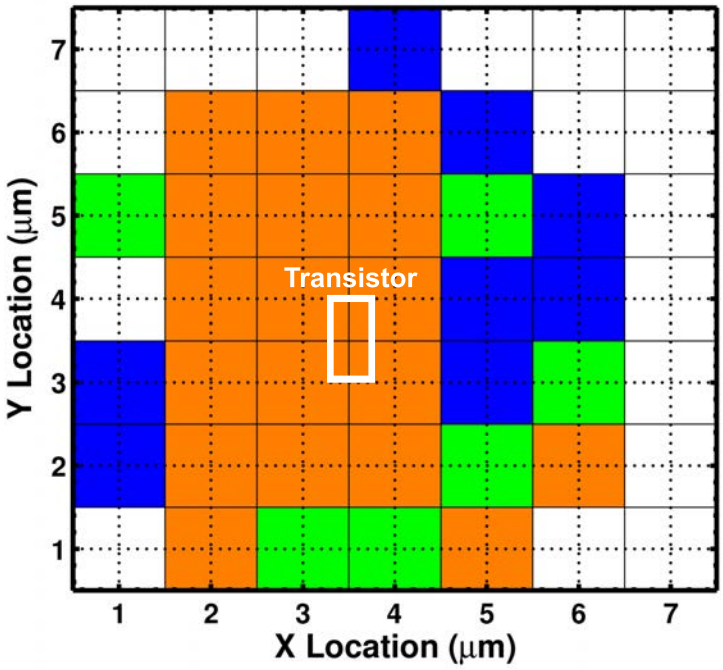

(b) 406 pJ.

Figure 4.12: TPA laser area scan at two laser energies showing the number of laser exposure to the RRAM access transistor until the cell falls below the upset threshold. Direct strikes to the transistor result in SEUs, while diffusive transients require multiple exposures to upset the cell.

4.4 Resistive Random Access Memory Modeling

4.4.1 Modeling of Oxide-Based Resistive Elements

The RRAM can, and most likely will, be manufactured on a variety of access-transistor technologies; given that the access transistor is the source of SEUs, modeling the RRAMs response to single-event induced transients is crucial to predicting its reliability in future technologies. The relationship given by (4.3) can be visualized by looking at the change in resistance as a function of the applied voltage pulse. Holding the initial resistance of the RRAM constant (150 kΩ), the theoretical voltage magnitude and pulse duration were varied to produce the plot in Figure 4.13. The initial resistance is chosen as 150 kΩ to represent the lower HRS states seen due to part to part variability. The lower resistance will require less change in state to reach the LRS, and is chosen as a conservative estimate of sensitivity. The red region in Figure 4.13 is where pulses are large enough to guarantee an upset from HRS to LRS. Orange, yellow, and light blue areas show a significant resistance state change of the RRAM, but do not cause the RRAM to fall below the LRS threshold. These regions demonstrate the possibility for partial upsets due to abnormal writes, and the ability of multiple events to contribute to an MEU.

Eq. (4.3) assumes a square pulse of constant magnitude. For time-varying waveforms, individual changes in resistance can be computed for each time step, and summed to calculate the total change in resistance, Eq. (4.4).

$$\Delta R = \sum_{n=1}^{m} \frac{2A \cdot R(n) \cdot \Delta t(n)}{\phi} \cdot e^{-\frac{E_A - \alpha q V(n)}{k(T_0 + \frac{R_{th}}{R_0} V(n)^2)}} \tag{4.4}$$

Starting values for constants in Table 4.1 were used from [66], but were refined experimentally to obtain the values shown. A high speed function generator (AFG3252) was used to generate Gaussian voltage pulses of 1 V magnitude with different durations (4-12 ns FWHM) on the gate of the access transistor. V_{BL} was biased from 1 to 1.8 V in order to control ΔV across the resistor. The RRAM was measured before and after a generated pulse using an HP4156, and was reset when the resistance fell below 10 kΩ. Figure 4.14

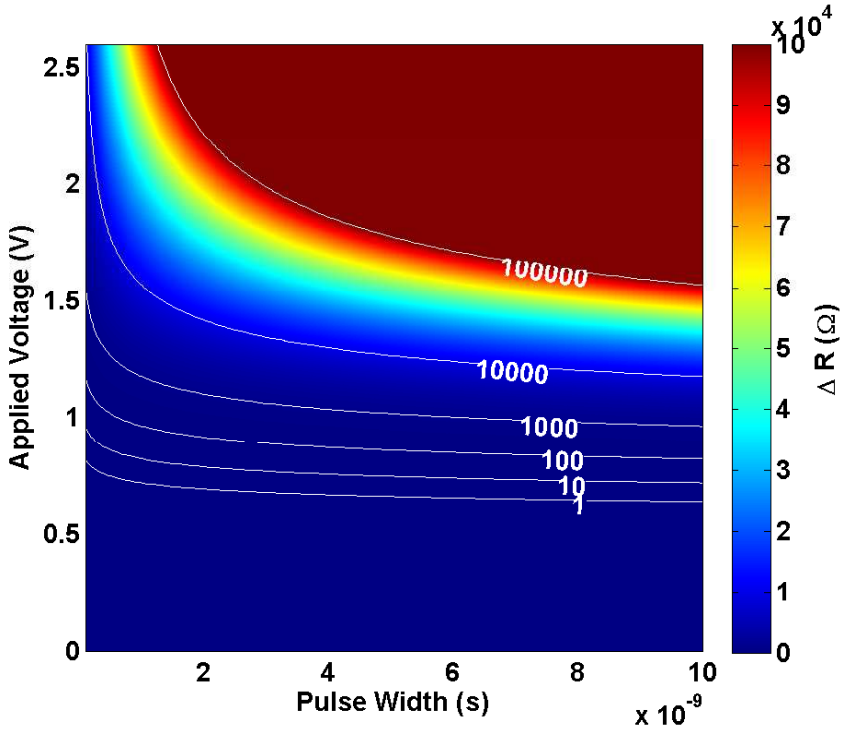

Figure 4.13: Change in the RRAM resistance as a function of the applied pulse magnitude and duration.

shows the result of two of these measurements (1.2 and 1.4 V, 4 ns pulse). This test was run on a single device, with this particular device having a series of high starting resistance values, which happens occasionally, and is commonplace for a still-maturing process. The red line represents calculations using (4.4). Values were selected such that the model produces conservative estimates in all cases, sometime resulting in slightly higher values of ΔR than the experiment. These parameters along with (4.4) are used in the following section to simulate heavy ion strikes.

There are inherent limitations to calculating the resistor's state change in post processing, typically causing an over prediction of the cell's sensitivity. A comparison of the two methods is shown in Section 4.4.2. 3D device simulations were performed using Synopsys TCAD [60], and the dynamic model was implemented using the Compact Model Interface (CMI). The CMI uses a user defined input/output matrix as well as a Jacobian matrix to

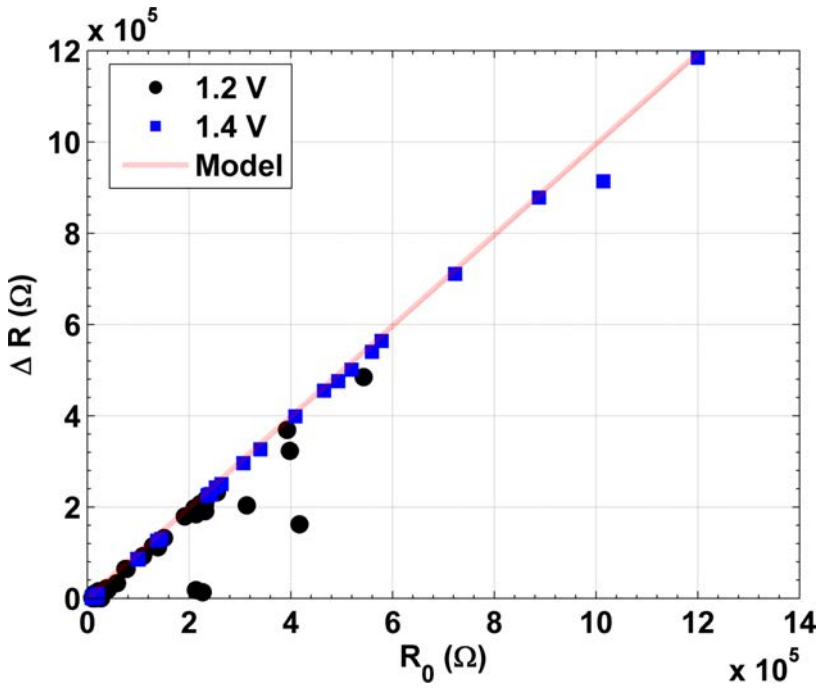

Figure 4.14: Experimental verification of the input parameters for Eq. 4.1 listed in Table 4.1 for a pulse width of 4 ns.

communicate between the model's calculations and device simulations. The input matrix (4.5), output matrix (4.6), and Jacobian matrix (4.7) are given by the following.

$$z(t) = \begin{bmatrix} u_1 \\ u_2 \\ i \end{bmatrix} \tag{4.5}$$

$$f_R(t, z(t)) = \begin{bmatrix} i \\ -i \\ (u_1 - u_2 - R \cdot i) \end{bmatrix} \tag{4.6}$$

$$\frac{d}{dz} f_R(t, z(t)) = \begin{bmatrix} 0 & 0 & 1 \\ 0 & 0 & -1 \\ 1 & -1 & -R \end{bmatrix} \tag{4.7}$$

u_1 and u_2 are the BL and drain electrode voltages on each side of the resistive element. i is the current flowing through the element from BL to drain, and R is given by:

$$R = R(n-1) - \frac{2A \cdot R(n) \cdot \Delta t(n)}{\phi} \cdot e^{-\frac{E_A - \alpha q V(n)}{k(T_0 + \frac{R_{th}}{R_0} V(n)^2)}} \tag{4.8}$$

R(-1) is the initial resistance and is called R_0 throughout this document. The compact model is instantiated as a circuit element during mixed-mode TCAD simulations. The resistive element is connected between an ideal voltage source (for V_{BL}) and the drain of the 3D transistor model. During each time step of the simulation, the resistor's state is solved simultaneously with the differential equations that describe the transistor's operation. During this process, the resistor is treated as a 'black box' where the simulator sends values to the compact model, and values are returned, without any understanding of what calculations are performed inside the model. The code used to implement the model is located in Appendix B.

4.4.2 RRAM Heavy-Ion Simulations

The importance of using a dynamically varying model is demonstrated in Figure 4.15; the constant-resistance modeling technique over predicts the sensitivity of the RRAM when compared to a dynamic compact model simulation using an identical access transistor structure. Both models give the same results until 1 ns, when the dynamic-resistor model has decreased enough in resistance to collect all of the ion-generated charge, and end the event. Conversely, the static model continues to have substantial changes in its state due to its higher value of R_0, and results in an over prediction of the memory element's sensitivity

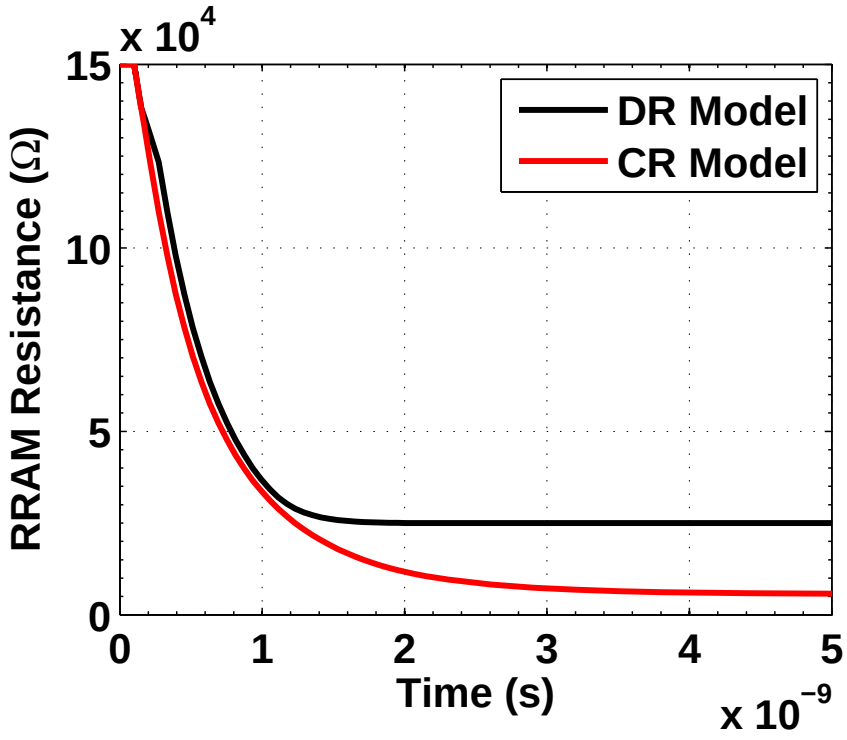

Figure 4.15: Comparison of the change in the RRAM resistance when modeling the device with a dynamic resistance model (DR) and a static resistance model (CR).

by almost 20 kΩ. For this example case, the static model's over prediction suggests that an upset will occur, although the more accurate model suggest that is will not.

The heavy-ion simulations were performed on an NMOS transistor with W=1 μm, L=100 nm with source and drain diffusions that are 1 x 0.2 μm (from fabrication information on the device under test, and shown in Figure 4.16). The nMOSFET was calibrated to match the fabricated transistor's IV characteristics. The drain is loaded with a 150 kΩ resistor to emulate the RRAM. This resistance in the TCAD simulation is constant, which is not a perfect representation of the experiment, but is a good estimate of the cell's response. It is also a conservative estimate because holding R constant causes ion-generated carriers to be collected slower, resulting in a longer voltage pulse, and ultimately a larger calculated value of ΔR. Various locations (shown in Figure 4.18a), LETs (10, 40, and 55 MeV-cm^2/mg), and RRAM bias voltages (1 and 1.8 V) were chosen to demonstrate the response under varying

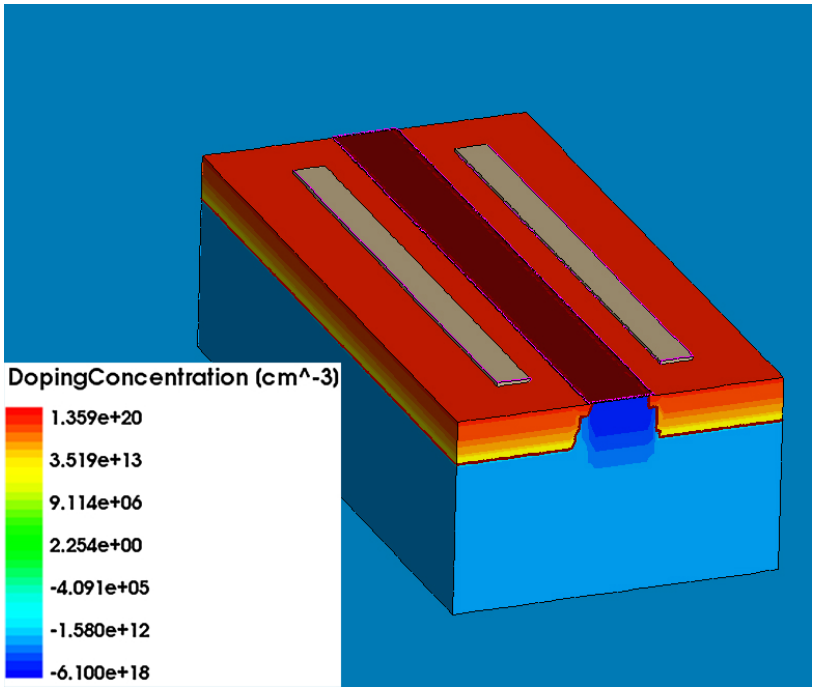

Figure 4.16: Angled topside image of 3D TCAD structure used for simulation.

conditions.

Figure 4.17 shows a voltage waveform for a simulated ion strike on a device in Synopsys TCAD [60]. The ion strikes the center of the reverse biased drain (1.8 V), with an LET of 55 MeV-cm^2/mg. The voltage waveform across the RRAM is plotted because it is the driving mechanism behind changes in the RRAM resistance; this is different from typical electronic circuits where current is typically the dominant upset criteria. Because the change in resistance is exponentially related to the applied voltage, large changes in resistance occur for voltages in excess of 1.5 V, while the rest of the voltage transient is of little significance. Note that the peak ΔV reported in simulation is the BL voltage (1.8 V) plus the built-in voltage ($\cong$ 0.8 V).

Results from CR simulations are shown in Figure 4.18, and demonstrate the strong dependence on location, voltage and LET. With an LET of 10 MeV-cm^2/mg, a well-reported trend in bulk CMOS junctions is shown whereby the most susceptible location is the center of the reverse biased drain. However, this trend changes for higher energy deposition,

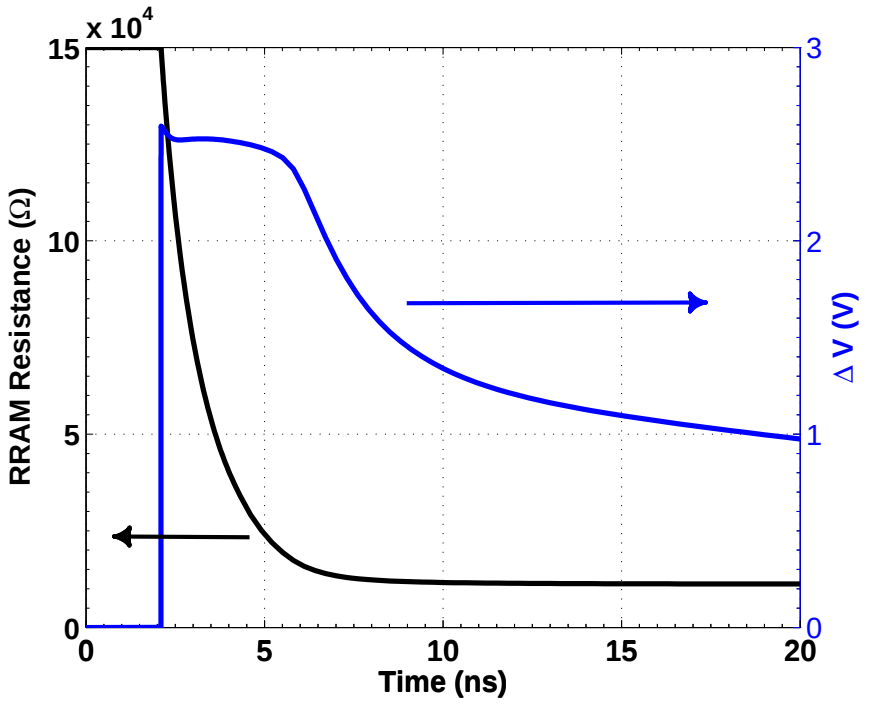

Figure 4.17: Ion generated voltage pulse across the RRAM (blue) as well as the RRAM resistance (black) that is calculated post simulation using Eq. 4.4.

resulting in an equally sensitive location outside of the drain (1 μm) for 55 MeV-cm^2/mg. This occurs due to the heavily loaded drain (150 KΩ) being pulled below the potential of the lightly loaded source, making the source a more favorable path for collection of the generated carriers. As the strike location moves towards 2 μm, the distance the carriers must travel to the source increases, increasing the time the drain has to collect those carriers, resulting in a longer voltage pulse on the drain; this ultimately causes a larger change in resistance for the RRAM.

Near position -2 μm, ΔR decreases, due to the increased distance the carriers must diffuse and the closer proximity to the source. Another well-reported trend in CMOS transistors is that increasing the ion's LET increases the magnitude and duration of current transients, which increases the change in resistance. An increase in LET dependence is also shown with increased distance from the drain diffusion. This increase is controlled by the amount of charge that is collected on the drain, the time over which it is collected,

and the peak voltage dropped across the RRAM. Since ΔR is exponentially related to the voltage across the RRAM (4.3), relatively small changes in ΔV can have large effects on ΔR. Also, ΔR is a self limiting process since the resistance cannot fall below the 5 kΩ range for short pulses, so it will also eventually saturate with sufficiently large voltage pulses.

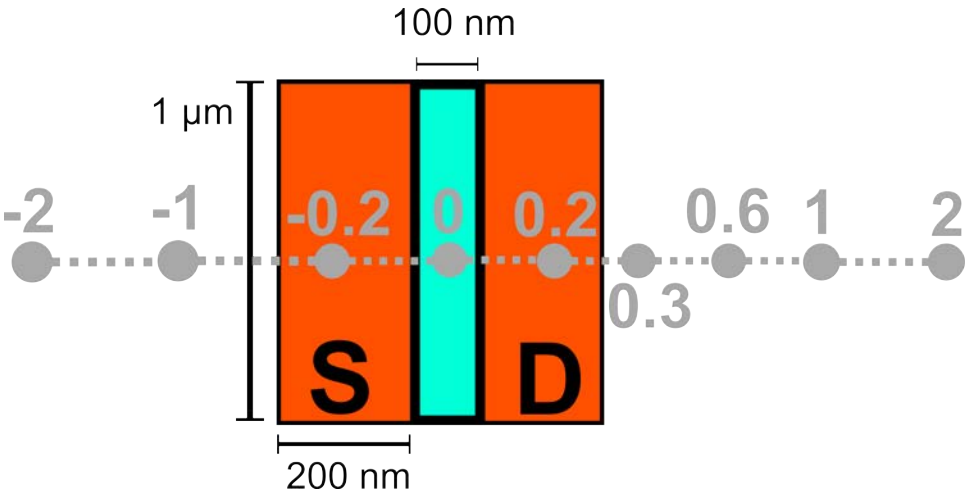

(a)

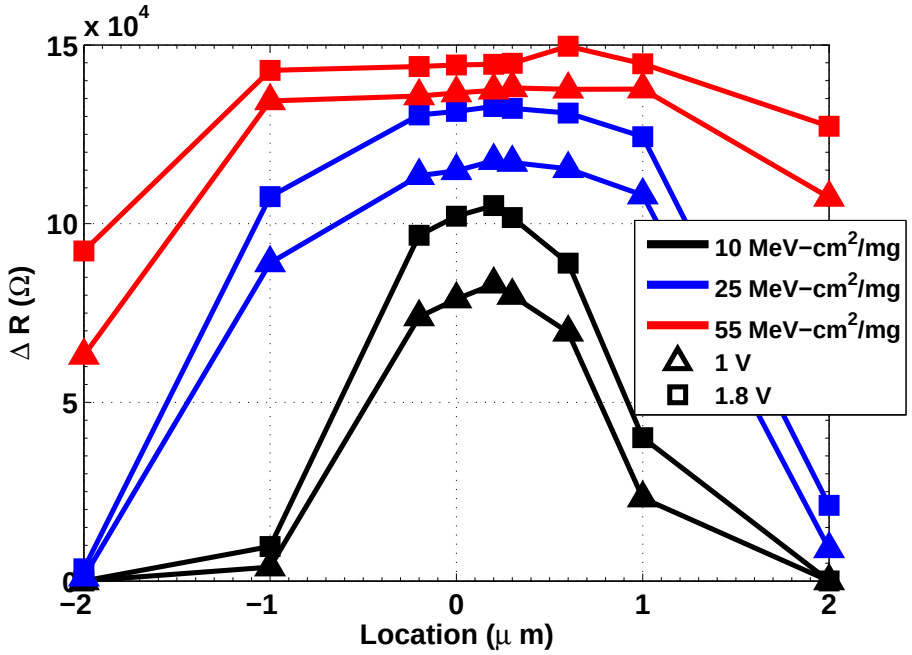

(b)

Figure 4.18: (a) Top side view of the access transistor, with locations of simulated ion strikes shown in gray. (b) The change in resistance as a function of applied voltage, ion LET, and position using the constant resistor modeling method.

A more detailed comparison of the CR and DR simulation methods is shown in Figure 4.19 for ion strikes occurring at multiple locations. The main trends seen in the CR simulation method hold true when the simulations are run using the DR method. There is a major difference however, in the two methods in the gradual and natural slope associated with strikes occurring outside of the transistor, with the DR method having a smoother roll off as ions strike farther from the cell. The CR model also over predicts the cell‘s susceptibility for strikes directly hitting the transistor, while under predicting diffusion transients that are generated outside of the transistor.

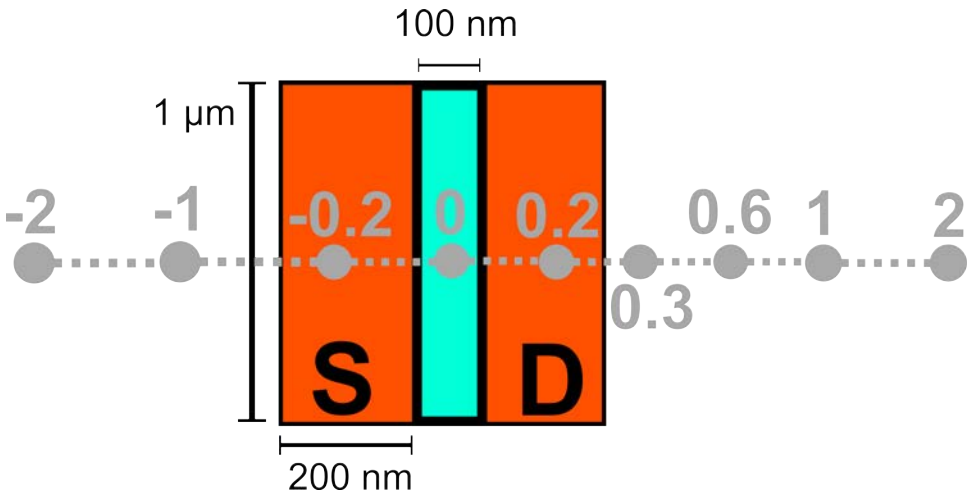

(a)

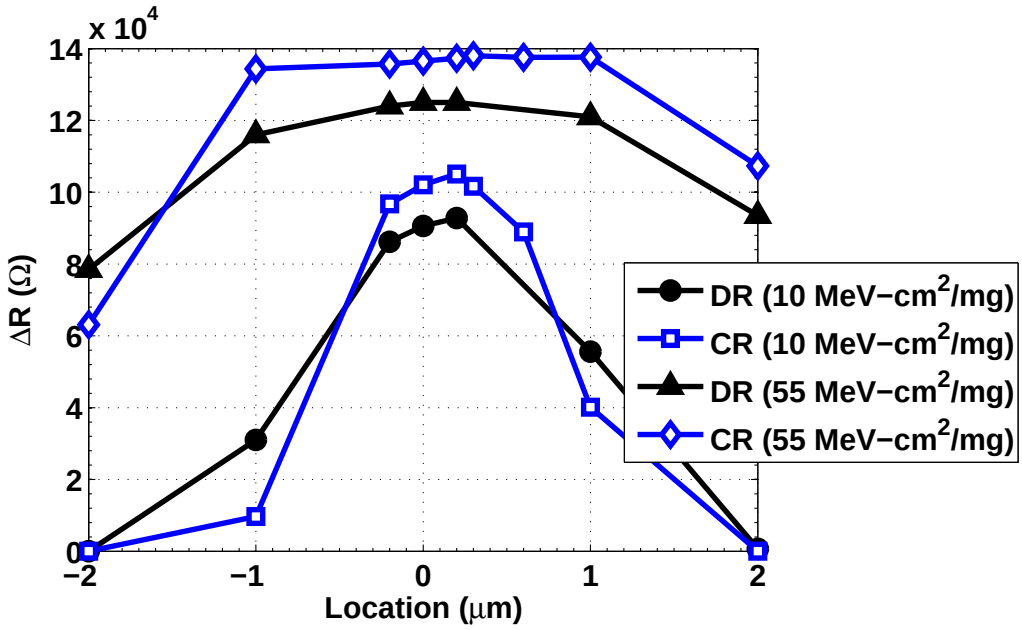

(b)

Figure 4.19: Reduction in the RRAM's resistance as a function of ion LET and strike location, for constant-resistance (CR) and dynamic-resistance (DR) simulations.

Simulations were also performed with the resistor in the LRS with the source reverse biased while the bit line connected to the RRAM was grounded. In this bias condition, the RRAM can change from the LRS to the HRS if the gate is activated. Even with the maximum applied voltage of 1.8 V, the generated current pulses were too low in magnitude to cause the RRAM to upset. The change in resistance was approximately 100 Ω, which would require much more than 1,000 worst-case events (high applied voltage, high LET) to upset the cell, making its contribution to the upset rate of the device extremely small for even the most extreme of radiation environments. Attempts were made to confirm this susceptibility in experiment, but were never able to significantly alter the cell's state even for a large number of high energy TPA events.

The DR model can also be used to simulate MEUs in the RRAM cell, which have been shown here to be a significant contributor to the tested upset rate. MEUs were simulated on the fabrication matched transistor cell by striking the same location repeatedly with the same ion-generated charge. After each simulation completes, the resistors value is maintained in the following simulation. This operates in the same way as the experimental device, where the cell's state is maintained between subsequent ion strikes. Figure 4.20 shows simulation results which have the same trend that was seen in experimental data in Figure 4.7, where the first strike transitions the cell between the high and low thresholds. The first strike has a large change in resistance, and subsequent strikes have a lessening effect. Each subsequent strike transitions the cell less than previous identical strikes. For the presented simulation example, it took four subsequent strikes to upset the cell. The strong dependence on the resistor's initial state is expected because the change in the resistor's state is linearly proportional to both the RRAM's resistance and the duration of the write pulse. It is also exponentially dependent on the voltage magnitude of the pulse. All three of these factors are effected during a single-event strike when the resistance of the RRAM changes.

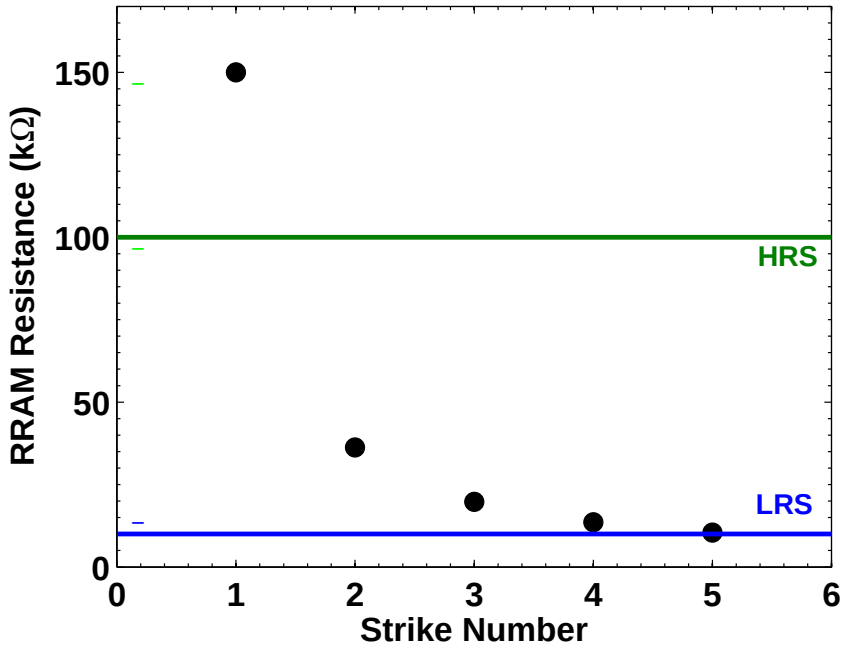

Figure 4.20: MEU demonstrated in the 1T1R RRAM structure by repeatedly striking the same cell until the value falls below the upset threshold (10 kΩ).

4.5 Window of Vulnerability of Unhardened RRAM Cells

The RRAM is susceptible to ion-induced upsets when a voltage capable of writing to the device is applied to the off state 1T1R RRAM. The amount of time the RRAM is in this state will be significantly less than the operational time of the device, and varies significantly depending on the application. The following is an estimate of the fraction of operational time that the RRAM would be vulnerable. The equation for estimating the vulnerability window (not the upset rate (SER) or failures in time (FIT)) is:

$$Vul.\,Window = State \cdot \frac{rows}{bit\ lines} \cdot Activity \cdot Time. \tag{4.9}$$

For a 1 MB example, if we choose 1024 rows, 1024 bit lines, an activity ratio of 0.01, and an equal probability of the RRAM being in HRS or LRS (0.5 because the RRAM is not vulnerable in LRS):

$$Vul.\,Window = 0.5 \cdot \frac{1024}{1024} \cdot 0.01 \cdot Time \tag{4.10}$$

Thus the window of vulnerability would be 0.5% of its operation time, which is orders of magnitude lower compared to unhardened memories which are always vulnerable (DRAM/SRAM/Flash). This is promising for the possibility of RRAM being used in radiation environments. RRAM susceptibility is directly proportional to the current transient generated by the access transistor, and single-event transients decrease in magnitude and duration as technology scales [68], so RRAMs should be relatively robust in a variety of radiation environments.

4.6 Hardening Methodologies for RRAM Technologies

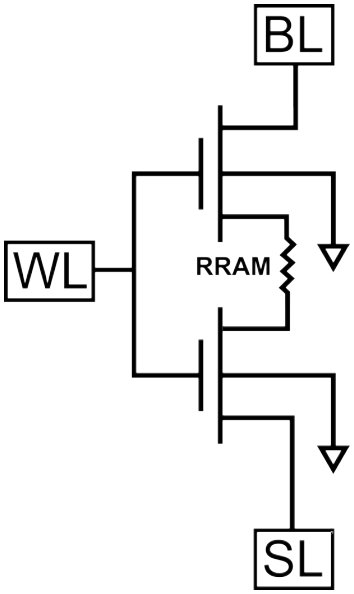

Figure 4.21: Circuit diagram of the hardened RRAM cell used in simulation.

The upset sensitivity is a direct result of the applied voltage to the memory cell. Hardening the cell to single-event strikes is as simple as disconnecting the applied voltage when the cell is dormant. One way to accomplish this is by adding a second transistor to the cell [69]. We simulated this setup using matched transistor model to the 1T1R fabricated cell,

but with a second transistor added (shown schematically in Figure 4.21). Both transistors turn on/off together, and in the off state there is no voltage applied to the RRAM.

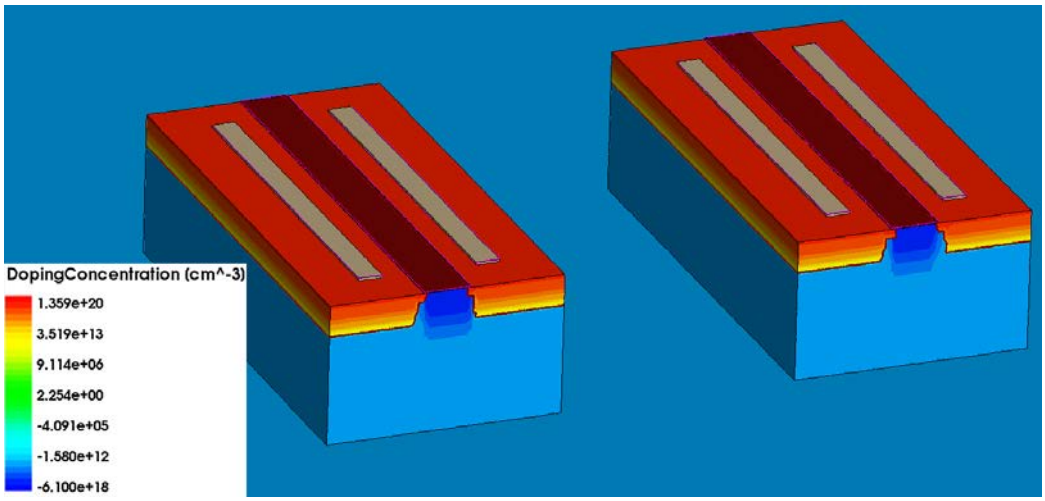

Figure 4.22: Angled topside image of 3D TCAD structure used for hardening simulation.

The electrostatic potential of the simulated off-state device, with the BL enabled (1.8 V), from Synopsys TCAD is plotted in Figure 4.23a. Normal incidence strikes for an LET of 1, 25, 50, and 100 MeV-cm^2/mg were simulated across both transistors with a peak sensitivity of 14 Ω at X = 0.5 μm. This means that thousands of events with an LET of 100 MeV-cm^2/mg would need to directly hit the access transistor, while it is biased in a vulnerable state, before an upset becomes possible.

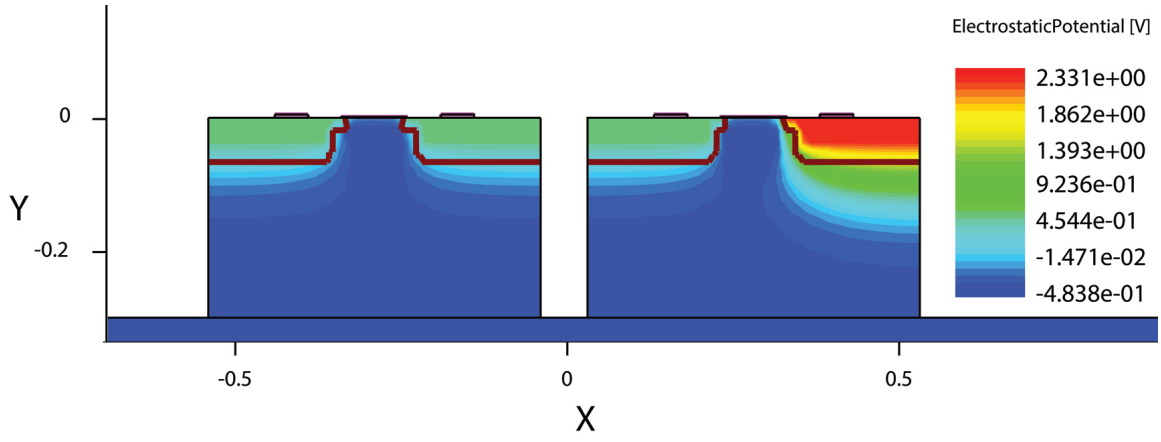

(a)

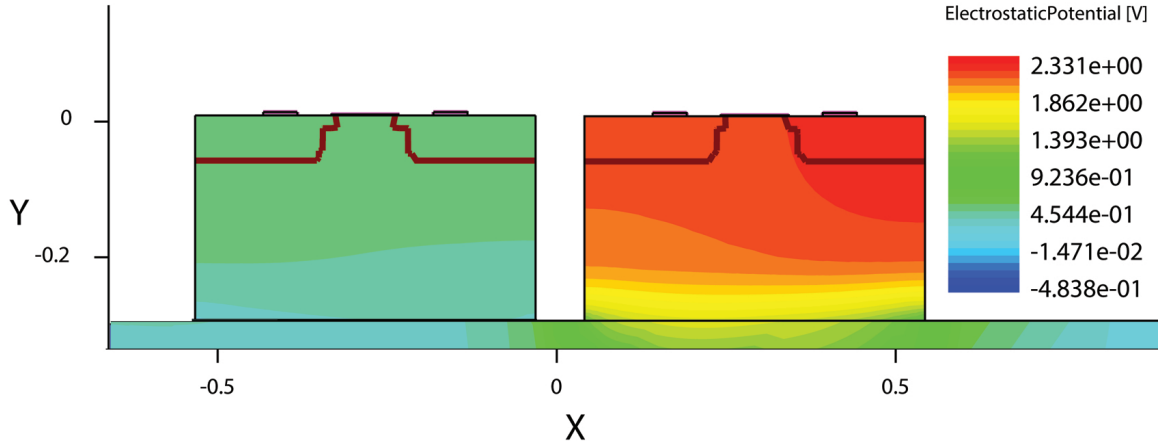

(b)

Figure 4.23: Pre-strike (a) and post-strike (parallel to the surface) (b) electrostatic potential from 3D heavy-ion simulation in Synopsys TCAD.

Strikes parallel to the surface were also simulated, increasing the susceptibility of the cell. By generating enough charge in both transistors, the applied voltage is dropped across the resistive element. This is shown in Figure 4.23 as the electrostatic potential from 3D TCAD device simulations. The simulated ion has an LET of 55 MeV-cm^2/mg and passes through both transistors. The post-strike potential shows that both transistors are shorted by the ion-generated charge, and the strike causes a substantial voltage differential across the resistive element. Unlike the normal incidence strikes, this can cause a significant change in the resistive element, and is a strong function of the incident ion's LET. The change in the resistance of the the RRAM as a function of the ion's LET is shown in Figure 4.24.

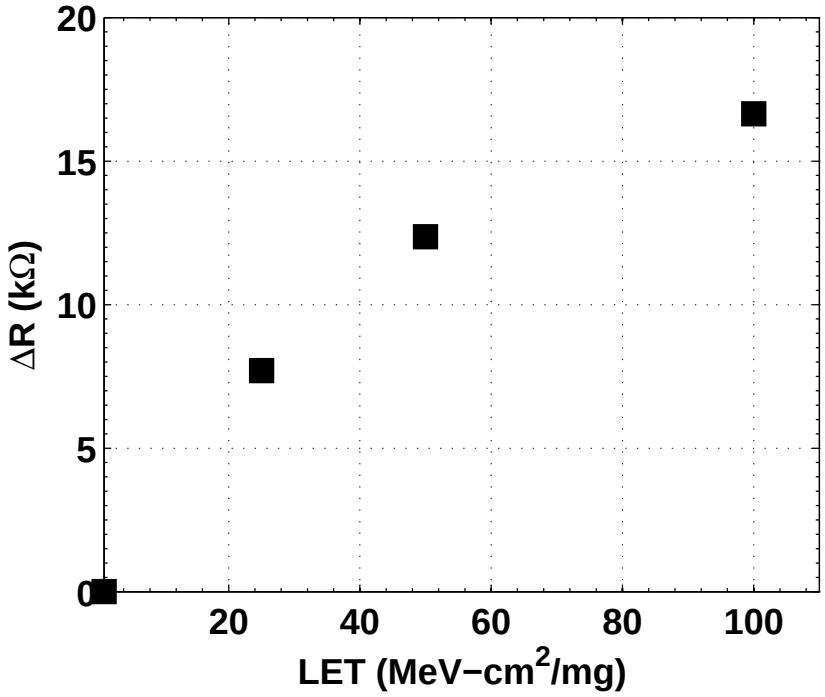

Figure 4.24: Change in the state of the resistive element after a parallel to the surface strike is simulated.

Even for a strike perpendicular to the surface with an LET of 100 MeV-cm^2/mg, the resistive element changes about 16 kΩ from its nominal state (approximately 150 kΩ). To upset the cell, nine consecutive worse case events, occurring during the window of vulnerability, would have to occur to upset the cell. The need to have 9 correlated events in

order to upset the cell demonstrates the strong radiation tolerance that can be gained with a relatively simple hardening scheme.

4.7 Discussion of RRAM Results

This chapter encompassed the first published measurement of a heavy-ion induced memory upsets in resistive memories. The upset mechanism, a voltage pulse generated from the collection on ion-generated charge, is similar to mechanisms that drive upsets in other commercial memories (SRAM/DRAM/Flash). However, several mechanisms are unique to RRAM cells such as the exponential dependence on the applied BL voltage and the limited window of vulnerability of the cell. In SRAM cells, an increased operating voltage usually shows a more robust SEE response than the same cell operated at a lower voltage. This trend is reversed in RRAMs where the lower the BL voltage, the lower the sensitivity. The other most distinguishing difference is the ability to create Multiple Event Upsets, where subsequent particle strikes can accumulate and finally culminate in an upset of a cell due to lack of a restoration force.

These mechanisms were shown using broadbeam heavy-ion experiments, and were corroborated using position-aware TPA laser testing as well as dynamic heavy-ion simulation using Synopsys TCAD. TPA results show a position dependence of laser excitations, where pulse that occur farther from the junction take a larger number of excitations to upset the cell. Simulations showed the importance of dynamic modeling with resistive elements, by showing the over-prediction given using constant-resistance models. These results set the foundation for future RRAM reliability work for space and radiation environments, giving researchers and designers an understanding of what to expect from resistive memories during ground testing for space qualification. The dynamic compact model also give designers a methodology for RRAM simulation with the goal of minimizing implementation costs associated with a new technology.

CHAPTER 5

RRAM Simulations for Highly-Scaled Access Transistors

Estimating the response of the next-generation of resistive memories is a useful extension of the presented experimental data. Using a 28 nm FinFET access transistor and modifying the resistive element's properties to operate with the resultant decreased conduction current, the SER of future RRAM cells can be estimated.

5.0.1 Scaled Access Transistor and Resistive Element Model

The FinFET transistor has a gate length of 28 nm, and fin width of 20 nm. All 8 fins are constructed on top of a 150 nm thick SiO_2 buried layer. The gate oxide is 3 nm thick, and wraps around the top and two sides of each fin. Ideal contacts are placed on the entirety of the gate oxide opposite the silicon channel. A substrate contact is placed 140 nm from the nearest fin, and is grounded for all simulations. The cell was designed to match information found in [70], and the resulting structure and doping profiles are shown in Figure 5.1.

The resistive element's properties were scaled to accommodate the lower on-state current of the FD-SOI (Fully Depleted Silicon On Insulator) access transistor. To ensure the resistor's parameters stayed within physical limits, each modifiable parameter was changed to improve the element's switching speed. This is a safer approach than modifying one parameter heavily, because changing a single parameter would likely move it into an unphysical range. The new parameters are given in Table 5.1.

The parameters of the FinFET's resistive element were verified by passing a 5 ns 1 V square-wave pulse to the gate of the access transistor and analyzing the resulting resistance. Figure 5.2a shows the resulting voltage across the resistive element when the gate pulse is applied. The voltage drops as the RRAM's resistance reduces because the access transistor has a limited ability to conduct the necessary current. The voltage spikes at the beginning and end of the write pulse are caused by switching noise. Figure 5.2a also reinforces

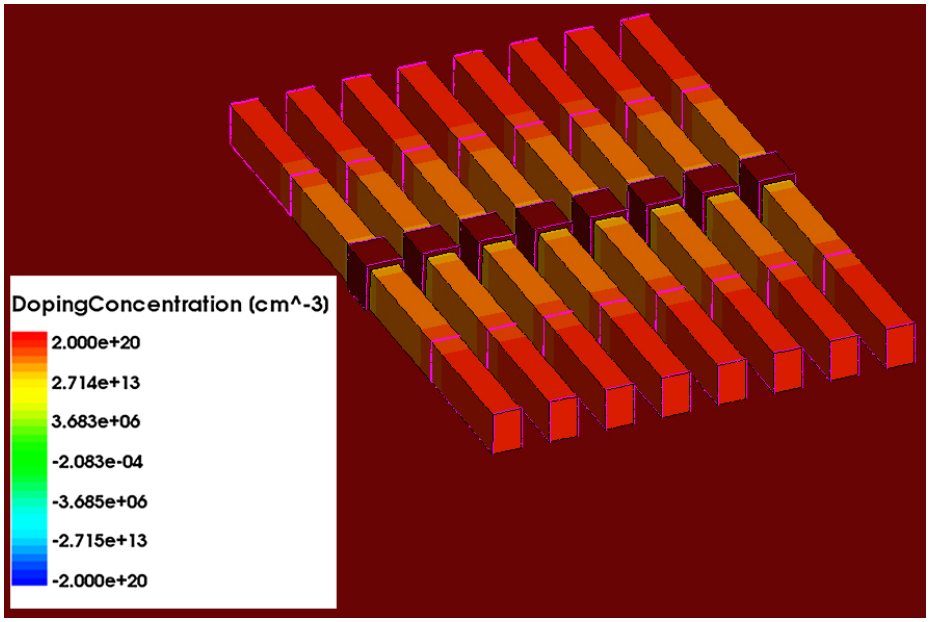

Figure 5.1: Angled topside image of 3D TCAD FinFET structure used for simulations to understand the effects of access transistor scaling.

why dynamic modeling is important to properly characterize resistive memories, because with a static resistor the applied voltage would be constant throughout the simulation. The constant voltage would over predict the ability of the access transistor to switch the resistor's state, leading to inaccurate modeling. Figure 5.2b shows the resulting resistance from simulation, with the final resistance being just below the low resistance threshold.

5.0.2 Estimating On-Orbit Upset Rates

The sensitivity of the above cell can be estimated using heavy-ion simulations in Synopsys TCAD. To maximize the feasibility of the heavy-ion solution space, incident angles of the simulated strikes were limited to every 45° angle with redundant strikes (mirror image angles) excluded. The exact angles are listed in Table 5.2. The strike origin is in the middle of the eight fins in both the X and Y directions. The angle (0,0) is perpendicular to the surface and passes through the origin.

To further limit the sample space, the worst case angle is used as the incidence for which

Table 5.1: Variable Declarations

Variable	Description	Value
A	Pre-exponential Constant	± 1 [66]
ϕ	Filament Width	Data [66]
E_a	Activation Energy	0.4
α	Barrier Lowering Coeff.	0.3
V	Applied Voltage	Input
t	Pulse duration	Input
$R(n)$	Present Resistance	$R_0 - \Delta R(n-1)$
R_0	Initial Resistance	Input
R_{th}/R_0	Thermal Resistance Ratio	3000
T_0	Starting Temperature	300

Table 5.2: Simulated Strike angles in spherical coordinates.

θ	ϕ
0°	0°
0°	45°
0°	90°
45°	0°
45°	45°
45°	90°
90°	90°

every strike occurs. This is an overly conservative estimate of the cell's sensitivity, but makes the upset rate calculation easier to comprehend, while still stressing the robustness of this cell. The worst case angle for all ion LET values is a particle traveling through the channel of all of the fins (0,90°). A worst case strike at the highest LET (100 MeV-cm^2/mg) is not enough to upset the cell. The cell would still have to be struck three times, without the cell being SET/RESET during normal operation. At this point in the calculation it is already apparent that the cell will be very difficult to upset, but the finalization of this calculation shows the magnitude of the cell's sensitivity, and can give insight into what part of the heavy-ion spectrum plays the most significant role.

Figure 5.3 shows the results from the worst case strike at each LET value in red. The same exponential trend that was shown in experimental data is shown in simulation as the LET values approach 0.1. Values below 0.1 cannot cause any measurable change in simu-

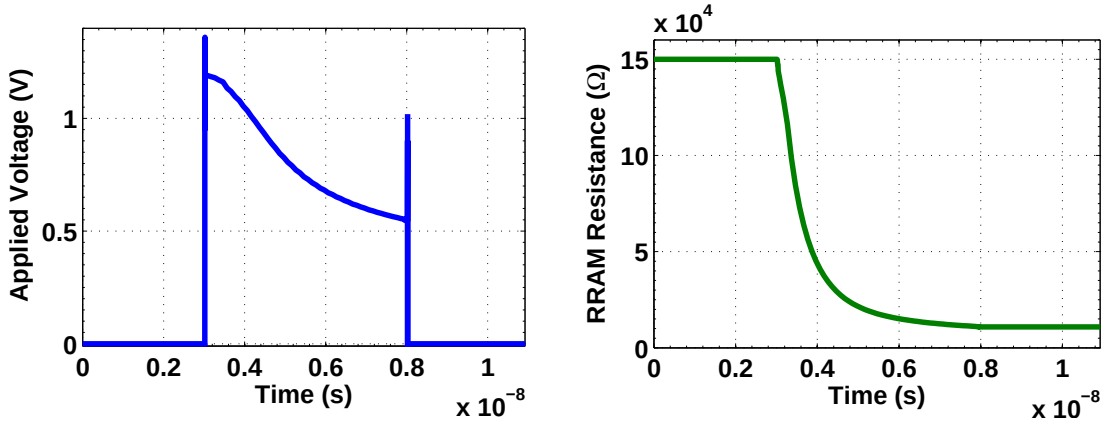

(a) (b)

Figure 5.2: (a) Voltage differential applied across the resistance element by activating the access transistor and (b) the corresponding change in the resistive element's resistance from 3D TCAD simulations.

lation, so they are seen as requiring an infinite number of strikes to upset. Ions with LET values less than this threshold will not cause SEUs in this cell. The required number of strikes until upset can be used to weight a particular on-orbit particle spectrum to estimate the upset rate of this technology. The blue data in Figure 5.3 represent the best case strike angle (normal incidence). The normal incidence data show that even at high LET values, the best case does not match the worst case. The best case data demonstrates the conservative estimate of the following calculation.

Figure 5.4 shows data generated from Creme96, a solar spectrum generation tool, for the worst day of geosynchronous orbit [24]. The calculation is performed with 100 mils of aluminum shielding. Sharp peaks in this data are an artifact of the calculation process. This spectrum, like many extraterrestrial environments, is dominated by particles with an LET less than 5 MeV-cm^2/mg. To weight this spectrum in coordination with the TCAD simulation data, the spectrum needs to be divided by the number of strikes it would require to upset the cell. The spectrum also needs to be weighted by the vulnerability window

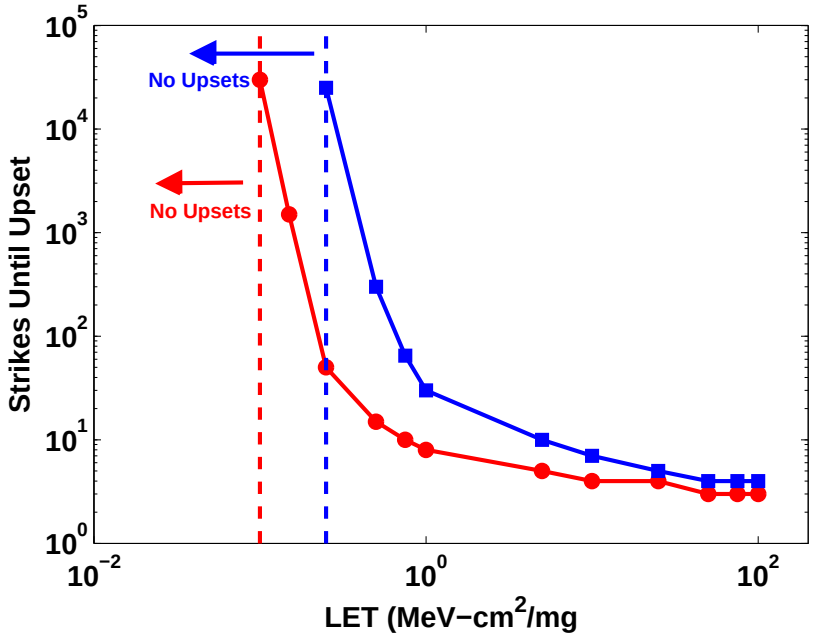

Figure 5.3: Number of ion strikes required to upset the cell, at the worst case angle (through the channel of all fins) shown in red, and the best case angle (normal incidence) shown in blue.

($5{\cdot}10^{-3}$) discussed in Section 4.5. This is represented mathematically as:

$$Flux_{weighted}(LET) = Flux(LET) \cdot \frac{Window\,of\,Vulnerability}{Strikes\,Until\,Upset(LET)} \tag{5.1}$$

Significant differences can already be seen between the two spectra shown in Figure 5.5. The difference is several orders of magnitude across the LET range, and the weighted spectrum ends at an LET of 0.1 MeV-cm^2/mg. The end of the spectrum is a significant contributor to the reduced single event upset rate because of the dominance of lower values in the spectrum. Resistive memories, like their CMOS memory counterparts, have a threshold for upset or state change, with the exact value varying between different technologies.

The desired result is an estimated upset rate per bit-s. To remove the angle of incidence dependence, the worst case angle is assumed for all strikes; to account for all possible incident angles, a factor of 4π is multiplied by the spectrum. The flux is also normalized

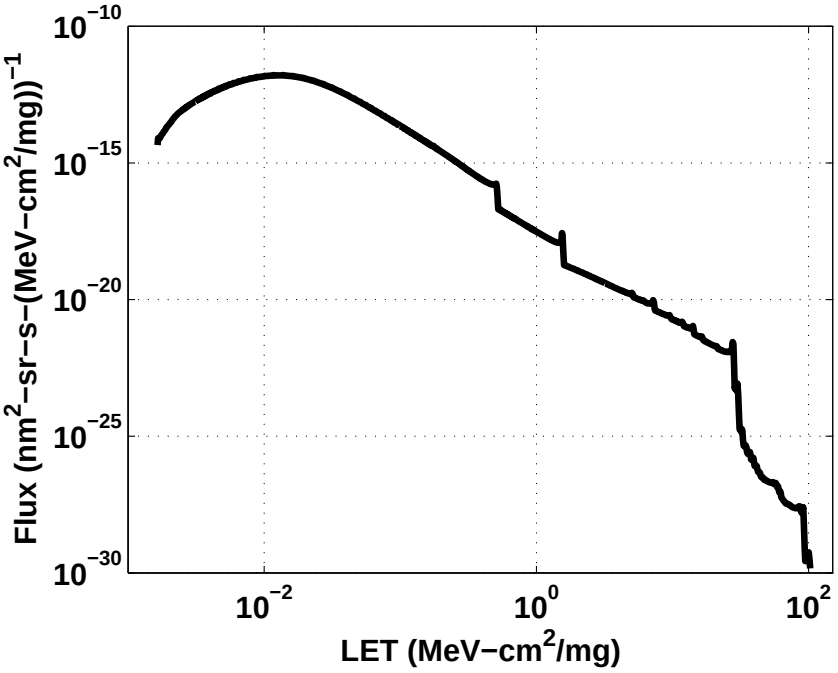

Figure 5.4: Creme96 generated spectrum for worst day of geosynchronous orbit.

by the bit area (300 nm x 430 nm) to obtain results on a per bit basis. The spectrum is then reverse integrated in (5.2) to estimate the total upset rate for the cell in this environment.

$$Integral\,Upsets = \sum_{l=100}^{LET} Flux(l) \cdot \frac{Window\,of\,Vulnerability}{Strikes\,Until\,Upset(l)} \cdot 4\pi \cdot Bit\,Area \tag{5.2}$$

A plot of the integral upsets per bit is given in Figure 5.6. Expected features show up in the data for LET values less than 0.01, where the integral saturates, and there is no more contribution to the sum. A strong contribution is also shown from lower LET particles. Because of their high probability in the original spectrum, even the much lower state change of the resistive element caused by these particles cannot eliminate their dominance.

The maximum value in Figure 5.6 can be used to estimate the number of upsets in a large data array, as well as understand the likelihood that an event occurs in a single cell. A limit-defining example is given for a memory array that is 1 Gb in size, and will be storing data permanently. No additional (excluding initial programming) data writes will

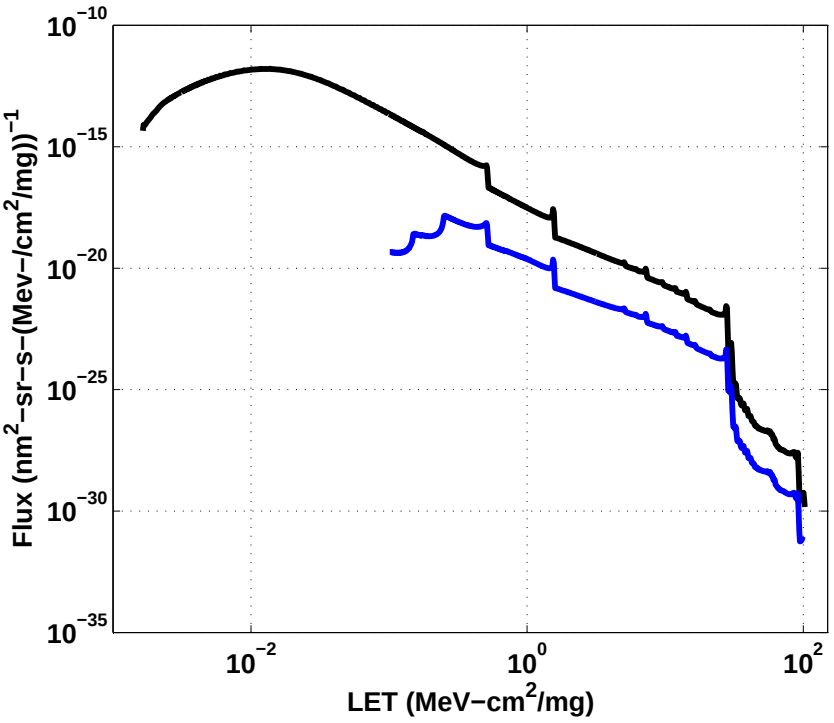

Figure 5.5: Creme96 generated spectrum for worst day of geosynchronous orbit (black), and the weighted spectrum of flux taking into consideration Equation 5.1

be performed on the cell of interest during its lifetime. Any degradation to the bit will be kept indefinitely until the cell upsets. This example is given as the extreme use case, since it is highly improbable during operation that adjacent cells would be written to, while this cell would remain static. Starting with the maximum value from Figure 5.6 ($3.35{\cdot}10^{-15}$ (bit-s)$^{-1}$), and multiplying by the number of bits yields the number of upsets per second in the memory array.

$$Integral\,Upsets = 3.35 \cdot 10^{-15} \cdot 1 \cdot 10^{9} = 3.35 \cdot 10^{-6}\ (bit-s)^{-1} \tag{5.3}$$

This equates to approximatively 1 upset in 1 Gb every 3.5 days, a quantity that can easily be corrected with basic Error-correcting codes (ECC). ECC is almost always used in some form in critical applications implemented in radiation environments, and is also widely

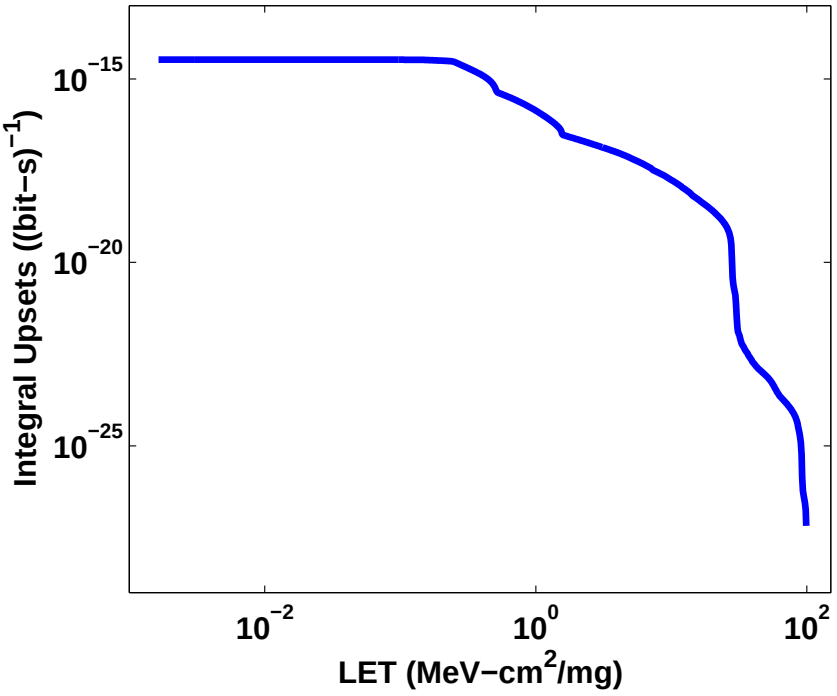

Figure 5.6: Integral upsets per bit-s after all calculations have been performed on the original Creme96 spectrum and has been normalized to the bit area.

used in server/data-center memory. MEU errors can further be eliminated by regularly rewriting to the cell. Since RRAM has shown read/write cycles in the 10 billion range, regular rewriting is not a reliability concern, but could almost eliminate MEUs, and thus upsets in the device.

5.1 Discussion of Future RRAM Technologies in Radiation Environments

Projecting future technologies is fraught with assumptions and challenges to foresee issues not yet discovered. The goal of this section was not to precisely predict how an RRAM will respond as it scales, but to understand how the mechanisms will affect the RRAM memory cell as both the resistive element and access transistor evolve. The SOI FinFET reduces the voltage transient generated on the cell, while maintaining sufficient drive strength. Since there are no other transistors in the storage element that are scal-

ing downward with the access transistor, the cell's SEU response will improve because the single-event pulses are shrinking while the pulse needed to transition the cell remains constant. Even when the resistive element is made to operate faster, reducing the voltage pulse needed to upset the cell, the single-event pulse scales faster than the response of the element. Again, there are assumptions that could be incorrect depending on the driving factors of next-generation RRAMs, but this section shows that the outlook is positive. Using on-orbit calculated spectrum shows that SEUs will likely be impossible, and MEUs will be the only chance for an upset. Writing on a regular basis to all cells in the array can mitigate most MEUs because the degradation to individual cells cannot be maintained. Combined with ECC, hardening cells may not be a strong concern because of inherent robustness in radiation environments.

CHAPTER 6

Discussion and Conclusions

This chapter serves to summarize the results of this work, explain some of the limitations, and detail future actions which may lead to further insight. A major result from this work is the first experimental evidence of single-event upsets in Hf/HfO_2 based Resistive Random Access Memories (RRAMs). The cell was also found to only be susceptible in only one of the two states it occupies during normal operation (High Resistance State). The RRAM's sensitivity shows that SEUs will be a concern for these memories if they are used in space and other radiation environments. Also, the single-state sensitivity demonstrates a 50 percent reliability increase, compared to similar unhardened memories, before any hardening of the RRAM has taken place. Even large values of laser excitations were not able to transition the cell, solidifying this mechanism's existence. Since it was also seen in simulations, there are no currently known limitations to this finding, with future work likely examining different materials or layouts where this mechanism may cease to exist.

A new type of upset was also seen, whereby effects from subsequent strikes on a single cell can accumulate until the cell transitions to its complementary state. This upset is termed a Multiple Event Upset (MEU), as an extension of single-event upsets. MEUs are possible because the RRAM lacks a restoration force seen in other memory types (e.g., SRAMs). An MEU in these cells should be considered a rare event, almost always occurring during long periods of individual cell inactivity, when an adjacent cell is activated. The cell's window of susceptibility stems from the RRAM only being susceptible when a voltage in excess of 0.7 V is applied to the BL of the device. During heavy-ion testing and in heavy-ion simulations, MEU are the major contributor to upsets in these cells. RRAMs can be operated in such a way that cells are rewritten if inactive during long periods of time. Therefore, a simple firmware level condition would drastically cut the SER in the cell, and

in some future generation of RRAM, when combined with ECC, may even eliminate upsets altogether. There is also a real likelihood that the RRAM becomes more sensitive as the access transistors scale to smaller dimensions, possibly offsetting gains made by these techniques. The main limitation of this result is experimentally dependent definition of MEU, something that is unavoidable when testing individual RRAM cells. There is a future need of testing dense memory arrays to understand how these MEUs will appear in arrays while they are being operated.

The exponential dependence between the sensitivity of the cell to ionizing radiation and the applied voltage to the BL of the device was shown in both heavy-ion and TPA experiments. The RRAM becomes more sensitive with larger applied bias voltages on the BL of the device, which is inverse to similar mechanisms in SRAM cells where higher operating voltages decrease a cell's sensitivity. The inverse dependence is a crucial result for future experiments and circuit design guidelines. Since the result is counterintuitive from standard CMOS SRAM hardening, there should be a goal to limit voltage magnitudes so that upsets rates can be minimized. The application of this information will be limited by the circuit's ability to function at lower supply voltages. Future insight will likely be gained from data arrays due to the limiting statistical nature of a single cell. Some insight could be gained from trying to find the minimum reliable operating point of the RRAM cells, and comparing that to the nominal supply voltage while under TPA or heavy-ion irradiations.

A compact model was created to help understand experimental results on the RRAM, and is a promising area of future work. The dynamic compact model was experimentally calibrated to match the switching response of RRAM. Results comparing the use of a single resistor and the created compact model show the importance of having a dynamic resistor in simulation. Results obtained using the static resistor method over predict the change in the resistor's state because the resistor does not decrease in magnitude during simulation. The dynamic model was used to investigate how the fabricated cells would respond to position dependence of the incidence ion, and it qualitatively matched results from position-

aware TPA testing. The model also allowed for simulation of a hardening technique that greatly increased the hardness of the cell (likely meeting flight requirements) while still maintaining the cell size of a standard SRAM cell. Finally a dynamic resistor model was implemented with a scaled access transistor and resistive element to estimate the sensitivity of future technology nodes. The results were promising, showing a decrease in sensitivity with increased scaling. The model presented in this work is deterministic, with the goal of matching the average response of the RRAM cell. Future modeling should concentrate on encompassing the stochastic operation of the RRAM in a probabilistic way. This would be an intensive modeling project, with many unknowns yet to be realized.

To understand how tightly spaced RRAM cells will interact in large arrays, experiments and simulation were preformed on a custom silicon test structure. The investigation of how neighboring junctions affect each other from basic physical mechanisms showed clear evidence that adjacent junctions alter the charge collected on opposing junctions. Turning on a nearby junction reduces the amount of charge collected on the main junction. This is counter intuitive to the term charge sharing, because the junctions are competing for the same generated charge. The closer junction or the junction with the stronger reverse bias will collect more of the generated charge, and was shown experimentally using TPA laser testing. This mechanism will become increasingly difficult to study as junction sizes and spacing become much smaller than the generation size of the TPA laser. These junctions will also be much smaller than the window of uncertainty during microbeam heavy-ion experiments, making position-aware measurements as efficient as broadbeam irradiations. Measurements will have to move to on-chip calculations with an array of measurement circuits producing statistics. A pulse width measurement circuit may be sufficient to detail charge collection mechanisms in a statistically valid method, and can be used in broadbeam irradiations. This limits future work to statistical representations of the mechanisms and not raw transient capture and processing that was used in this work.

Perhaps the most significant outcome from the Multi-Node Charge Collection (MNCC)

research was a detailed comparison of heavy-ion irradiations and TPA laser experiments. A significant increase in the likelihood that a MNCC event occurs was shown when TPA laser experiments were run to correlate with heavy-ion data. TCAD simulations were compared in the same way and showed a quantitatively similar response to heavy-ion irradiations. The difference between excitation sources as it pertains to MNCC has a resounding effect on the interpretation of data that is collected using only TPA laser experiments. As covered in Section 2.2, Radiation Hardened By Design (RHBD) circuits are often validated using TPA laser experiments exclusively. TPA validation alone could misrepresent the efficacy of a particular hardening strategy by increasing the likelihood and magnitude of MNCC in the circuit. Likewise, when the hardened circuit is compared to an unhardened version, the unhardened version may show results which are worse than heavy-ion data if the circuit has a particular sensitivity to MNCC. The method described in this work gives future experimental guidance to understanding the difference between TPA laser and heavy-ion irradiations. It is even possible to layout test structures to quantify the difference in an attempt to directly compare the two sources. A particular technology could be compared between the two sources and then used as a calibration point for multiple circuits to be tested using only TPA excitations. A calibration structure is the best future application of this work, and is where the work should head to have a meaningful impact on the way experimental data is understood.

All of these achievements were used to test the efficacy of a single transistor hardening technique and a projection of how these mechanisms change with scale. MNCC was the only way for the hardened cell to change the state of the resistor, but still required 9 or more worst case events in a row to upset the cell. If only one transistor collects charge, the state of the resistor is not modified. Scaling the access transistor further reduced the effect that ionizing radiation had on the cell's reliability, reducing the need for hardening. Work will have to continue on this topic as devices with next-generation layouts become available, but these results give RRAM a promising future in radiation-tolerant designs. The cell's

current reliability should lead the mission critical electronics community to look at these memories.

Appendices

Appendix A

Rapid Transient Acquisition and Computational Analysis (RATACA)

A.1 DISCLAIMER

Use at your own risk! Be familiar with the code before you attempt to publish any data that it produces. Do not blame the code for your lack of effort in learning how this code base processes transient data. If, after reading this manual, you have questions about how to use the software, or what calculations it is performing, please ask for help. Also, any publications using this code base should be reviewed by the current Vanderbilt maintainers, before being sent for outside review.

-Geoff and Nick

A.2 Introduction

This code base was written to help facilitate single-event testing on devices using the two-photon absorption laser source at Vanderbilt University, and particle testing around the world. It is broken into three main subsections: data capture, data analysis, and data plotting. Data capture contains scripts needed to capture data using a Tektronix oscilloscope over TCPIP or GPIB, and control code for the motorized stages in Vanderbilt's laser SEE test facility. It is not recommended to use the laser code detailed here for other testing facilities, as it may be completely incompatible. Data capture for ion sources is also documented, but should be more universal in its application. Data Analysis code processes captured data and does the following: produces plots of transient information in real-time (peak current, total charge, transient FWHM), filters data based on user-specified input parameters to reduce the effects of noise on transient signals, intelligently chooses integration bounds of transients for determining total collected charge, and saves a single output file containing all processed and original data for each individual measurement run (e.g, all of the data for a particular laser scan is condensed into one output file).

A.2.1 Some General Comments Regarding RATACA and MATLAB

All data capture, analysis, and plotting utilizes MATLAB software. As an end user, you should focus on the subsections of the code pertaining to data analysis and plotting. If you do not already have access to the code base, please contact the current RER staff member responsible for maintaining the code base, and request the RATACA code. You will be given access to a folder containing many of the functions described below.

It is essential to understand the following MATLAB concepts in order to use this software to its fullest potential: Basic array manipulation, Basic data plotting, Cell Arrays, and Structures. These concepts will not be discussed here. If you are not comfortable with these terms, Google is your friend. The rest of this guide will focus on using the RATACA software, and will assume the user is comfortable with the MATLAB concepts mentioned

above.

To run these functions, make sure they are on your MATLAB path, or that you have navigated to the folder where they are saved on your machine (using the current folder bar at the top of the MATLAB window). You can temporarily add folders to your MATLAB path by right-clicking on them in the Current Folder pane (left side of the MATLAB window) and choosing Add to Path. This will only be in effect for your current MATLAB session, to permanently add folders to your path, use the $File > SetPath...$ option.

A.3 Data Capture

A.3.1 Common Operations

A.3.1.1 Setup Oscilloscope

Required Software: TekVISA 4.0 or greater, and Agilent I/O 16.3 or greater.

It is recommended that TCPIP on a Ethernet based LAN be used for connecting to the oscilloscope. A GPIB function is available, but should only be used in the event that the TCPIP approach is unusable. To connect the scope, make sure the scope is found by Agilent I/O software. If using the laser gui, go on to the next paragraph. If collecting heavy ion data, you will need to create a scope instance to make measurements, i.e. $scope = connect\_to\_12G\_scope\_tcpip()$;. A windows will pop-up to input the scope's IP address; it can be obtained from the Agilent I/O software (e.g. $TCPIP0 :: 169.254.178.72 :: inst0 :: INSTR$).

Next, settings on the oscilloscope need to be set according to the measurement need. Set the oscilloscope to Fast Frame mode, and select the number of Fast Frames needed for capture. Each requested read will capture this number of transients per read. Next choose an appropriate record length, and make sure it matches the record_length value in $xyz\_raster\_monitor\_rev2\_gui.m$. Leave on only the channels needed for data capture, and make sure to not skip sequential channels (i.e. 1,2,3 but not 1,3,4).

A.3.2 Laser Control GUI

A.3.2.1 Setup A Scan

Function Call: *virtual_joystick_with_scanning*();

This launches the interactive GUI from which all systems can be connected to and controlled, Figure A.1. Motion controllers for the XY and Z stages should connect auto-

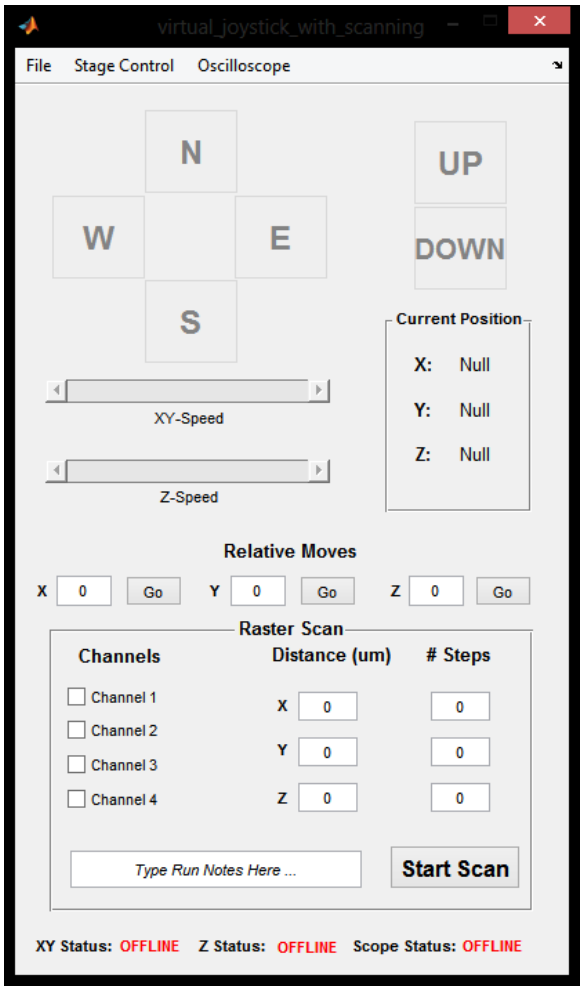

Figure A.1: Laser system interactive GUI.

matically when the GUI is initialized. Error messages will prompt the user if a connection cannot be made. Usually, an error results from the GPIB connection to the Newport Z-stage controller. A simple fix for this is power cycling the GPIB/LAN gateway, letting it re-acquire an IP address, and then retrying the connection. Typically, connection errors will

need to be fixed by whoever is responsible for maintaining the setup. Finally click the oscilloscope menu on the GUI and select connect. If an error occurs, most likely the scope is not visible in the TekVISA software, the Agilient I/O software, or the IP address entered into the software was incorrect. It is also recommended that the motors of the stages be tuned each time the GUI is opened. **This should be done by the current laser operator ONLY**, and is an automated process under the *Stage Control* option named *Tune XY Motors*.

A.3.2.2 Run A Scan

Due to a MATLAB limitation the right click mouse button must be used to control the GUI. The N,E,S,W buttons move the stages in the given direction. Up and Down move the stage only in Z. Stage motor speeds are controlled using the sliders below these buttons. To move an exact quantity, use the "Relative Moves" subsection. Units are in micrometers, and can be positive or negative, depending on the desired direction of motion.

If using the oscilloscope, select the channels you want to record, and verify that they are enabled on the scope. Now, input the distance you want to raster over, and the number of steps you want to take in that direction. The minimum step is 0.1 μm, and make sure you choose a step size that is a finite length decimal number (i.e. not 0.33333 repeating). For example, if you wanted to move 15 μm in the positive x-direction, and you wanted the step size to be 3 μm, you would set the X distance to 15 and the first #*steps* value to 5 (i.e., move 15 micrometers in 5 steps, for a step size of 3 micrometers).

At the bottom of the Raster Scan panel, there are two text fields. The first is intended for run number and/or run name. A good idea here is to enter something descriptive about your current measurement. For example, "Run_1_Device_A_Vg=0V_Vd=1V_Vs=0V_area_scan", or something similar. The individual files produced during the scanning operation will take whatever text is entered in this field and use it as the prefix of the filenames for the output files. The second text field is intended for notes about the run you are about to perform. This would be a good place to describe the intent of the measurement, or any other notes

you might typically record in a lab notebook, etc. The text entered into this field will be saved within each individual file produced during the scan, which is good for reference later.

Once the proper scan parameters have been chosen, click the *LaunchScan* button. This will open a window prompting the for the save location for the data that is about to be collected. It is recommended that data be saved in one main folder, with individual subfolders corresponding to each run. For example, the main folder might be called *Data*. Within *Data* would be individual folders named *Run*1, *Run*2, *Run*3, and so on for each scan performed. After the proper save location is chosen, another window will open displaying a text field and three buttons. Clicking *Go* will start the scan. During the scan, progress will be shown in the text field. DO NOT interact with the main GUI window during the scan. Doing so could lead to errors. However, if you wish to temporarily pause a scan (if the laser energy requires tuning, for example) click the *Pause* button. Double-clicking *Resume* will restart the scan at the position where it was paused. If you wish to cancel the run entirely, click *Cancel*.

Once a scan completes, the start button will turn gray and read finished. The stage should then return to its original location. The same procedure that is outlined above can be used to set up and initiate another scan.

A.3.2.3 Other Options

In addition to the buttons and text fields previously described, the Laser Scan GUI also features several menus. These are the File menu, the Stage Control menu, and the Oscilloscope menu. Currently, only the functions found in the latter two menus have been implemented. The Oscilloscope menu allows the user to connect via TCPIP to the TDS6124C oscilloscope. The functions available under the Stage Control menu are described in Table A.3.2.3.

Function	Action
Lock XY	Freeze the X and Y stages in their current position
Free XY	Allow the X and Y stages to be moved freely by hand
Set Current as Home	Set the current position (X, Y, and Z) in memory as the Home position
Move to Current Home	Automatically move the X, Y, and Z stages to the Home position
Tune XY Motors	Automatic tuning function for the X and Y stages

Table A.1: Functions available in the Stage Control menu of the Laser Scan GUI and their intended purpose.

A.3.3 Ion Transient Capture

There is currently not a GUI for transient capture for ion data, so all data capture will be handled by the MATLAB command window. Data capture is performed by:

$function\ \ ion\_ff\_acq\_rev3(scope, num\_reads, channel\_list, varargin)$

Input Arguments:

Variable Name	Type	Comments
scope	instance	Oscilloscope instance created in the previous subsection
num_reads	int	Number of times to read data from the scope
channel_list	array	Number of channels to record, e.g. [1 2 3]
varargin arguments:		
ion	string	Ion Under Test.
cocktail	string	Cocktail Under Test
notes	string	User notes
saves	string	'yes' or 'no', default 'yes'
out_dir	string	Location for data, default is user receives GUI prompt

Table A.2: Ion code input parameters.

EXAMPLE: Ion Transient Capture

This call will make 100 reads from the oscilloscope, which will have 20 Transients (fast frames) per read, and data will be recorded for channels 1 and 2:

$ion\_ff\_acq\_rev3(scope, 100, [1,2], 'ion', 'oxygen', 'cocktail', '16MeV', 'notes', ...$

$'Run\ 1\ 3.3V\ Device\ 2345W'$)

Next, a window will appear to let the user choose a save locations for the data, then the capture will begin. The command line output will let you know which channels are being captured, and how many total transients were recorded. The total number of data points should be the record length times the number of fast frames.

A.4 Data Analysis

A.4.1 Raw Data

A.4.1.1 Laser Raw Data

The laser scan GUI outputs a .mat file per location per channel for the entire scan in the user-specified folder (one folder per scan). This data can be accessed directly using the variables in Table A.3. The data is more manageable when processed using the method detailed in the next subsection.

A.4.1.2 Ion Raw Data

The ion code outputs a .mat file per read per channel for the entire run in the user-specified folder (one folder per run). This data can be accessed directly using the variables in Table A.4. The data is more manageable when processed using the method detailed in the next subsection.

Variable Name	Type	Comments
time	matrix	The recorded time for all data points at the given location
volts	matrix	The recorded voltage (mV) for all data at the given location
num_fast_frames	int	Number of captured Fast Frames in the data file
channel	int	Source channel
time_per_point	int	Time between data points
start_time	double	Time of first data point
y_multiplier	double	Scaling factor for Y data
record_length	int	Number of data points per transient
xlength	int	Distance scanned in X
ylength	int	Distance scanned in Y
zlength	int	Distance scanned in Z
xstep	int	Distance per step in X
ystep	int	Distance per step in Y
zstep	int	Distance per step in Z
matrix_size	array	Number of record locations in [X,Y,Z]
mat_coords	array	Current location in the scan matrix [X,Y,Z]

Table A.3: Raw laser data structure.

A.4.2 Automated Data Processing

Raw data is processed using the following:

Laser

$monitor\_folder\_laser(data\_store, varargin)$

Ion

$monitor\_folder(data\_store, varargin)$

data_store is the directory where the raw data is located, and *varagin* is a variable used by MATLAB to pass parameters. This can be called with no additional argument as in: $monitor\_folder('PathToFile')$; , but does has 3 optional arguments.

'trans','no' will disable transient plotting.

'backups','yes', will backup raw data to a separate location(useful for ion testing).

'params','FileName.txt', will allow for custom filtering etc., which is detailed in the next section.

Variable Name	Type	Comments
time	matrix	The recorded time for all data points at the given location
volts	matrix	The recorded voltage (mV) for all data at the given location
num_fast_frames	int	Number of captured Fast Frames in the data file
channel	int	Source channel
time_per_point	int	Time between data points
start_time	double	Time of first data point
y_multiplier	double	Scaling factor for Y data
record_length	int	Number of data points per transient

Table A.4: Raw ion data structure.

This function creates a single output file that contains both the raw data, and processed data (filtered transients, peak current, collected charge, etc.). Specifically what data is in the output file can be found in Table A.4.2.6 for laser data and Table A.4.2.7 for ion data. Figure A.2 shows the basic plot output of the processing script. The raw transient data is shown in blue for all four channels, while the median filter transient (only used for data processing) is shown in red (dashed). The FWHM is shown in magenta, and the integration bounds are shown by

---

EXAMPLE: monitor_folder_laser This call will process laser data without plotting, but with backups, and with a different parameter file:

$monitor\_folder\_laser('DataDir','trans','no','backups','yes','params',...$
$'my\_custom\_params.txt')$

A.4.2.1 Custom Parameter File

A parameter file is loaded by *monitor_folder* when data processing begins. It contains several useful values such as the output directory for processed data, a directory to backup a copy of the data (if backups are requested when using *monitor_folder*, filter coefficients

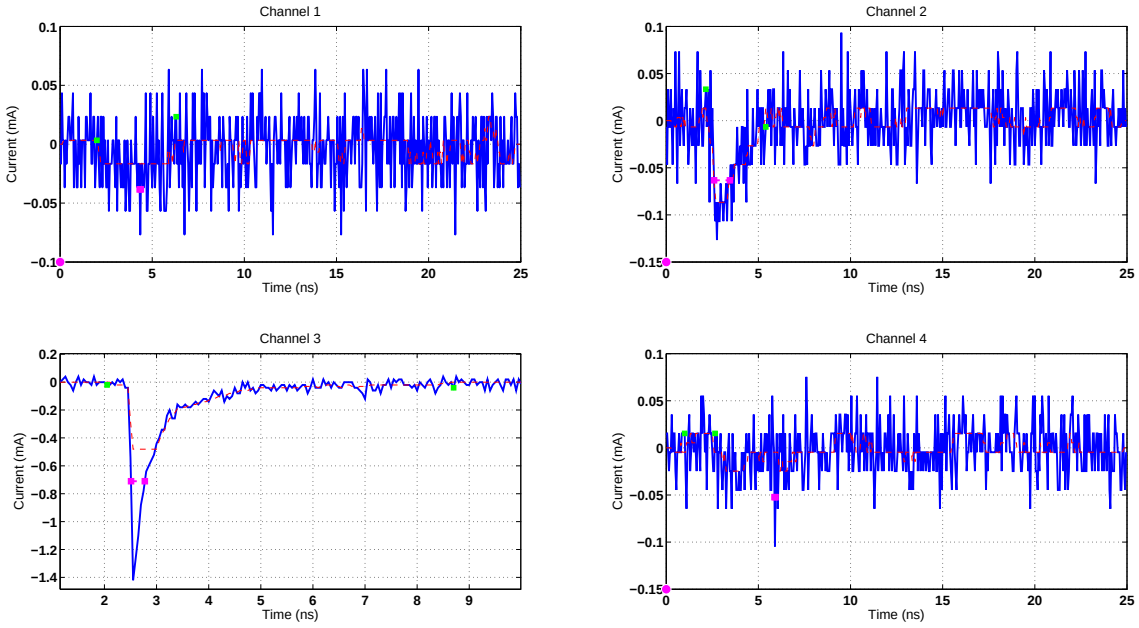

Figure A.2: Full plot of all four channels being plotted during processing.

for transient filtering, and the type of plots shown to the user after processing. Filter coefficients often change based on the device and environment, so it may be useful to change the filter values in order to obtain better noise canceling results. Also, it is a good idea to specify a path to an output folder for processed data. Custom files should be located in the same directory as the default file $.\backslash monitor\_parameter\_files\backslash$. Ensure that your parameter file structure matches that of the default. The default file appears as:

Example: default_parameters.txt

%User parameter folder for monitor_folder.mat

%directory to save processed data files to

output_directory=default

%directory to save backups to (for remote backup). Use 'none' for no backups

backup_directory=default

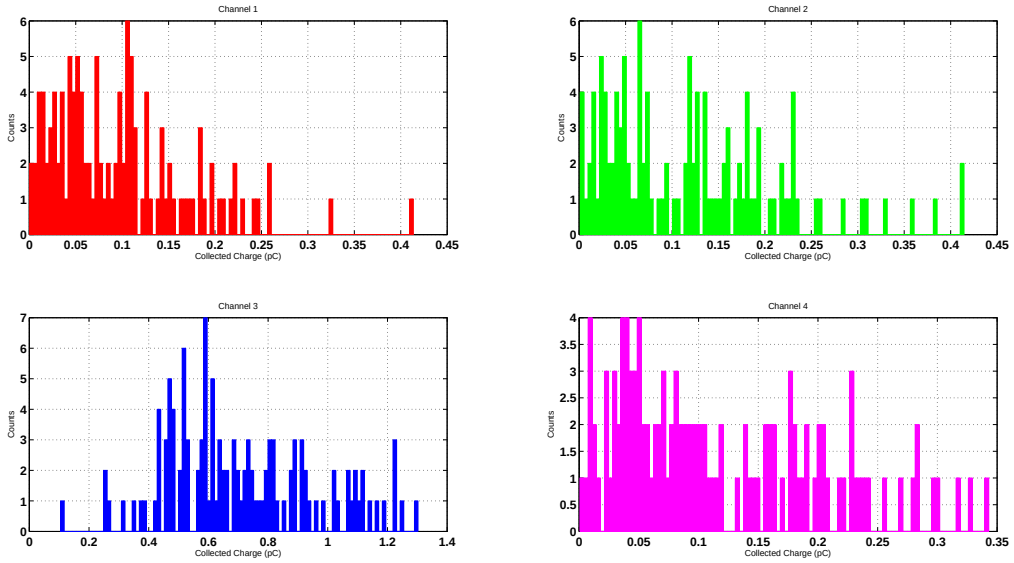

Figure A.3: Histogram of raw data being plotted during data processing, but in real time with data capture.

%filter coefficients. filter coefficients go as: [X,Y]=cheby2(A,B,C)

A=4

B=30

C=0.5

%Plot type. Default is 'peak_charge'. Change if you have your own specialized plot function plot_type=peak_charge

---

A.4.2.2 Filtering

Filtering parameters are often temperamental, and depend heavily on the data being recorded. RATACA uses MATLAB's built in Chebyshev Type II filter which is called using the $cheby2(n,R,Wst)$; command. The three input parameters are detailed in the MATLAB

help documentation. In its current state, RATACA does not allow for a different filter type, however the filter coefficients can be edited through the parameter files described earlier. Issue a *doc cheby*2 at the matlab command line to get a better understanding of the filter coefficients.

A.4.2.3 Selective Integration

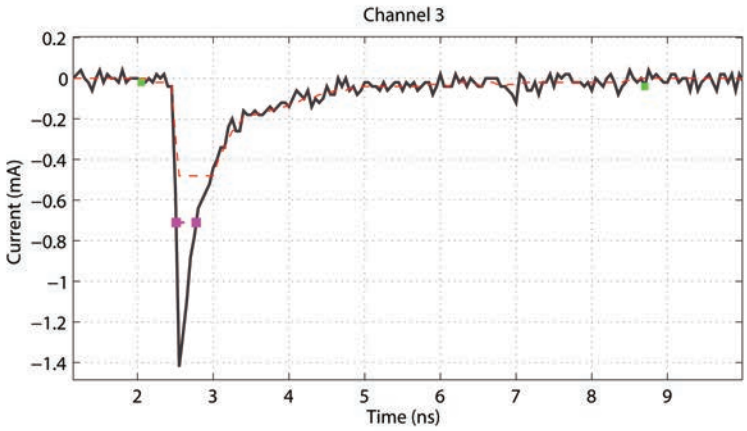

Figure A.4: Data being plotted in real time during transient data processing.

Many transients in modern devices are at, or approaching, the noise floor of the test environment. This often makes it difficult to calculate the total collected charge from a given measurement. Many oscilloscopes have drift in the noise that does not integrate to zero, and can strongly affect the analysis. To alleviate this, RATACA uses the median filtered transient (Figure A.4, red dashed line) to determine the bounds in time (Figure A.4, green squares) of integration, then only integrates the original data over that time period. Traveling away from the peak value in positive time, the time at which a value that is 1 % of the maximum is chosen as the end time. The same value is chosen heading towards negative time, and then the raw data is integrated over these bounds. Transient captures which exceed the window of the scope will result in incorrect data.

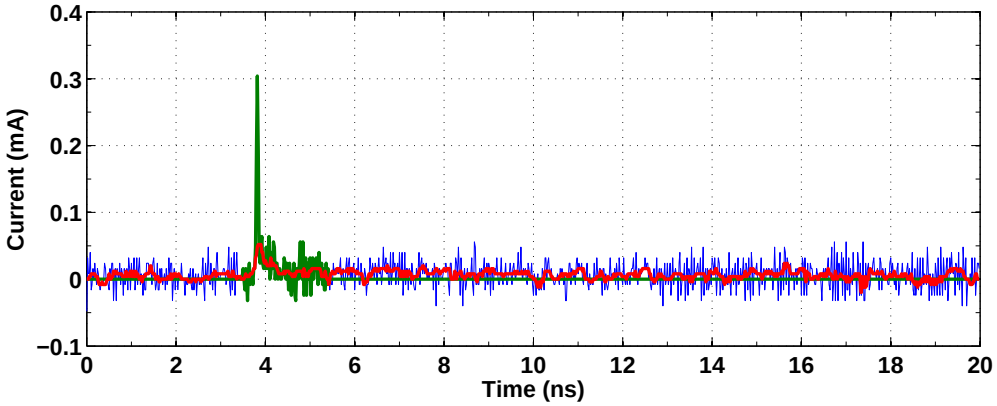

(a) Raw transient data shown in blue, median filtered transient data shown in red, and the section of transient data used to integrate collected charge values shown in green when using the selective integration procedure.

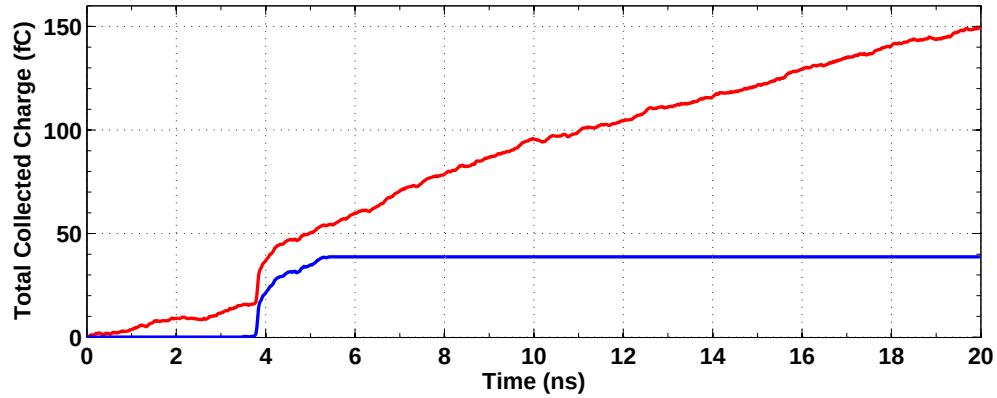

(b) The result of integrating the raw transient data from (a) without any processing is shown in red, while the result of using the selective integration procedure is shown in blue.

Figure A.5

A.4.2.4 Processed Data

A.4.2.5 Optimized Laser Data

$function\ in\_data = optimize\_laser\_data(data\_file, photo\_diode\_channel)$

There is inherent fluctuation in laser pulse energy during a scan, which that can make data interpretation difficult due to the dependence of the laser generated charge on the square of the pulse energy. To alleviate this, there is a function in RATACA that will only keep samples from inside one standard deviation of the mean laser pulse energy. This process gets rid of outliers, and effectively shrinks the error bars of a measurement. The process can be seen in data shown in Figure A.6. Light red data represent the laser energy of raw data collected during TPA testing, and the overlaid purple bars are data of laser pulses after being optimized. The variance in the laser energy is reduced by about 65%, significantly reducing transient data variance. The input datafile should have already been processed using the laser folder monitor, and the photo diode channel tells the code which channel on the oscilloscope the photo-diode voltage was recorded. If the photo-diode was not recorded, optimization cannot take place. Therefore, it is crucial to record the waveforms from the photo-diode as well. Only the peak of this wave form is needed, so it is sufficient to only record the first part of the waveform, and ignore the tail. The laser data is optimized by averaging the pulse energy per location for an entire measurement. The standard deviation of the pulse energy at each location is also calculated. Once this has been done, any transient produced by a laser pulse whose energy was outside 1 standard deviation of the average value is eliminated from further processing. This greatly reduces the effects of pulse-to-pulse energy variation on the interpretation of the data. Because this occurs on a location-by-location basis, it is a good idea to record several fast frames (10 or more if possible) at each location to get a better idea of the average pulse energy per location.

Example: Optimizing laser data

Note that this function modifies the original processed data file. No new file will be created.

$optimize\_laser\_data('PathToFile', 4)$

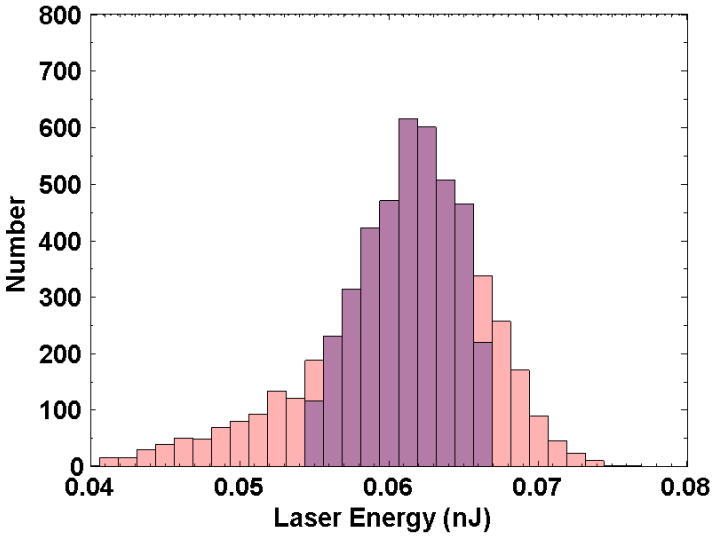

Figure A.6: Light red data represent the laser energy of raw data collected during TPA testing. Purple bars are overlaid data of laser pulses after being optimized.

A.4.2.6 Processed Laser Data

Variable Name	Type	Comments
avg_opt_energy	double	Average laser pulse energy (pJ)
charge	cell array	Total integrated charge (pC)
coords	cell array	Location of each transient capture
filtered_fwhm	cell array	FWHM of filtered transients
fwhm	cell array	FWHM of original transient
matrix_size	array	Number of record locations in [X,Y,Z]
peaks	cell array	Peak current (mA)
opt_*	cell array	Denotes data that has been optimized
num_fast_frames	int	Number of captured Fast Frames in the data file
record_length	int	Number of data points per transient
std_opt_energy	double	Standard deviation of laser energy
opt_transient_indexs	matrix	Indexes of transient inside 1 standard deviation
time	cell array	The recorded time each transient in *transients*
transients	cell array	The recorded current (mA)
xlength	int	Distance scanned in X
ylength	int	Distance scanned in Y
zlength	int	Distance scanned in Z
xstep	int	Distance per step in X
ystep	int	Distance per step in Y
zstep	int	Distance per step in Z

Table A.5: Processed laser data structure.

A.4.2.7 Processed Ion Data

Variable Name	Type	Comments
avg_opt_energy	double	Average laser pulse energy (pJ)
charge	cell array	Total integrated charge (pC)
filtered_fwhm	cell array	FWHM of filtered transients
fwhm	cell array	FWHM of original transient
peaks	cell array	Peak current (mA)
num_fast_frames	int	Number of captured Fast Frames in the data file
record_length	int	Number of data points per transient
time	cell array	The recorded time each transient in *transients*
transients	cell array	The recorded current (mA)

Table A.6: Processed ion data structure.

A.5 Data Plotting

A.5.1 General Plotting

To load processed data into the MATLAB workspace, use:

$run\_data = importdata('full\backslash path\backslash to\backslash Run1\_data\_processed.mat')$.

This will load the variables from Table A.4.2.6 into the *run_data* variable. You should spend some time reviewing structures and different data types in MATLAB. Several examples are given here for reference, but basic MATLAB information is not covered. Each cell array in the structure contains 4 cells corresponding to the 4 channels on the scope. If channels were not recorded, some cells may be empty. All variables correspond to each other.

EXAMPLE: Corresponding data

This is the way to access data for channel 3, transient 121.

X data (which is time) = run_data.time{3}(:,121)

Y data (which is current) = run_data.transients{3}(:,121)

Peak = run_data.peaks{3}(121)

Collected Charge = run_data.charge{3}(121)

FWHM = run_data.fwhm{3}(121)

It is often that a single piece of information wants to be accessed for all of the collected data. The next example if accessing all of their peak values.

EXAMPLE: Access peak current for all transient captures.

This gives access to each channels peak current values in sequential order.

$PeakCH1 = run\_data.peaks\{1\}(:);$

$PeakCH2 = run\_data.peaks\{2\}(:);$

$PeakCH3 = run\_data.peaks\{3\}(:);$

$PeakCH4 = run\_data.peaks\{4\}(:);$

You can load different runs into different variables and plot them as a function of your different run types. Next is a scatter plot example.

EXAMPLE: Scatter plot of different run.

This code snippet will load 2 separate data files, and then plot the collected charge vs. peak current on channel 2 using the same plot.

$run\_data1 = importdata(full\backslash path\backslash to\backslash Run1\_data\_processed.mat);$

$run\_data2 = importdata(full\backslash path\backslash to\backslash Run2\_data\_processed.mat);$

$scatter(run1\_data.charge\{2\}(:), run1\_data.peaks\{2\}(:), 'filled', 'ro');$

hold on % hold plot drawing to show both on the same plot

$$scatter(run2\_data.charge\{2\}(:), run2\_data.peaks\{2\}(:), 'filled', 'ks');$$

A.5.2 Pick and Plot

$function\ pick\_and\_plot\_4trans(xdata, ydata, time, transients1, transients2, ...$
$transients3, transients4, varargin)$

Pick and plot produces two figures, although only one is immediately visible. The Figure that shows up first will be a scatter plotting of the first two inputs to the function (xdata,ydata). If you mouse over this Figure you will see cross hairs. Using those cross hairs you can click on any data point in the figure. Once you do, a second Figure will open. This Figure will show four transients related to the data point. This is a good way, for example, to look at what the transients look like for your events that have the greatest peak current, collected charge, or FWHM. In addition to opening the second figure, the proper index to the data point you click on will appear in the MATLAB command window. So, if you clicked on a point in the first Figure that corresponds to the transient with index 187, you will see the number 187 in the command window. This is helpful if you want to plot a few transients together. BE CAREFUL! This is a very tough script on MATLAB and will often cause it to crash on windows. Two precautions to keep in mind are to 1) if using multiple monitors, bring the windows back to the original monitor before closing, and 2) close the pop-up window of the transients being plotted before closing the scatter plot of the X-Y data.

EXAMPLE: Pick and plot with 4 channel data.

$pick\_and\_plot\_4trans(data.peaks2, data.peaks3, data.times3, data.filtered_transients1, ...$
$data.filtered_transients2, data.filtered_transients3, data.filtered_transients4);$

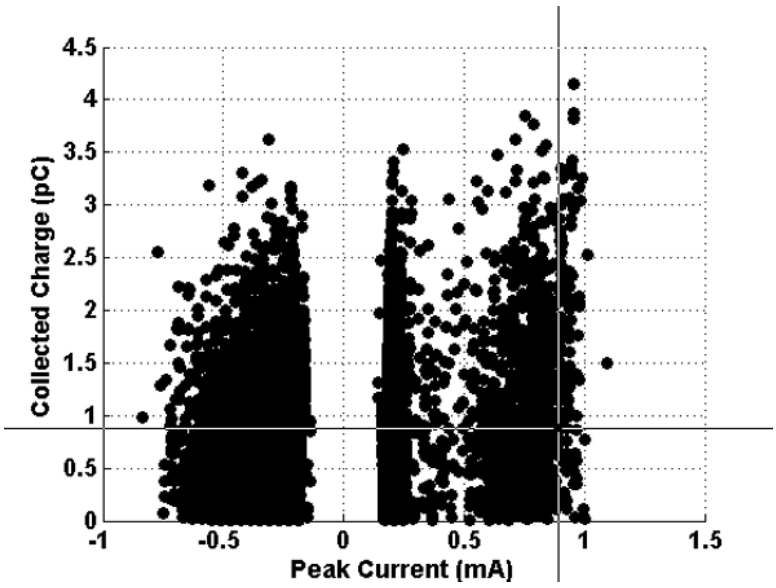

(a) XY data plot to select data to plot the resultant transients (cross-hair designates selected data).

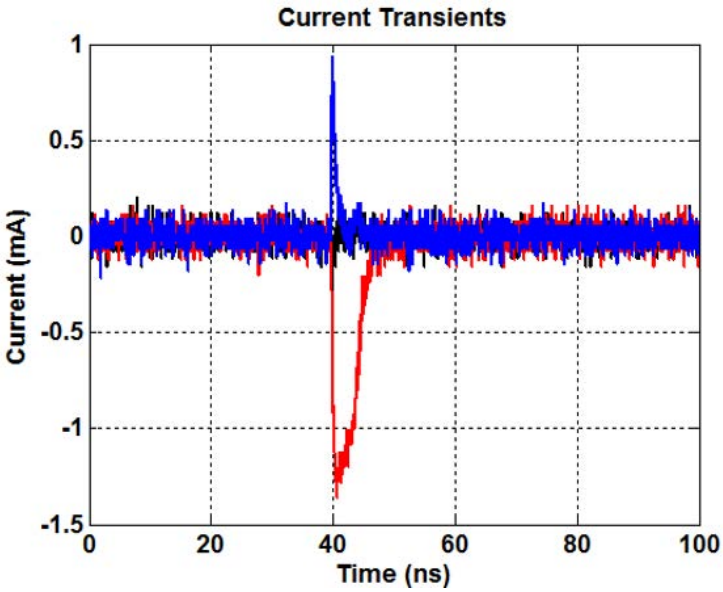

(b) Current pulse represented by the selected data from (a).

Figure A.7: Example use of *pick_and_plot* with the XY data shown in (a), and the selected transient data shown in (b).

A.5.3 Laser Specific Plotting

A.5.3.1 Plot Laser Line Scans

$function\ plot\_laser\_line\_scans(data\_file)$

$data\_file$ should be a file that only has data in 1 dimension (X or Y). It will produce a plot of peak current and collected charge as a function of the laser position for each channel in the file.

A.5.3.2 Plot Laser Area Scans

This is a 2 part process that starts with loading the data, then plots the loaded data.

Step 1:

$function\ data\_out = make\_map\_data(data\_file, varargin)$

This will create the necessary grids etc. needed to surf (plot) 3D data in MATLAB.

Step 2:

$function\ plot\_laser\_area\_scan(map\_data\_in, channel, varargin)$

Pass your map data to *map_data_in*, the number of the channel you want to plot data for into *channel*, and an optional varagin argument for the quantity you want to plot. There are 3 varagin options: 'charge', 'fwhm', or 'peak'.

EXAMPLE: Area Scan Color Map.

$plot\_laser\_area\_scan(map\_data, 3, 'quantity', 'fwhm')$.

This will plot the FWHM value for channel 3 from the imported data. Example output is shown in Figure A.8.

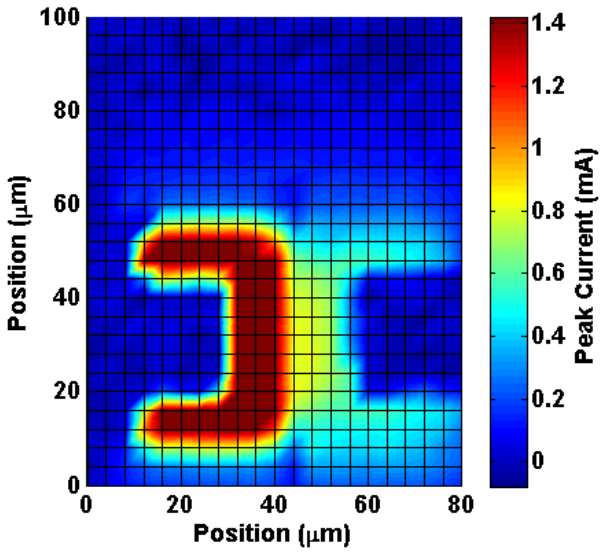

Figure A.8: Laser peak current map generated using RATACA.

Appendix B

RRAM Compact Model Code

The following two files are the code needed to implement the presented RRAM compact model using Synopsys TCAD's compact model interface. The compact circuit file is used to instantiate an instance of the model as a circuit element in the simulation netlist. The compact model file is used by the compact circuit file to calculate values during the time steps of the TCAD simulation. Users should be able to edit parameters in the compact circuit files, without having to edit the compact model file. There are hard coded debug output lines in the compact model files (lines 268 and 283), that will need to be replaced if debug output is needed. However, the model should run without this value being changed.

B.1 Compact Circuit File

```
1  DEVICE rram
2          ELECTRODES
3                  u1 // input voltage 1
4                  u2 // input voltage 2
5          INTERNALS
6                  i // current through resistor
7          PARAMETERS
8                  double r = 150000 // resistance
9                  double alpha = 0.3 //
10                 double A = 1 //
11                 double Ea = 0.4 //
12                 double q = 1.6E-19 //
13                 double k = 8.62E-5 //
14                 double RthRo = 2500 //
15                 double phi_a = -0.352 //
16                 double phi_b = 4E-8 //
17                 double tref = 300 // temperature
18                 int node = 0 //
19 END DEVICE
20
21 PSET rram_pset
22         DEVICE rram
23 END PSET
```

B.2 Compact Model File

```
#include <stdlib.h>
#include <string.h>
#include <stdio.h>
#include <iostream>
#include <fstream>
#include <math.h>
#include "CMIModels.h"
#include "CMISupport.h"
using namespace std;


class Parameters {
public:
        double r ;
        double alpha;
        double A;
        double Ea;
        double q;
        double k;
        double RthRo;
        double phi_a;
        double phi_b;
        double tref;
        double prev_time;
        double prev_dt;
        double delta_R;
        int node;

        Parameters ();
        void Set (const CCMBaseParam* param);
        void Get (CCMBaseParam* param);
};

Parameters::
Parameters () :
        r (150000),
        alpha (0.3),
        A (1),
        Ea (0.5),
        q (1.6E-19),
        k (8.62E-5),
        RthRo (2500),
        phi_a (-0.352),
```

```
44          phi_b (4E-8),
45          tref (300),
46          prev_time (0),
47          prev_dt (0),
48          delta_R (0),
49          node (0)
50  {
51  }
52
53  void Parameters::
54  Set (const CCMBaseParam* param)
55  {
56
57  if (param->Defined ()) {
58          if (strcmp (param->Name (), "r") == 0) {
59                  r = *param;
60          } else if (strcmp (param->Name (), "alpha") == 0) {
61                  alpha = *param;
62          } else if (strcmp (param->Name (), "A") == 0) {
63                  A = *param;
64          } else if (strcmp (param->Name (), "Ea") == 0) {
65                  Ea = *param;
66          } else if (strcmp (param->Name (), "q") == 0) {
67                  q = *param;
68          } else if (strcmp (param->Name (), "k") == 0) {
69                  k = *param;
70          } else if (strcmp (param->Name (), "RthRo") == 0) {
71                  RthRo = *param;
72          } else if (strcmp (param->Name (), "phi_a") == 0) {
73                  phi_a = *param;
74          } else if (strcmp (param->Name (), "phi_b") == 0) {
75                  phi_b = *param;
76          } else if (strcmp (param->Name (), "tref") == 0) {
77                  tref = *param;
78          } else if (strcmp (param->Name (), "prev_time") ==
                0) {
79                  prev_time = *param;
80          } else if (strcmp (param->Name (), "prev_dt") == 0)
                {
81                  prev_dt = *param;
82          } else if (strcmp (param->Name (), "delta_R") == 0)
                {
83                  delta_R = *param;
84          } else if (strcmp (param->Name (), "node") == 0) {
85                  node = *param;
```

```
86                  }
87          }
88  }
89
90  void Parameters::
91  Get (CCMBaseParam* param)
92  {
93
94  if (strcmp (param->Name (), "r") == 0) {
95                  *param = r;
96                  param->Defined (1);
97          } else if (strcmp (param->Name (), "alpha") == 0) {
98                  *param = alpha;
99                  param->Defined (1);
100         } else if (strcmp (param->Name (), "A") == 0) {
101                 *param = A;
102                 param->Defined (1);
103         } else if (strcmp (param->Name (), "Ea") == 0) {
104                 *param = Ea;
105                 param->Defined (1);
106         } else if (strcmp (param->Name (), "q") == 0) {
107                 *param = q;
108                 param->Defined (1);
109         } else if (strcmp (param->Name (), "k") == 0) {
110                 *param = k;
111                 param->Defined (1);
112         } else if (strcmp (param->Name (), "RthRo") == 0) {
113                 *param = RthRo;
114                 param->Defined (1);
115         } else if (strcmp (param->Name (), "alpha") == 0) {
116                 *param = alpha;
117                 param->Defined (1);
118         } else if (strcmp (param->Name (), "phi_a") == 0) {
119                 *param = phi_a;
120                 param->Defined (1);
121         } else if (strcmp (param->Name (), "phi_b") == 0) {
122                 *param = phi_b;
123                 param->Defined (1);
124         } else if (strcmp (param->Name (), "prev_time") ==
              0) {
125                 *param = prev_time;
126                 param->Defined (1);
127         } else if (strcmp (param->Name (), "tref") == 0) {
128                 *param = tref;
129                 param->Defined (1);
```

```
130         } else if (strcmp (param->Name (), "prev_dt") == 0)
                {
131                 *param = prev_dt;
132                 param->Defined (1);
133         } else if (strcmp (param->Name (), "delta_R") == 0)
                {
134                 *param = delta_R;
135                 param->Defined (1);
136         } else if (strcmp (param->Name (), "node") == 0) {
137                 *param = node;
138                 param->Defined (1);
139         } else {
140                 param->Defined (0);
141         }
142 }
143
144 class Device {
145 public:
146         Parameters par;
147 };
148
149 class PSet {
150 public:
151         Parameters par;
152 };
153
154 class Instance {
155 public:
156         Parameters par;
157 };
158
159 extern "C" void
160 cmi_device_create (CCMBaseDevice*const device)
161 { device->device_desc = new Device;
162 }
163 extern "C" void
164 cmi_device_set_param (CCMBaseDevice*const device,
165                       const CCMBaseParam*const param)
166 { Device* dev = (Device*) device->device_desc;
167 dev->par.Set (param);
168 }
169
170 extern "C" void
171 cmi_device_initialize (CCMBaseDevice*const device)
172 {
```

```
173 }
174
175 extern "C" void
176 cmi_device_get_param (CCMBaseDevice*const device,
177                       CCMBaseParam*const param)
178 { Device* dev = (Device*) device->device_desc;
179 dev->par.Get (param);
180 }
181
182 extern "C" void
183 cmi_device_delete (CCMBaseDevice*const device)
184 { delete (Device*) device->device_desc;
185 }
186
187 extern "C" void
188 cmi_pset_create (CCMBasePSet*const pset)
189 { pset->pset_desc = new PSet;
190 }
191
192 extern "C" void
193 cmi_pset_set_param (CCMBasePSet*const pset,
194                     const CCMBaseParam*const param)
195 { PSet* ps = (PSet*) pset->pset_desc;
196 ps->par.Set (param);
197 }
198
199 extern "C" void
200 cmi_pset_initialize (CCMBasePSet*const pset)
201 {
202 }
203
204 extern "C" void
205 cmi_pset_get_param (CCMBasePSet*const pset,
206                     CCMBaseParam*const param)
207 { PSet* ps = (PSet*) pset->pset_desc;
208 ps->par.Get (param);
209 }
210
211 extern "C" void
212 cmi_pset_delete (CCMBasePSet*const pset)
213 { delete (PSet*) pset->pset_desc;
214 }
215
216 extern "C" void
217 cmi_instance_create (CCMBaseInstance*const instance)
```

```
218 { instance->instance_desc = new Instance;
219
220 }
221
222 extern "C" void
223 cmi_instance_set_param (CCMBaseInstance*const instance,
224                         const CCMBaseParam*const param)
225 { Instance* inst = (Instance*) instance->instance_desc;
226 inst->par.Set (param);
227 }
228
229 extern "C" void
230 cmi_instance_initialize (CCMBaseInstance*const instance)
231 { Instance* inst = (Instance*) instance->instance_desc;
232 }
233
234 extern "C" void
235 cmi_instance_get_param (CCMBaseInstance*const instance,
236                         CCMBaseParam*const param)
237 { Instance* inst = (Instance*) instance->instance_desc;
238 inst->par.Get (param);
239 }
240
241
242
243 #define u1 (variables [0])
244 #define u2 (variables [1])
245 #define i (variables [2])
246
247
248
249 extern "C" void
250 cmi_instance_get_rhs (CCMBaseInstance*const instance,
251                       const int dc, const double time,
252                       const double*const variables,
253                       double*const rhs)
254 { Instance* inst = (Instance*) instance->instance_desc;
255         if (dc) {
256                 double local_time = time;
257                 double dt = local_time - inst->par.prev_time
                        ;
258                 double R = inst->par.r;
259                 std::string node_string;
260                 std::fstream fs;
261
```

```
262                 //write header to the output file
263                 if (time == 0){
264
265                         ostringstream convert;
266                         convert << inst->par.node;
267                         node_string = convert.str();
268                         std::string fname("/home/bennetw1/
                               TCAD/RRAM/FinFET/rram_output/
                               rram_output_node"+node_string+".
                               txt");
269                         char *fileName = (char*)fname.c_str
                               ();
270                         fs.open (fileName, std::fstream::in
                               | std::fstream::out | std::
                               fstream::trunc);
271                         fs << "Time(s)\tElectrode1(V)\
                               tElectrode2(V)\tRRAM(Ohm)\
                               tCurrent(A)\tDelta_R(Ohm)" <<
                               endl;
272                         fs.close();
273                         }
274
275                 //write out data if last time step was
                       successful
276                 if (dt > 0){
277                         R = inst->par.r - inst->par.delta_R;
278                         inst->par.r = R;
279
280                         ostringstream convert;
281                         convert << inst->par.node;
282                         node_string = convert.str();
283                         std::string fname("/home/bennetw1/
                               TCAD/RRAM/FinFET/rram_output/
                               rram_output_node"+node_string+".
                               txt");
284                         char *fileName = (char*)fname.c_str
                               ();
285                         fs.open (fileName, std::fstream::in
                               | std::fstream::out | std::
                               fstream::app);
286                         fs << time << "\t" << u1 << "\t" <<
                               u2 << "\t" << R << "\t" << i << "
                               \t" << inst->par.delta_R << endl
                               ;
287                         fs.close();
```

```
288                         }
289                     if (dt == 0){dt=inst->par.prev_dt;}
290                     else if(dt < 0){dt = inst->par.prev_dt + dt
                            ;}
291                     inst->par.prev_dt=dt;
292                     inst->par.prev_time = time;
293
294
295
296                     double V = u1 - u2;
297                     double phi = (inst->par.phi_b)*pow(inst->par
                            .r,(inst->par.phi_a));
298                     if (V > 0.1){
299                     inst->par.delta_R = 2*inst->par.r*dt/(phi*
                            exp((inst->par.Ea - (inst->par.q*inst->
                            par.alpha*V))/(inst->par.k*(inst->par.
                            tref + V*V*inst->par.RthRo))));
300                     } else {
301                     inst->par.delta_R = 0;
302                     }
303                     //inst->par.delta_R = 2*150000*dt/(phi*exp((
                            inst->par.Ea - (inst->par.q*inst->par.
                            alpha*V))/(inst->par.k*(inst->par.tref +
                            V*V*inst->par.RthRo))));
304
305                     cout << "dt:" << dt << "\tu1:" << u1 << "\
                            tu2:" << u2 << "\tR:" << R << "\tdR:" <<
                            inst->par.delta_R << endl;
306
307                     rhs [0] = i;
308                     rhs [1] = -i;
309                     rhs [2] = u1 - u2 - R * i;
310                     //rhs [2] = u1 - u2 - 1 * i;
311                     } else {
312                     rhs [0] = 0.0;
313                     rhs [1] = 0.0;
314                     rhs [2] = 0.0;
315             }
316 }
317
318 extern "C" void
319 cmi_instance_get_jacobian (CCMBaseInstance*const instance,
320                                     const int dc, const double
                                        time,
```

```
321                                     const double*const variables
                                            ,
322                                     double*const*const jacobian)
323 { Instance* inst = (Instance*) instance->instance_desc;
324 if (dc) {
325         double dt = time - inst->par.prev_time;
326         double R = inst->par.r;
327         //inst->par.prev_time = time;
328
329         //std::fstream fs;
330         //fs.open ("/home/bennetw1/TCAD/rram_cmi/debug.txt",
                std::fstream::in | std::fstream::out | std::
              fstream::app);
331         //fs << "u1:" << u1 << " u2:" << u2 << << " R:" << R
                << " i:" i << endl;
332         //fs.close();
333
334         jacobian[0][2] = 1.0;
335         jacobian[1][2] = -1.0;
336         jacobian[2][0] = 1.0;
337         jacobian[2][1] = -1.0;
338         jacobian[2][2] = -R;
339         //jacobian[2][2] = -1;
340         }
341 }
342
343 extern "C" int
344 cmi_instance_is_physical (CCMBaseInstance*const instance,
345                                     const double time,
346                                     const double*const variables
                                            )
347 { return 1;
348 }
349
350 extern "C" void
351 cmi_instance_delete (CCMBaseInstance*const instance)
352 { delete (Instance*) instance->instance_desc;
353 }
```

REFERENCES

[1] G. J. Brucker, R. Smeltzer, W. A. Kolasinski, and R. Koga, "Soft error dependence on feature size," *IEEE Trans. Nucl. Sci.*, vol. 31, no. 6, pp. 1562–1564, 1984.

[2] M. L. Alles, R. D. Schrimpf, R. A. Reed, L. W. Massengill, R. A. Weller, M. H. Mendenhall, D. R. Ball, K. M. Warren, T. D. Loveless, J. S. Kauppila, and B. D. Sierawski, "Radiation hardness of FDSOI and FinFET technologies," in *IEEE International SOI Conference (SOI)*, 2011, pp. 1–2.

[3] J. C. Pickel and J. T. Blandford, "Cosmic-ray-induced errors in MOS devices," *IEEE Trans. Nucl. Sci.*, vol. 27, no. 2, pp. 1006–1015, 1980.

[4] L. W. Massengill, O. A. Amusan, S. DasGupta, A. L. Sternberg, J. D. Black, A. F. Witulski, B. L. Bhuva, and M. L. Alles, "Soft-Error Charge-Sharing Mechanisms at Sub-100 nm Technology Nodes," in *IEEE International Conference on Integrated Circuit Design and Technology*, 2007, pp. 1–4.

[5] K. Kuhn, M. Liu, and H. Kennel, "Technology options for 22nm and beyond," in *2010 International Workshop on Junction Technology (IWJT)*, 2010, pp. 1–6.

[6] H. Y. Lee, P. S. Chen, T. Y. Wu, Y. S. Chen, C. C. Wang, P. J. Tzeng, C. H. Lin, F. Chen, C. H. Lien, and M.-J. Tsai, "Low power and high speed bipolar switching with a thin reactive ti buffer layer in robust HfO2 based RRAM," in *Electron Devices Meeting, 2008. IEDM 2008. IEEE International*, 2008, pp. 1–4.

[7] O. A. Amusan, A. F. Witulski, L. W. Massengill, B. L. Bhuva, P. R. Fleming, M. L. Alles, A. L. Sternberg, J. D. Black, and R. D. Schrimpf, "Charge Collection and Charge Sharing in a 130 nm CMOS Technology," *IEEE Trans. Nucl. Sci.*, vol. 53, no. 6, pp. 3253–3258, 2006.

[8] B. D. Olson, D. R. Ball, K. M. Warren, L. W. Massengill, N. F. Haddad, S. E. Doyle, and D. McMorrow, "Simultaneous Single Event Charge Sharing and Parasitic Bipolar Conduction in a Highly-scaled SRAM Design," *IEEE Trans. Nucl. Sci.*, vol. 52, no. 6, pp. 2132–2136, 2005.

[9] J. R. Ahlbin, L. W. Massengill, B. L. Bhuva, B. Narasimham, M. J. Gadlage, and P. H. Eaton, "Single-Event Transient Pulse Quenching in Advanced CMOS Logic Circuits," *IEEE Trans. Nucl. Sci.*, vol. 56, no. 6, pp. 3050–3056, 2009.

[10] S. Rezgui, R. Won, and J. Tien, "SET Characterization and Mitigation in 65-nm CMOS Test Structures," *IEEE Trans. Nucl. Sci.*, vol. 59, no. 4, pp. 851–859, 2012.

[11] L. Artola, G. Hubert, K. M. Warren, M. Gaillardin, R. D. Schrimpf, R. A. Reed, R. A. Weller, J. R. Ahlbin, P. Paillet, M. Raine, S. Girard, S. Duzellier, L. W. Massengill, and F. Bezerra, "SEU Prediction From SET Modeling Using Multi-Node Collection in Bulk Transistors and SRAMs Down to the 65 nm Technology Node," *IEEE Trans. Nucl. Sci.*, vol. 58, no. 3, pp. 1338–1346, 2011.

[12] J. S. Kauppila, T. D. Haeffner, D. R. Ball, A. V. Kauppila, T. D. Loveless, S. Jagannathan, A. L. Sternberg, B. L. Bhuva, and L. W. Massengill, "Circuit-Level Layout-Aware Single-Event Sensitive-Area Analysis of 40-nm Bulk CMOS Flip-Flops Using Compact Modeling," *IEEE Trans. Nucl. Sci.*, vol. 58, no. 6, pp. 2680–2686, 2011.

[13] L. Entrena, A. Lindoso, E. S. Millan, S. Pagliarini, F. Almeida, and F. Kastensmidt, "Constrained Placement Methodology for Reducing SER Under Single-Event-Induced Charge Sharing Effects," *IEEE Trans. Nucl. Sci.*, vol. 59, no. 4, pp. 811–817, 2012.

[14] R. W. Blaine, S. E. Armstrong, J. S. Kauppila, N. M. Atkinson, B. D. Olson, W. T. Holman, and L. W. Massengill, "RHBD Bias Circuits Utilizing Sensitive Node Active Charge Cancellation," *IEEE Trans. Nucl. Sci.*, vol. 58, no. 6, pp. 3060–3066, 2011.

[15] B. Narasimham, J. K. Wang, M. Buer, R. Gorti, K. Chandrasekharan, K. M. Warren, B. D. Sierawski, R. D. Schrimpf, R. A. Reed, and R. A. Weller, "Contribution of Control Logic Upsets and Multi-Node Charge Collection to Flip-Flop SEU Cross-Section in 40-nm CMOS," *IEEE Trans. Nucl. Sci.*, vol. 57, no. 6, pp. 3176–3182, 2010.

[16] G. Toure, G. Hubert, K. Castellani-Coulie, S. Duzellier, and J. Portal, "Simulation of Single and Multi-Node Collection: Impact on SEU Occurrence in Nanometric SRAM Cells," *IEEE Trans. Nucl. Sci.*, vol. 58, no. 3, pp. 862–869, 2011.

[17] W. G. Bennett, R. D. Schrimpf, N. C. Hooten, R. A. Reed, J. S. Kauppila, R. A. Weller, K. M. Warren, and M. H. Mendenhall, "Efficient Method for Estimating the Characteristics of Radiation-Induced Current Transients," *IEEE Trans. Nucl. Sci.*, vol. 59, no. 6, pp. 2704–2709, 2012.

[18] S. Natarajan, M. Armstrong, M. Bost, R. Brain, M. Brazier, C.-H. Chang, V. Chikarmane, M. Childs, H. Deshpande, K. Dev, G. Ding, T. Ghani, O. Golonzka, W. Han, J. He, R. Heussner, R. James, I. Jin, C. Kenyon, S. Klopcic, S.-H. Lee, M. Liu, S. Lodha, B. McFadden, A. Murthy, L. Neiberg, J. Neirynck, P. Packan, S. Pae, C. Parker, C. Pelto, L. Pipes, J. Sebastian, J. Seiple, B. Sell, S. Sivakumar, B. Song, K. Tone, T. Troeger, C. Weber, M. Yang, A. Yeoh, and K. Zhang, "A 32 nm Logic Technology Featuring 2nd-Generation High-k+ Metal-gate Transistors, Enhanced Channel Strain and 0.171 μm^2 SRAM Cell Size in a 291 Mb Array," in *IEEE International Electron Devices Meeting*, 2008, pp. 1–3.

[19] R. Doering, *Handbook of Semiconductor Manufacturing Technology, Second Edition*. CRC Press, 2007.

[20] R. Reed, "Fundamental mechanisms for single particle-induced soft errors," *Nuclear and Space Radiation Effects Conference Short Course Notebook*, 2008.

[21] L. Edmonds, "Electric currents through ion tracks in silicon devices," *IEEE Trans. Nucl. Sci.*, vol. 45, no. 6, pp. 3153 –3164, Dec. 1998.

[22] ——, "A theoretical analysis of steady-state charge collection in simple diodes under high-injection conditions," *IEEE Trans. Nucl. Sci.*, vol. 57, no. 2, pp. 818 –830, Apr. 2010.

[23] C. I. Underwood, D. J. Brock, P. S. Wiliams, S. Kim, R. Dilao, P. R. Santos, M. C. Brito, C. S. Dyer, and A. J. Sims, "Radiation environment measurements with the cosmic ray experiments on-board the KITSAT-1 and PoSAT-1 micro-satellites," *IEEE Trans. Nucl. Sci.*, vol. 41, no. 6, pp. 2353–2360, 1994.

[24] A. J. Tylka, J. H. Adams, P. R. Boberg, B. Brownstein, W. F. Dietrich, E. O. Flueckiger, E. L. Petersen, M. A. Shea, D. F. Smart, and E. C. Smith, "CREME96: a revision of the cosmic ray effects on micro-electronics code," *IEEE Trans. Nucl. Sci.*, vol. 44, no. 6, pp. 2150–2160, 1997.

[25] J. L. Barth, C. S. Dyer, and E. G. Stassinopoulos, "Space, atmospheric, and terrestrial radiation environments," *IEEE Trans. Nucl. Sci.*, vol. 50, no. 3, pp. 466–482, 2003.

[26] F. W. Sexton, "Microbeam studies of single-event effects," *IEEE Trans. Nucl. Sci.*, vol. 43, no. 2, pp. 687–695, 1996.

[27] J. S. Melinger, S. Buchner, D. McMorrow, W. J. Stapor, T. R. Weatherford, A. B. Campbell, and H. Eisen, "Critical evaluation of the pulsed laser method for single event effects testing and fundamental studies," *IEEE Trans. Nucl. Sci.*, vol. 41, no. 6, pp. 2574–2584, 1994.

[28] D. McMorrow, W. T. Lotshaw, J. S. Melinger, S. Buchner, and R. L. Pease, "Subbandgap Laser-induced Single Event Effects: Carrier Generation Via Two-photon Absorption," *IEEE Trans. Nucl. Sci.*, vol. 49, no. 6, pp. 3002–3008, 2002.

[29] D. M. Cardoza, S. D. LaLumondiere, M. A. Tockstein, S. C. Witczak, Y. Sin, B. J. Foran, W. T. Lotshaw, and S. C. Moss, "Single event transients induced by picosecond pulsed x-ray absorption in III #x2013;v heterojunction transistors," *IEEE Trans. Nucl. Sci.*, vol. 59, no. 6, pp. 2729–2738, 2012.

[30] D. M. Fleetwood, S. L. Kosier, R. N. Nowlin, R. D. Schrimpf, J. Reber, R. A., M. DeLaus, P. S. Winokur, A. Wei, W. E. Combs, and R. L. Pease, "Physical mechanisms contributing to enhanced bipolar gain degradation at low dose rates," *IEEE Trans. Nucl. Sci.*, vol. 41, no. 6, pp. 1871–1883, 1994.

[31] N. M. Atkinson, A. F. Witulski, W. T. Holman, J. R. Ahlbin, B. L. Bhuva, and L. W. Massengill, "Layout technique for single-event transient mitigation via pulse quenching," *IEEE Trans. Nucl. Sci.*, vol. 58, no. 3, pp. 885–890, 2011.

[32] R. W. Blaine, N. M. Atkinson, J. S. Kauppila, S. E. Armstrong, N. C. Hooten, J. H. Warner, W. T. Holman, and L. W. Massengill, "Differential charge cancellation (DCC) layout as an RHBD technique for bulk CMOS differential circuit design," *IEEE Trans. Nucl. Sci.*, vol. 59, no. 6, pp. 2867–2871, 2012.

[33] N. Seifert, V. Ambrose, B. Gill, Q. Shi, R. Allmon, C. Recchia, S. Mukherjee, N. Nassif, J. Krause, J. Pickholtz, and A. Balasubramanian, "On the radiation-induced soft error performance of hardened sequential elements in advanced bulk CMOS technologies," in *Reliability Physics Symposium (IRPS), 2010 IEEE International*, 2010, pp. 188–197.

[34] R. W. Blaine, N. M. Atkinson, J. S. Kauppila, T. D. Loveless, S. E. Armstrong, W. T. Holman, and L. W. Massengill, "Single-event-hardened CMOS operational amplifier design," *IEEE Trans. Nucl. Sci.*, vol. 59, no. 4, pp. 803–810, 2012.

[35] H.-S. P. Wong, H.-Y. Lee, S. Yu, Y.-S. Chen, Y. Wu, P.-S. Chen, B. Lee, F. T. Chen, and M.-J. Tsai, "Metal #x2013;oxide RRAM," *Proceedings of the IEEE*, vol. 100, no. 6, pp. 1951–1970, 2012.

[36] S. Tanachutiwat, M. Liu, and W. Wang, "FPGA based on integration of CMOS and RRAM," *IEEE Transactions on Very Large Scale Integration (VLSI) Systems*, vol. 19, no. 11, pp. 2023–2032, 2011.

[37] Y.-S. Chen, H.-Y. Lee, P.-S. Chen, W.-H. Liu, S.-M. Wang, P.-Y. Gu, Y.-Y. Hsu, C.-H. Tsai, W.-S. Chen, F. Chen, M.-J. Tsai, and C. Lien, "Robust high-resistance state and improved endurance of resistive memory by suppression of current overshoot," *IEEE Electron Device Letters*, vol. 32, no. 11, pp. 1585–1587, 2011.

[38] A. Mehonic, A. Vrajitoarea, S. Cueff, S. Hudziak, H. Howe, C. Labb, R. Rizk, M. Pepper, and A. J. Kenyon, "Quantum conductance in silicon oxide resistive memory devices," *Scientific Reports*, vol. 3, Sep. 2013. [Online]. Available: http://www.nature.com/srep/2013/130919/srep02708/full/srep02708.html

[39] Y. Y. Chen, R. Degraeve, S. Clima, B. Govoreanu, L. Goux, A. Fantini, G. S. Kar, G. Pourtois, G. Groeseneken, D. J. Wouters, and M. Jurczak, "Understanding of the endurance failure in scaled HfO2-based 1T1R RRAM through vacancy mobility degradation," in *Electron Devices Meeting (IEDM), 2012 IEEE International*, 2012, pp. 20. 3.1–20.3.4.

[40] R. Waser, S. Menzel, and V. Rana, "Recent progress in redox-based resistive switching," in *2012 IEEE International Symposium on Circuits and Systems (ISCAS)*, 2012, pp. 1596–1599.

[41] Y. Shiyanovskii, A. Rajendran, F. Wolff, and C. Papachristou, "Effect of voltage scaling on soft error protection methods for SRAMs," in *Aerospace and Electronics Conference (NAECON), Proceedings of the IEEE 2010 National*, 2010, pp. 328–333.

[42] L. Chang, D. M. Fried, J. Hergenrother, J. W. Sleight, R. H. Dennard, R. K. Montoye, L. Sekaric, S. J. McNab, A. W. Topol, C. D. Adams, K. W. Guarini, and W. Haensch, "Stable SRAM cell design for the 32 nm node and beyond," in *2005 Symposium on VLSI Technology, 2005. Digest of Technical Papers*, 2005, pp. 128–129.

[43] M. Fliesler, D. Still, and J.-M. Hwang, "A 15 ns 4 Mb NVSRAM in 0.13 u SONOS technology," in *Non-Volatile Semiconductor Memory Workshop, 2008 and 2008 International Conference on Memory Technology and Design. NVSMW/ICMTD 2008. Joint*, 2008, pp. 83–86.

[44] "Cypress CY14B102 2Mbit and CY14B108 8Mbit nvSRams." [Online]. Available: http://www.electronicsweekly.com/news/products/memory-products/cypress-cy14b102-2mbit-and-cy14b108-8mbit-nvsrams-2008-07/

[45] T. Calin, M. Nicolaidis, and R. Velazco, "Upset hardened memory design for submicron CMOS technology," *IEEE Trans. Nucl. Sci.*, vol. 43, no. 6, pp. 2874–2878, 1996.

[46] D. Rose, "Memory test tips #3: Improving flash memory testing with pulse generators EE times." [Online]. Available: http://www.eetimes.com/document.asp?doc_id=1280214

[47] S. Tehrani, J. M. Slaughter, E. Chen, M. Durlam, J. Shi, and M. DeHerren, "Progress and outlook for MRAM technology," *IEEE Transactions on Magnetics*, vol. 35, no. 5, pp. 2814–2819, 1999.

[48] J. Heidecker, "MRAM technology status," Feb. 2013. [Online]. Available: http://trs-new.jpl.nasa.gov/dspace/bitstream/2014/43135/1/JPL%20Pub%2013-3.pdf

[49] T. Devolder, "Material issues for the scalability of MRAMs |ahmed ." [Online]. Available: http://www.ahmedabdelhamid.com/main/?p=212

[50] Y. S. Chen, H. Y. Lee, P. S. Chen, P. Y. Gu, C. W. Chen, W. P. Lin, W. H. Liu, Y. Y. Hsu, S. S. Sheu, P.-C. Chiang, W.-S. Chen, F. T. Chen, C. H. Lien, and M.-J. Tsai, "Highly scalable hafnium oxide memory with improvements of resistive distribution and read disturb immunity," in *Electron Devices Meeting (IEDM), 2009 IEEE International*, 2009, pp. 1–4.

[51] D. Ielmini, S. Larentis, and S. Balatti, "Physical modeling of voltage-driven resistive switching in oxide RRAM," in *Integrated Reliability Workshop Final Report (IRW), 2012 IEEE International*, 2012, pp. 9–15.

[52] S. Koveshnikov, K. Matthews, K. Min, D. C. Gilmer, M. G. Sung, S. Deora, H. F. Li, S. Gausepohl, P. D. Kirsch, and R. Jammy, "Real-time study of switching kinetics in integrated 1T/ HfOx 1R RRAM: intrinsic tunability of set/reset voltage and trade-off with switching time," in *Electron Devices Meeting (IEDM), 2012 IEEE International*, 2012, pp. 20. 4.1–20.4.3.

[53] B. Butcher, S. Koveshnikov, D. C. Gilmer, G. Bersuker, M. G. Sung, A. Kalantarian, C. Park, R. Geer, Y. Nishi, P. D. Kirsch, and R. Jammy, "High endurance performance of 1T1R HfOx based RRAM at low (#x003c;20 #x03bc;a) operative current and elevated (150 #x00b0;c) temperature," in *Integrated Reliability Workshop Final Report (IRW), 2011 IEEE International*, 2011, pp. 146–150.

[54] Y. Y. Chen, B. Govoreanu, L. Goux, R. Degraeve, A. Fantini, G. S. Kar, D. J. Wouters, G. Groeseneken, J. A. Kittl, M. Jurczak, and L. Altimime, "Balancing SET/RESET pulse for endurance in 1T1R bipolar RRAM," *IEEE Transactions on Electron Devices*, vol. 59, no. 12, pp. 3243–3249, 2012.

[55] D. Ielmini, F. Nardi, and S. Balatti, "Evidence for voltage-driven Set/Reset processes in bipolar switching RRAM," *IEEE Transactions on Electron Devices*, vol. 59, no. 8, pp. 2049–2056, 2012.

[56] Y. Y. Chen, R. Degraeve, B. Govoreanu, S. Clima, L. Goux, A. Fantini, G. S. Kar, D. J. Wouters, G. Groeseneken, and M. Jurczak, "Postcycling LRS retention analysis in RRAM 1T1R device," *IEEE Electron Device Letters*, vol. 34, no. 5, pp. 626–628, 2013.

[57] Y. Y. Chen, L. Goux, S. Clima, B. Govoreanu, R. Degraeve, G. S. Kar, A. Fantini, G. Groeseneken, D. J. Wouters, and M. Jurczak, "Endurance/Retention trade-off on cap 1T1R bipolar RRAM," *IEEE Transactions on Electron Devices*, vol. 60, no. 3, pp. 1114–1121, 2013.

[58] K. Shao, V. Pouget, E. Faraud, C. Larue, D. McMorrow, and D. Lewis, "3D Knife-edge Characterization of Two-Photon Absorption Volume in Silicon for Integrated Circuit Testing," in *Nonlinear Optics*, ser. OSA Technical Digest (CD). Optical Society of America, Jul. 2011, p. NMD5.

[59] N. Hooten, W. Bennett, L. Edmonds, J. Kozub, R. Reed, R. Schrimpf, and R. Weller, "The Impact of Depletion Region Potential Modulation on Ion-Induced Current Transient Response," *IEEE Trans. Nucl. Sci.*, in this issue.

[60] "Synopsys TCAD," 2011. [Online]. Available: http://www.synopsys.com/tools/tcad/Pages/default.aspx

[61] N. Hooten, L. Edmonds, W. G. Bennett, J. Ahlbin, N. Dodds, R. Reed, R. Schrimpf, and R. Weller, "The Significance of High-Level Carrier Generation Conditions for Charge Collection in Irradiated Devices," *IEEE Transactions on Nuclear Science*, vol. 59, no. 6, pp. 2710–2721, 2012.

[62] R. A. Weller, M. H. Mendenhall, R. A. Reed, R. D. Schrimpf, K. M. Warren, B. D. Sierawski, and L. W. Massengill, "Monte Carlo Simulation of Single Event Effects," *IEEE Trans. Nucl. Sci.*, vol. 57, no. 4, pp. 1726–1746, 2010.

[63] E. Marinissen, B. Prince, D. Keltel-Schulz, and Y. Zorian, "Challenges in embedded memory design and test," in *Design, Automation and Test in Europe, 2005. Proceedings*, 2005, pp. 722–727 Vol. 2.

[64] R. Degraeve, A. Fantini, S. Clima, B. Govoreanu, L. Goux, Y. Y. Chen, D. Wouters, P. Roussel, G. Kar, G. Pourtois, S. Cosemans, J. Kittl, G. Groeseneken, M. Jurczak, and L. Altimime, "Dynamic hour glass model for SET and RESET in HfO2 RRAM," in *2012 Symposium on VLSI Technology (VLSIT)*, 2012, pp. 75–76.

[65] R. Degraeve, A. Fantini, N. Raghavan, Y. Chen, L. Goux, S. Clima, S. Cosemans, B. Govoreanu, D. Wouters, P. Roussel, G. Kar, G. Groeseneken, and M. Jurczak, "Modeling RRAM set/reset statistics resulting in guidelines for optimized operation," in *2013 Symposium on VLSI Technology (VLSIT)*, 2013, pp. T98–T99.

[66] D. Ielmini, "Filamentary-switching model in RRAM for time, energy and scaling projections," in *Electron Devices Meeting (IEDM), 2011 IEEE International*, 2011, pp. 17.2.1–17.2.4.

[67] J. Schwank, V. Ferlet-Cavrois, M. R. Shaneyfelt, P. Paillet, and P. Dodd, "Radiation effects in SOI technologies," *IEEE Transactions on Nuclear Science*, vol. 50, no. 3, pp. 522–538, 2003.

[68] V. Ferlet-Cavrois, L. Massengill, and P. Gouker, "Single Event Transients in Digital CMOS - Review," *IEEE Transactions on Nuclear Science*, vol. 60, no. 3, pp. 1767–1790, 2013.

[69] T. ROEHR, "Electronic device with a memory cell," Patent US 7 289 350, 10 30, 2007. [Online]. Available: http://www.patentlens.net/patentlens/patent/US_7289350/en/

[70] C.-H. Lin, R. Kambhampati, R. Miller, T. B. Hook, A. Bryant, W. Haensch, P. Oldiges, I. Lauer, T. Yamashita, V. Basker, T. Standaert, K. Rim, E. Leobandung, H. Bu, and M. Khare, "Channel doping impact on FinFETs for 22nm and beyond," in *2012 Symposium on VLSI Technology (VLSIT)*, Jun. 2012, pp. 15–16.